Mathematical model for ethane pyrolysis in an industrial furnace

by

Emily Victoria Cowperthwaite

A thesis submitted to the Graduate Program in Chemical Engineering

in conformity with the requirements for the

Degree of Master of Applied Science

Queen's University

Kingston, Ontario, Canada

September 19, 2014

Abstract

Ethane pyrolysis is an important industrial process that occurs by passing ethane and steam through radiant coils (tubes) in gas-fired furnaces to produce ethylene and other light olefins. Undesirable side reactions that occur during the pyrolysis of ethane lead to the formation of coke (solid carbon) on the tube walls, which has to be periodically burnt off in decoking cycles. NOVA Chemicals is interested in developing a model that can accurately predict dynamic coke formation and associated decoking times that would help to optimize run lengths, and decrease costs.

A steady-state ethane pyrolysis model of the radiant section of a floor-fired furnace was developed as a first step towards development of a dynamic coke formation model. The model includes 56 pyrolysis reactions involving 28 species, and accounts for radiant heat transfer from the furnace gas to the process gas using the Roesler flux method. The process-side model includes 29 material balances (28 reacting species plus inert steam), 1 energy balance and 1 momentum balance to track the concentration of the 29 species, the process gas temperature and the process gas pressure along the length of the reactor. These model equations are implemented in PREDICI® as an initial value problem.

The furnace-side model, which includes 2 radiant flux balances and 1 energy balance, resulted in numerical problems when solved as an initial value problem in PREDICI®. Instead, the model was discretized using finite differences and simplifying assumptions. The resulting system of algebraic equations was solved in PREDICI® and then radiant fluxes were imposed on the process-side model. Preliminary studies of model responses to changes in key model inputs indicate that the model performs as physically expected, rendering this model a strong starting point for future model development.

Acknowledgements

I would like to thank a number of people without whom this project would not have been possible. First of all, to my supervisor Dr. Kim McAuley, thank you for your guidance, expertise and consistent support. Dr. Bolaji Olayiwola from NOVA Chemicals, it has been a pleasure to work with you on this project. Thank you for always taking the time to help me, and for helping me to understand the greater context of this research. To all of the other members of the Petrochemicals Team and beyond at NOVA Research and Technology Centre, thank you for making my 6 months in Calgary such a positive experience.

Dr. Michael Wulkow, the developer of PREDICI®, thank you for your timely responses to all of my PREDICI® questions, and for always working hard to find a way to solve my problems. Thank you to NSERC, NOVA Chemicals, Queen's University and the Province of Ontario for financial and scholarship support.

Thank you to my labmates, colleagues and friends in the Chemical Engineering Department for the fun times and sharing your experience through valuable discussions. To my housemates, friends and family, thank you for listening to me discuss my project, even when you had no idea what I was talking about. Your continued support and companionship has been an important part of my grad school experience.

Table of contents

List of Figures

List of Tables

Nomenclature

Symbol	Description	Units
α	Pressure drop constant in equation 7.1	dimensionless
α_{air}	Fraction of excess air used in combustion of fuel	dimensionless
β	Fraction of upward or downward band radiation absorbed per unit height of furnace gas	m^{-1}
ε'	Differential emission coefficient in Koenigsberger equation 17	dimensionless
ε_r	Emissivity of refractory wall	dimensionless
ε_t	Emissivity of tubes	dimensionless
λ_c	Thermal conductivity of coke	$kW \cdot m^{-1}K^{-1}$
λ_g	Thermal conductivity of process gas	$kW \cdot m^{-1}K^{-1}$
λ_i	Thermal conductivity of component *i*	
λ_t	Thermal conductivity of the tube wall	$kW \cdot m^{-1}K^{-1}$
μ_g	Dynamic viscosity of process gas	Pa·s
μ_i	Dynamic viscosity of component *i*	
ρ_g	Average density of process gas	$kg \cdot m^{-3}$
σ	Stefan-Boltzmann constant	$kW \cdot m^{-2}K^{-4}$
τ	Fraction of radiation emitted as band radiation	dimensionless
A_c	Cross sectional area of radiant section	m^2
A_j	Pre-exponential factor for reaction *j*	$m^3 \cdot mol^{-1}s^{-1}$ or s^{-1}
A_r	Refractory wall surface area per unit volume of furnace gas	m^{-1}
A_t	Tube wall surface area per unit volume of furnace gas	m^{-1}
C_i	Concentration of coke precursor	$mol \cdot m^3$
$C_{p,air}$	Average heat capacity of air	$kJ \cdot kg^{-1}K^{-1}$
$C_{p,f}$	Heat capacity of furnace gas	$kJ \cdot kg^{-1}K^{-1}$
$C_{p,fuel}$	Heat capacity of fuel	$kJ \cdot kg^{-1}K^{-1}$
$C_{p,g}$	Heat capacity of process gas	$kJ \cdot kg^{-1}K^{-1}$
$C_{p,i}$	Heat capacity of component *i* in furnace gas	$kJ \cdot kg^{-1}K^{-1}$
D_i	Tube inner diameter	m
D_{ic}	Diameter at inner surface of coke layer	m
D_{lm}	Log mean diameter	m
D_o	Tube outer diameter	m
$E_{a,j}$	Activation energy of reaction j	$kJ \cdot mol^{-1}$
Fr	Friction factor inside tubes	dimensionless
$h_{conv+cond}$	Combined heat transfer coefficient for heat transferred through tube walls via conduction and to process gas via convection	$kW \cdot m^{-2}K^{-1}$

$h_{conv,g}$	Convective heat transfer coefficient between process gas and coke surface	$kW \cdot m^{-2}K^{-1}$
$\Delta H_{c,CH_4}$	Heat of combustion of methane	$kJ \cdot mol^{-1}$
$\Delta H_{c,fuel}$	Average heat of combustion of fuel	$kJ \cdot mol^{-1}$
$\Delta H_{c,H_2}$	Heat of combustion of hydrogen	$kJ \cdot mol^{-1}$
ΔH_{crack}	Enthalpy of reaction	$kJ \cdot mol^{-1}$
$H_{furnace}$	Height of the furnace	m
k_j	Rate constant for reaction *j* at temperature T_g	$m^3 \cdot mol^{-1}s^{-1}$ or s^{-1}
$\dot{m}_{air}$	Mass flow rate of combustion air to burners	$kg \cdot s^{-1}$
$\dot{m}_f$	Mass flow rate of furnace gas to the radiant section	$kg \cdot s^{-1}$
$\dot{m}_{fuel}$	Mass flow rate of fuel to all burners	$kg \cdot s^{-1}$
$\dot{m}_g$	Mass flow rate of process gas through a single tube	$kg \cdot s^{-1}$
$\dot{m}_{H_2O}:\dot{m}_{C_2H_6}$	Mass flow ratio of steam to ethane	dimensionless
MW_f	Average molecular weight of furnace gas	$kg \cdot mol^{-1}$
MW_{fuel}	Average molecular weight of fuel	$kg \cdot mol^{-1}$
MW_g	Average molecular weight of process gas	$kg \cdot mol^{-1}$
MW_i	Molecular weight of component *i*	$kg \cdot mol^{-1}$
n_p	Number of tubes passes per tube	dimensionless
n_s	Number of sections used for discretization	dimensionless
n_t	Number of tubes	dimensionless
$\dot{n}_f$	Upward molar flow rate of furnace gas	$mol \cdot s^{-1}$
$\dot{n}_{fuel}$	Molar flow rate of fuel to burners	$mol \cdot s^{-1}$
$\dot{n}_{i,f}$	Molar flow rate of component *i* in furnace gas	$mol \cdot s^{-1}$
P	Absolute pressure inside tubes	Pa
ΔP_{adj}	Adjusted pressure drop used for data collection	$Pa \cdot s \cdot kg^{-1}$
q^+	Rate of radiant flux in the positive direction	$kW \cdot m^{-2}$
q^-	Rate of radiant flux in the negative direction	$kW \cdot m^{-2}$
$\dot{Q}_{lost}$	Rate of heat lost at the burners	kW
$\dot{Q}_{transfer}$	Rate of heat transfer from furnace gas to process gas	kW
R	Ideal gas constant	$J \cdot mol^{-1}K^{-1}$
R_{bend}	Radius of bend in tube	dimensionless
Re_g	Reynolds number for process gas	$kg \cdot m^{-1}s^{-1}$
r_{ci}	Rate of free-radical coke formation	$kg \cdot m^{-2}h^{-1}$
r_{crack}	Reaction rate of ethane consumption	$mol \cdot m^{-3}s^{-1}$
r_i	Rate of reaction of component *i*	K
s_t	Tube wall thickness	m
T_c	Coke layer inner surface temperature	K
T_{comb}	Combustion gas temperature when it enters radiant section	K
T_f	Furnace gas temperature	K
T_{fuel}	Fuel temperature entering burners	K

T_g	Process gas temperature	K
T_{ref}	Reference temperature	K
T_{to}	Outer tube wall temperature	K
T_{ti}	Inner tube wall temperature	K
v_g	Process- gas velocity	$m \cdot s^{-1}$
$w_{C_2H_6,g}$	Mass fraction of ethane in process gas feed	dimensionless
$w_{H_2O,g}$	Mass fraction of steam in process gas feed	dimensionless
x	Position along reactor tube length	m
$x_{CH_4,fuel}$	Mole fraction of methane in fuel	dimensionless
$x_{H_2,fuel}$	Mole fraction of hydrogen in fuel	dimensionless
$x_{i,f}$	Mole fraction of component *i* in furnace gas	dimensionless
$x_{i,g}$	Mole fraction of component *i* in process gas	dimensionless
$x_{N_2,air}$	Mole fraction of nitrogen in air	dimensionless
$x_{O_2,air}$	Mole fraction of oxygen in air	dimensionless
$x_{Q_{lost}}$	Fraction of heat of combustion lost at burners	dimensionless
z	Vertical position within a furnace	m

List of Abbreviations

ACM – Aspen Custom Modeller®

CFD – Computational fluid dynamics

CSTR – Continuous stirred tank reactor

ODE – Ordinary differential equation

PDE – Partial differential equation

TLE – Transfer-line exchanger

USX – Ultra-selective exchanger

Chapter 1 – Introduction

1.1 Project background

Thermal cracking of hydrocarbons provides the majority of the worldwide annual commercial production of ethylene through a process commonly referred to as pyrolysis or steam cracking.[1] Endothermic reactions occur when gaseous feedstock (ethane, propane or butane) or liquid feedstock (naptha, vacuum gas oil, etc.) are fed through radiant coils in a gas-fired furnace to produce ethylene and other light olefins. The heat from flue gases outside of the radiant coils transfers through the tube walls to the process gas and leads to high rates of cracking within the tubes.[1] Steam is used as a diluent and increases the olefin selectivity by decreasing the partial pressure of the hydrocarbons.[2] Steam is also used to reduce coke formation through reactions between the steam and the coke layer that occur at high temperatures producing carbon monoxide and hydrogen.[3]

Coke is a solid material (primarily carbon) that deposits on the inner surfaces of the radiant coils. The rate of coke deposition depends on temperature and gas composition inside the tubes, as well as the composition of the temperature-resistant metal alloy used to manufacture the tubes.[4] Build-up of a coke layer leads to a decrease in inner tube diameter, which increases the pressure drop over the length of the reactor and decreases ethylene selectivity due to higher average reactor pressure. Figure 1 shows a tube that has been fouled by coke formation.

Figure 1 – Radiant coil with significant coke formation

The layer of coke formed on the tube walls also inhibits heat transfer from combustion gases to the reactor contents. As a result, the external temperature must be increased to provide the same amount of heat to the reacting mixture.[5] Coke deposition can also lead to coil damage due to hot spots and corrosion.[6]

When the tube wall temperature or reactor pressure becomes too high, the furnace must be temporarily taken out of production and subjected to a decoking process. During decoking, the coke can be removed via controlled combustion using a mixture of steam and air.[7] This process leads to an important reduction in production capacity due to the furnace being taken off-stream to perform decoking, as well as high maintenance and operating costs and shortened coil life due to the thermal cycling of the coil.[8] A model that can accurately simulate coke formation and decoking duration would serve to optimize the decoking process, increase production capacity and decrease operating and maintenance costs.[5,7]

1.2 Project objectives and outline

The objective of the research described in the current thesis is to create a steady-state model of the radiant section of an ethane pyrolysis furnace of interest to NOVA Chemicals. The model assumes a floor-fired burner configuration and considers the initial operation in a coke-free tube. The model will be able to predict the process gas temperature, process gas pressure and composition profiles over the length of the radiant section. This project is part of a larger overall research project that aims to create a dynamic model of the entire ethane pyrolysis unit. The larger model will account for the formation of a coke layer over time, and will predict changes in furnace behavior in response to coke deposition, dynamic plant disturbances, and contaminants in the feed stream. It will also be able to simulate the decoking process. Parameter estimation and industrial operating data will be used to tune this model. A process flow diagram of the pyrolysis unit is provided in Figure 2, showing the four main sections of the unit: i) convection section, ii) radiant section, iii) ultra-selective exchanger (USX) and iv) transfer-line exchanger (TLE).

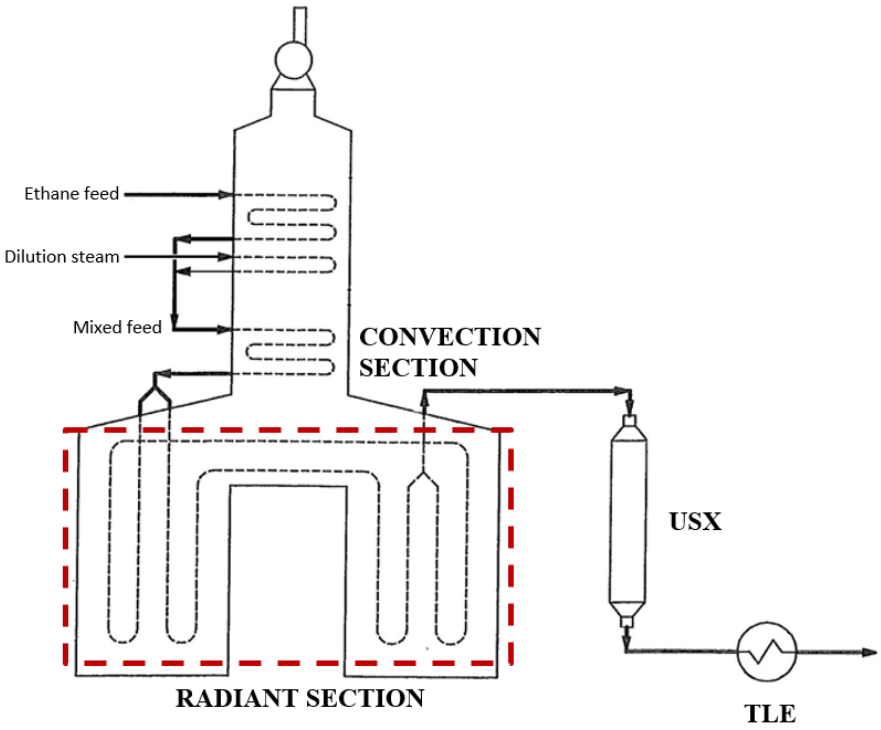

Figure 2 – Ethane pyrolysis unit process flow diagram

The scope of this thesis is limited to the radiant section, highlighted by the dotted line in Figure 2. The information in this thesis is organized as follows: Chapter 2 provides a review of the ethane cracking, coke formation and heat transfer literature; Chapter 3 describes the development of the model; Chapter 4 describes the implementation of the model into the chosen PREDICI® software; Chapter 5 shows some simulation results and sensitivity analysis. Conclusions and recommendations for future work are provided in Chapter 6.

Chapter 2 – Literature review

2.1 Ethane pyrolysis

Ethane cracking takes place in the radiant section of the furnace, after the feedstock has been diluted with steam and passed through the convection section for pre-heating. Low

rates of reaction occur in the convection section, but the desired cracking temperature is not reached until the process gas reaches the radiant section of the furnace.[9] Ranjan et al. report that temperatures in the radiant section of industrial cracking furnaces typically increase from 525°C to 1125°C and that, to limit coke formation, reactants are only exposed to these elevated temperatures for a short residence time.[9]

Many reaction mechanisms have been proposed for simulation of ethane cracking over the last half century. It is well established that the overall reactions proceed via free-radical mechanisms involving initiation, propagation or hydrogen abstraction, and termination steps. Because detailed free-radical mechanisms lead to complex systems of differential equations, simplified molecular schemes have been more commonly used for design and simulation purposes.[9] The molecular reaction scheme proposed by Sundaram and Froment has been widely adopted because it was the most accurate kinetic scheme, even though it does not account for the formation of higher-molecular-weight components.[1] Recently, Ranjan et al.[9] proposed the addition of six reactions to the Sundaram and Froment scheme and reported better simulation results. The molecular scheme proposed by Ranjan et al. is presented in Table 1. Reactions 1 to 5 were included in the original Sundaram and Froment scheme and reactions 6 to 11 are the reactions added by Ranjan et al.

Table 1 – Ethane cracking molecular reaction scheme[9]

$$C_2H_6 \underset{k_{1r}}{\overset{k_1}{\rightleftharpoons}} C_2H_4 + H_2 \quad \textbf{1}$$

$$C_3H_6 \underset{k_{2r}}{\overset{k_2}{\rightleftharpoons}} C_2H_2 + CH_4 \quad \textbf{2}$$

$$C_2H_2 + C_2H_4 \xrightarrow{k_3} C_4H_6 \quad \textbf{3}$$

$$2C_2H_6 \xrightarrow{k_4} C_3H_8 + CH_4 \quad \textbf{4}$$

$$C_2H_4 + C_2H_6 \xrightarrow{k_5} C_3H_6 + CH_4 \quad \textbf{5}$$

$$C_2H_4 + C_4H_6 \xrightarrow{k_6} C_6H_6 + 2H_2 \quad \textbf{6}$$

$$C_3H_8 \underset{k_{7r}}{\overset{k_7}{\rightleftharpoons}} C_3H_6 + H_2 \quad \textbf{7}$$

$$C_3H_8 + C_2H_4 \xrightarrow{k_8} C_2H_6 + C_3H_6 \quad \textbf{8}$$

$$2C_3H_6 \xrightarrow{k_9} 3C_2H_4 \quad \textbf{9}$$

$$C_4H_{10} \underset{k_{10r}}{\overset{k_{10}}{\rightleftharpoons}} C_4H_8 + H_2 \quad \textbf{10}$$

$$C_3H_6 + C_2H_6 \xrightarrow{k_{11}} C_4H_8 + CH_4 \quad \textbf{11}$$

Although computations are much simpler when a molecular reaction scheme like the one in Table 1 is used to develop mathematical models, it has been shown that radical reactions are significant for prediction of coke formation. Therefore, there is an incentive to model coke formation in a more detailed way that explicitly considers free-radical reactions. There are over 2000 possible radical reactions that take place during pyrolysis of hydrocarbons, so it is important to determine which reactions are most important for the pyrolysis of ethane.[10] An increase in available kinetic data occurred with advances in kinetic theory and experimental techniques, along with the advent of large computers

capable of solving the complex sets of equations associated with these detailed reaction mechanisms.[10]

Sundaram and Froment described the free-radical mechanisms associated with the pyrolysis of paraffins, olefins and mixtures thereof.[11] Their reaction scheme for ethane pyrolysis considers 49 reactions which account for 20 species, 11 of which are molecular species and 9 of which are radical species. In their model, any of the products that are heavier than C_5H_{10} have been lumped into a single species C_5^+, and radicals heavier than C_5H_{11} are not considered. Although Sundaram and Froment recognized that aromatics and naphthenic species are possible reaction products, these species were omitted from their model to keep the model relatively simple and because there was a lack of available kinetic data.[11] The kinetic data used by Sundaram and Froment were taken from a number of different sources.[12–17] Many of their kinetic parameters were determined at low temperatures and pressures and therefore adaptation of these parameters was found to be necessary when simulating operation at industrial temperatures and pressures. Selected parameters were adjusted by Sundaram and Froment using trial-and-error methods to produce predictions that matched the industrial data.[11]

The model presented by Sundaram and Froment accounts for only the major reactions and a fraction of the minor reactions that have been reported in literature.[11] There are a number of other available publications with a wider or varied array of reaction mechanisms and kinetics.[10,12,13] One of the most widely utilized models is in industry is SPYRO® created by Technip S.A. This software is currently employed by NOVA Chemicals and other companies in the ethylene industry for feedstock selection, operability studies, real-time optimization, advanced process control, and planning and

scheduling.[18] The simulation is based on a rigorous kinetic scheme of about 3,000 equations involving 128 hydrocarbon species. SPYRO® claims to have the ability to accurately predict yield patterns for a wide variety of feedstocks from gases to gas oils at industrial operating conditions.[18] As SPYRO® is a commercial product, the kinetic scheme employed for ethane cracking is neither published nor available to the model user.

2.2 Coke formation

The formation of coke on coil surfaces during the thermal cracking of hydrocarbons has long been one of the main problems in olefin production.[19] Industrial operating conditions, residence time, diluent, coke inhibitors, tube coatings and tube metallurgy are all considered in attempts to limit coke formation. However, time spent in decoking cycles still represents a significant loss of ethylene production.[8] Coke formation does not significantly affect the reactor mass balance, or product composition. However, its effects on heat transfer and pressure drop have such strong industrial implications that it is very desirable to have a model that can accurately predict the extent of coke formation.[20]

Early coke formation models were based on experimental results where crude methods, such as weighing the reactor, were used to track the coke formation on the tube walls over time. Such methods allowed only for the calculation of an average weight gain over time, and therefore could not consider the coke profile along the length of a tubular reactor.[21] Coke deposits are generally greatest at or near the downstream end of the coil, so an average profile along the length of the reactor is likely not an accurate representation.[22] Sundaram and Froment[21] proposed a novel approach to track coke

formation over time using an electrobalance and a well-mixed reactor. They investigated both propane and ethane feedstocks and reported run lengths, coke thickness and tube wall temperature profiles that were in agreement with industrial data.[23] Other authors have performed similar experiments with a variety of feedstocks and have come up with kinetic expressions and parameter values for coke formation rates based on their empirical data.[22,24–27] Characterization of coke, however, suggests that there are multiple mechanisms that lead to coke formation that are not explicitly accounted for in these empirical correlations of coke formation.[28]

Examination of coke layers produced during ethane cracking on both a laboratory and industrial scale, shows that the coke structure varies with the build-up of a coke layer. The coke closest to the metal surface is rough and porous because it is formed from thickened coke filaments. This filamentous coke transitions into a solid, non-porous middle layer of coke. The upper surface of the coke layer is once again rough and porous.[4] Analysis of the coke layer using a scanning-electron microscope (SEM) also showed that metal particles were present throughout the coke layer, but at a higher weight percentage in the filamentous regions.[4]

To account for these changes in coke structure, Albright and Marek[28] proposed three mechanisms for coke formation: i) catalytic coke formation, ii) free-radical coke formation, and iii) droplet condensation. Droplet condensation occurs in the bulk phase of the reactor where large hydrocarbon molecules condense to form tar droplets that adhere to the surface and become incorporated in the coke layer.[19] This reaction is of particular importance in the low temperature TLE section of the furnace (see Figure 2) and when heavier feedstocks such as naphtha are cracked. With a light feedstock, such as ethane,

droplet condensation is of negligible importance, even in the lower temperature sections of the process.[8]

2.2.1 Catalytic coke formation

Catalytic coke formation accounts for the layer of filamentous coke that is formed on the surface of the tube walls. It favours a clean metal surface, or oxidixed surface after decoke, and occurs at temperatures from about 400 °C to about 1050 °C.[28] During start-up, reacting gases are in direct contact with the metal surface of the tube walls. Hydrocarbon molecules from the reacting gas are attracted to the metal surface where they are chemisorbed on the metal crystallite and undergo a surface reaction to produce carbon. These carbon atoms diffuse into the metal crystals and cause separation of the metal particles, lifting them from the surface. As more carbon is deposited, coke filaments form, carrying metal particles within them and at their tip. These metal particles are active sites in catalytic coke formation.[6] The result is a porous layer of interwoven filaments that covers the metal surface and contains about 1-2 wt% metal. The rate of catalytic coke formation decreases quickly as the surface of the metal is covered with coke.[6]

A number of kinetic models for catalytic coke formation were investigated by Mohamadalizadeh et al.[6] and compared to experimental data reported by Kumar and Kunzru.[24] The coke formed at the beginning of the coke formation process was considered as coke formed by catalytic mechanisms. The fourth mechanism presented by Mohamadalizadeh et al.[6] provided the best match to experimental data and is as follows:

$$X + S \underset{k_1'}{\overset{k_1}{\rightleftarrows}} XS \quad \textbf{12}$$

$$XS \xrightarrow{k_2} CS + nH_2 \quad \textbf{13}$$

$$CS \xrightarrow{k_3} eS + fC + gCS \quad \textbf{14}$$

where X represents the hydrocarbon molecule precursor, S the active sites, C the carbon that diffuses into the metal crystal and CS the produced carbon on the metal surface, which is considered as the catalytic coke. The stoichiometric coefficients *e*, *f*, and *g* are used to distinguish between the carbon that diffuses into the metal, the carbon that remains on the surface as coke and the active sites that are released. The values for rate constants k_1, k_1', k_2 and k_3, as well as activation energies and coefficients *e*, *f*, and *g* are reported in Table 2 below for a generic hydrocarbon.

Table 2 – Parameter values for catalytic coke formation[6]

Parameter		Value	
k			
	k_1	2.14×10^{3}	$m^2 \cdot mol \cdot s^{-1}$
	k_1'	2.60×10^{-11}	$m^2 \cdot m^{-3} \cdot s^{-1}$
	k_2	6.26×10^{1}	s^{-1}
	k_3	4.91×10^{1}	s^{-1}
E			
	E_1	-1.16×10^{3}	$J \cdot mol^{-1}$
	E_1'	1.32×10^{4}	$J \cdot mol^{-1}$
	E_2	7.48×10^{-3}	$J \cdot mol^{-1}$
	E_3	7.34×10^{-3}	$J \cdot mol^{-1}$
e		0.107	
f		0.2	
g		0.182	

The values of activation energies and stoichiometric coefficients presented by Mohamadalizadeh et al.[6] in Table 2, although are shown to provide good model predictions, raise questions in their physical validity. It is unusual that the activation

energy E_1 has a negative value, and that the activation energies E_2 and E_3 are so small that their associated reactions are essentially independent of temperature. It is also strange to have different values for the coefficients *e* and *f*, and that the coefficients *e*, *f*, and *g* do not sum to a value of one.

2.2.2 Free-radical coke formation

Free-radical coke formation makes up the majority of the coke deposition in the radiant section and results in thickening of the coke filaments formed during catalytic coke formation.[28] Free-radical coke formation depends on the presence of active sites on the catalytic coke surface resulting from hydrogen abstractions. These active sites are surface radicals where coke precursors react and then follow a sequence of dehydrogenation and cyclization reactions to incorporate the carbon atoms of the coke precursor into the coke layer. The active site is regenerated after the carbon has been deposited. The number of carbon atoms added to the coke layer is equal to the number of carbon atoms in the coke precursor.[19]

A lack of reliable information on the coking rates for individual hydrocarbons has hindered the development of fundamental models.[26] If all possible reaction pathways for free-radical coke formation were considered, it would lead to an unrealistically high number of kinetic parameters and parameter estimation would be inaccurate if not impossible.[29] Species that could be considered important precursors to coke formation are i) olefins, ii) unsaturates and iii) aromatics. Unsaturates are products of pyrolysis reactions so they are in high concentrations in the process gas stream. They are reactive and are good candidates for radical addition[19] rendering them important precursors for free-radical coke formation in naptha, propane and ethane feeds.[19,20,23,26,29,30] Aromatics

have a ring structure that is similar to the structure of the coke matrix and branched aromatics are reactive components, especially at cracking temperatures.[19] Aromatics have been reported as important precursors to coke formation with naptha feedstocks.[19,20,26,29]

The rate of free-radical coke formation depends on the concentration of free radicals on the coke surface. The free radicals are mostly formed by hydrogen being abstracted from the surface by radicals in the process gas. The most abundant and reactive of these radicals are H· and CH_3·, which become H_2 and CH_4 after the abstraction of hydrogen. Therefore, Reyniers et al.[19] report that the concentration of free radicals on the coke surface can be approximated as the concentration of H_2 and CH_4 in the process gas stream giving the following rate of free-radical coke formation:

$$r_{ci} = [\mathrm{H_2}][\mathrm{CH_4}]k_i C_i \qquad \textbf{15}$$

where k_i is the rate constant for a given coke precursor and C_i is concentration of that coke precursor. Coke precursors are classified into groups depending on their characteristic function. Precursors of the same group are considered to have the same activation energy as shown in Table 3.

Table 3 – Free-radical coke formation kinetic parameters

	$\boldsymbol{k_i}$ (kg coke·m^{7}hr^{-1}mol^{-3})	$\boldsymbol{E_a}$ (J·mol^{-1}K^{-1})
Olefins	7.8589 x 10^8	7.4164 x 10^4
Butadiene	2.099 x 10^{12}	1.2794 x 10^5
Aromatics	4.1865 x 10^8	2.9977 x 10^4

2.3 Heat transfer

The endothermic cracking reactions that take place inside the radiant section of the furnace require heat to be transferred to the coils from the surrounding hot flue gases. Ideal cracking temperatures are reached between 525 °C and 1025 °C.[9] At such temperatures, cracking reactions occur rapidly and furnaces are designed to limit the amount of time that the reacting gases spend at these high temperatures to limit coke formation. Typically, process gases are preheated before they are diluted with steam and then the mixed gases are sent through the convection section of the furnace for further preheating before moving to the radiant section (see Figure 2). Upon exiting the radiant section, the process gases are rapidly cooled in a TLE. Some furnace configurations also have a USX between the outlet of the radiant section and the TLE.

The main type of heat transfer from the combustion side of the furnace into the tubes (where cracking occurs) is radiant heat transfer. Modeling radiant heat transfer is complex and often requires a high computational cost. Radiant heat transfer in furnaces has been modeled in a variety of ways ranging from full computational fluid dynamic (CFD) models to the Roesler flux method and the Hottel zone method.[31–35] For the purposes of the current model, using a CFD approach would be too complicated and computationally intensive.

The flux method reported by Roesler[36], which was initially used for modeling radiative heat transfer in a steam-naptha reforming process, is based on work by astrophysicists Schuster[37] and Schwarzschild[38]. The concept is to decompose radiation fields into a finite number of beams, whose intensity changes can be represented by ordinary differential equations (ODEs). In the furnace modeled by Roesler, as well as in typical

thermal cracking furnaces, the main flux of radiation occurs in the vertical direction (furnace height), and the ODEs are with respect to the vertical coordinate, z.[36]

When using the Roesler flux method, it is common to consider two directions (up and down) and two "colours" of radiation (band and window). Band radiation is radiation that can be absorbed by the gas, and window radiation is radiation that always passes unaffected through the gas.[36] The density of energy flow (typically in $kW \cdot m^{-2}$) from a radiating surface is given by the Stefan-Boltzmann expression:

$$\varepsilon \sigma T^4 \quad \textbf{16}$$

where the emissivity coefficient ε is a property of the surface, σ is the Stephan-Boltzmann constant and T is the absolute temperature of the surface.[36]

The amount of energy radiated by a volume element of gas (in $kW \cdot m^{-3}$) is given by the Koenigsberger equation:[39]

$$dq = 4\varepsilon' \sigma T^4 dV \quad \textbf{17}$$

where the differential emission coefficient ε' is equal to:

$$\varepsilon' = \frac{\tau \beta}{2} \quad \textbf{18}$$

and τ represents the fraction of total radiation emitted by a black body that is emitted as band radiation and β is the volumetric absorption coefficient of the gas (in m^{-1}).[36] Roesler's flux method was applied by Siddall and Selçuk to an eight-pass process gas heater.[40] In their radiation balances they assumed the furnace gas to be a grey gas, eliminating window radiation. This is thought to be a good assumption because soot, an important constituent of flames, emits continuously over all wavelengths.[41] This grey gas assumption reduces the Roesler flux method into two radiant fluxes, one in the

upward (positive) direction, q^+ and one in the downward (negative) direction q^-. The ODEs presented by Siddall and Selcuk are:

$$\frac{dq^+}{dz} = \beta\sigma {T_f}^4 + \frac{\varepsilon_t A_t \sigma}{2} \frac{\sum_{i=1}^{n_p} {T_{to,i}}^4}{n_p} - \left(\beta + \frac{\varepsilon_r A_r}{4} + \frac{\varepsilon_t A_t}{2}\right) q^+ + \frac{\varepsilon_r A_r}{4} q^- \quad \textbf{19}$$

$$-\frac{dq^-}{dz} = \beta\sigma {T_f}^4 + \frac{\varepsilon_t A_t \sigma}{2} \frac{\sum_{i=1}^{n_p} {T_{to,i}}^4}{n_p} - \left(\beta + \frac{\varepsilon_r A_r}{4} + \frac{\varepsilon_t A_t}{2}\right) q^- + \frac{\varepsilon_r A_r}{4} q^+ \quad \textbf{20}$$

The first term on the right-hand side of equation 19 is the radiant energy emitted by the gas in the upward direction, the second term is the radiant energy emitted by the tube walls where n_p is the number of tube passes and A_t is the total tube surface area per unit volume of furnace gas. This term is the average upward radiant flux (per unit height) from all of the tube surfaces at height *z*. Different tube passes have different tube surface temperatures T_{to} at a given height *z*. The third term (in brackets) accounts for the incident radiation in the positive direction that is being absorbed by the gas, the refractory wall and the tube surfaces. Note that ε_r is the emissivity of the refractory and A_r is the surface area of the refractory wall per unit volume of furnace gas. The final term on the right-hand side of equation 19 is the incident radiation arriving from the negative direction that is absorbed by the refractory and then emitted in the positive direction. The terms in equation 20 are analogous to those in equation 19.

These radiation balance equations were combined with an energy balance on the furnace gas and with energy and material balances on the process gas to simulate the behaviour of the furnace at steady state. Accumulation of heat within the tube walls was neglected so that algebraic equations could be used to compute the inner and outer tube wall temperatures.[40] The Roesler flux method has also been used successfully to model

process gas heaters,[42] steam-methane reformers,[43] and Midrex reformers.[32] It is preferred to the more complicated Hottel zone method for modeling radiative heat transfer when ODEs are preferred compared to a large number of algebraic equations. The Hottel zone method is preferred in situations where radiative heat transfer is important in two or three dimensions and complex effects of furnace geometry on radiative heat transfer are of interest to the modeler.[44]

In summary, there is an abundance of kinetic data for ethane pyrolysis available in literature. There are over 2000 possible reactions and it must be determined which reactions and associated species are most important to include in the proposed model.[10] SPYRO® is the current industrial standard for ethane pyrolysis simulations used by NOVA Chemicals and other companies, and is reported to provide good predictions for typical operating conditions.[10,18] SPYRO® simulations provide a useful reference point to evaluate the reaction products of ethane pyrolysis. However, SPYRO® may use empirical correlations or other proprietary methods and assumptions to model coke formation, which may not be accurate for predicting coke formation over a wide range of operating conditions. The proposed model is being developed because SPYRO® models, due to their proprietary information, cannot be adapted and improved to accurately predict the influence of unusual operating conditions or disturbances that are of interest to research scientists, plant operators and process engineers. Also, SPYRO® is not capable of modeling dynamic operation, which the proposed model will be extended to be capable of simulating in future work.[45]

The study of coke layers has led to the categorization of coke depending on its physical structure. For each resulting physical structure of coke, there is assumed to be a different

formation mechanism. Catalytic coke forms a filamentous layer, free-radical coke forms an amorphous layer, and droplet condensation results in spherical particles of coke. Although these mechanisms are generally understood and accepted, most coke-formation models do not distinctly account for the different types of coke formation. These models instead use general empirical correlations.[22,24–27] The available kinetic data for each type of coke formation are limited and, to my knowledge, a model that can accurately predict dynamic coke formation based on fundamental mechanisms is not available in literature.

Chapter 3 – Model development

3.1 Model overview

The model presented in this work has been developed specifically for a Stone and Webster Induced Draft furnace like the one operated by NOVA Chemicals in Joffre, Alberta (see Figure 2). Operational data including flow rates, pressures, compositions and temperatures are available for model development, parameter estimation and model validation. The data are collected by plant instruments in real time and are stored in a historical database. These data values can be accessed using ASPEN Process Explorer®. Apart from storing and accessing the measured values, ASPEN Process Explorer® can be used directly to collect properties such as density-corrected flow rates, which are calculated in real time.

The radiant section is the focus of this work. It is divided into two parts called the *cold box* and the *hot box*. The process gas passes first through the cold box, where the process gas temperatures are lower, and then into the hot box where the process gas temperatures

are increased by heat transfer from the surrounding furnace gases into the tubes. In the current model, the cold box and the hot box are assumed to have floor-fired burners that provide heat to the furnace gases through combustion of methane and hydrogen. Future modeling work will consider side-fired furnace heating, where the combustion heat is provided more uniformly over the height of the cold box and the hot box. A depiction of a single tube through the radiant sections of a bottom-fired and a side-fired furnace are shown in Figure 3.

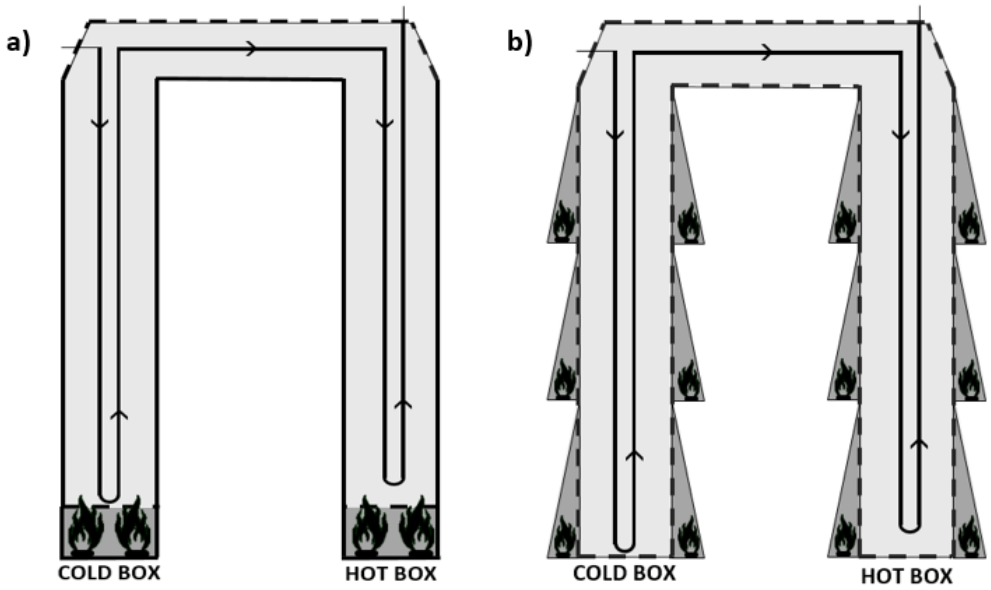

Figure 3 – Front view of the radiant section of a) a floor-fired furnace and b) a side-fired furnace

The radiant section consists of 16 coils with the same geometry in an inline arrangement with a front view as shown in Figure 3. Each coil has a downward and upward pass in the cold box and a downward and upward pass in the hot box. The cold-box and hot-box passes are connected by a cross-over tube. NOVA Chemicals operates a variety of furnaces, some are bottom fired and some are side fired as shown in Figure 3. The floor-fired furnaces have burners that sit on the floor of the radiant section. The side-fired furnaces have three terraces along each side of the hot box and the cold box, and the

burners sit on these terraces. There are only four sets of burners (in the into-the-page direction), so a single set of burners provides heat to four radiant coils. This arrangement can be seen in the top view of the cold box of the radiant section depicted in Figure 4.

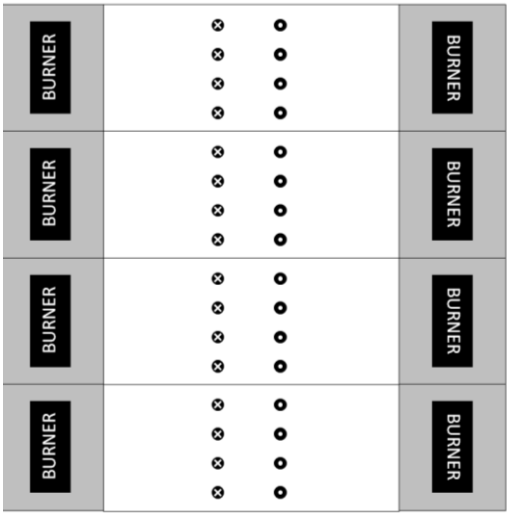

Figure 4 – Top view of radiant-section cold box

Since the furnace configuration contains 16 geometrically identical coils, it is assumed that they all follow the same temperature, pressure and reaction profile as listed as assumption 4.1 in Table 4. Therefore, the model is developed for a single tube, treated as a plug-flow reactor, operating at steady-state. The single tube accounts for a sixteenth of the total furnace throughput.

Table 4 – Assumptions made in model development and implementation

4.1	All 16 tubes in the furnace are fed the same composition and mass of diluted ethane feed and follow the same temperature, pressure and reaction profile. As a result, the model can focus on a single tube.
4.2	All burners will burn the same mass of fuel with the same composition and same fraction of excess air.
4.3	Ethane cracking reactions are elementary so their order corresponds to the molecularity.
4.4	Rate constants follow Arrhenius law in the temperature range of interest.
4.5	The flow in the tubes is perfect plug-flow.
4.6	The heat generated or consumed by reactions within the tubes can be neglected, except for the heat effects associated with the three reactions in Table 5 that consume ethane.
4.7	The thermal conductivity of coke does not depend on temperature.
4.8	Steam is an inert diluent.
4.9	Furnace gas is grey and non-scattering.
4.10	Convective and conductive heat transfer are negligible on the furnace gas side of the radiant section compared to the radiative heat transfer.
4.11	There is no temperature variation in the horizontal direction within the cold box or within the hot box.
4.12	The volume occupied by the tubes in the radiant section is negligible compared to the volume occupied by the furnace gas.
4.13	Combustion of fuel goes to completion due to the presence of excess air.
4.14	There is no coke within the tubes (for this initial version of the model) because the model is simulating process operation immediately after decoking. Also, there has been no spalling of coke particles from any upstream section into the radiant section.
4.15	The combusted furnace gas enters the bottom of the radiant section at the combustion temperature T_{comb} in floor-fired operation.
4.16	The radiant section is perfectly insulated and heat loss to the surroundings occurs only at the burners, influencing the value of T_{comb}.
4.17	The rate of heat loss at each burner is the same.
4.18	The refractory walls are grey and radiatively adiabatic, and cover the top and bottom of the radiant section.
4.19	Concentrations of radical species in the process gas are low at every given position. The presence of these radical species has a negligible effect on the heat capacity of the process gas.
4.20	Process gas acts as an ideal gas at the temperatures and pressures in the radiant section.
4.21	The flow of furnace gas through the radiant section is directly upward in perfect plug-flow. The furnace gas that enters in the cold box leaves at the top of the cold box and the furnace gas that enters in the hot box leaves at the top of the hot box.
4.22	The tube passes in the radiant section run the entire length between the top and bottom refractory walls. Any reactions that occur in the short U-bends can be neglected. Significant reactions do occur in the horizontal lengths of tubes (i.e.,

	the cross-over tubes) between the cold box and the hot box. The rate of radiant heat transfer to the cross-over tubes can be determined using radiant fluxes at the corresponding height in the cold box.
4.23	When computing the radiant flux profiles and the temperature profile for the furnace gas, the only reaction (and associated heat effects) that needs to be considered within the tubes is the overall ethane cracking reaction (reaction 52 on page 68).

To enable future model improvements, the model equations are derived assuming that a coke layer with a specified thickness profile along the tube may already exist. As a result, steady-state simulations could be performed to investigate the influence of the coke that is already deposited in the tubes. A cross-section of the tube considered in model development is shown in Figure 5, along with labels for the diameters and temperatures at different positions.

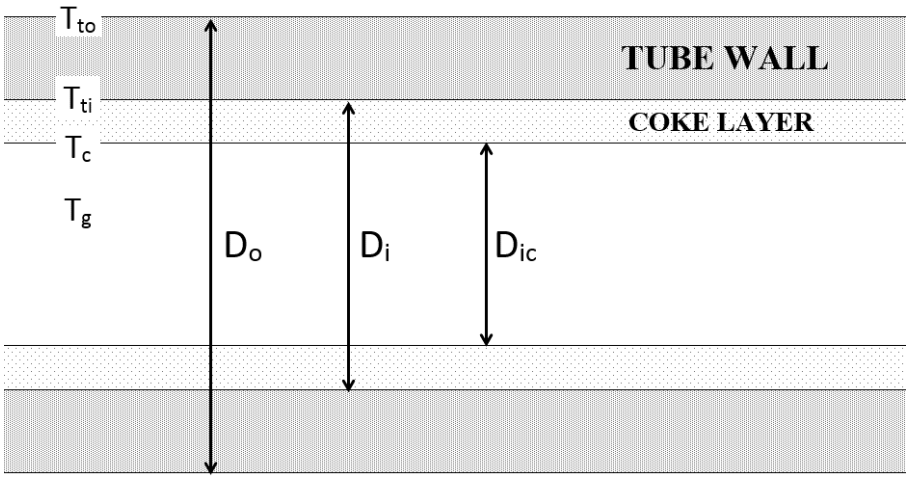

Figure 5 – Cross setion of a short piece of radiant section tube

3.2 Process-side model development

3.2.1 Reaction kinetics

The free-radical reaction scheme proposed by Sundaram and Froment for the cracking of ethane is an appropriate starting point for the development of a reasonable kinetic model for industrial use. The model proposed by Sundaram and Froment does not include the

formation of aromatic and naphthenic radicals and species due to a lack of kinetic data available at the time of publication.[11] The results of SPYRO® simulations indicate that appreciable low levels of aromatic and naphthenic species and radicals are expected during the thermal cracking of ethane at typical operating conditions. Therefore, reasonable mechanisms and kinetics for the formation of these species are included, based on information from other studies.[10–12,14,15,46,47] Also, Sundaram and Froment group all species with molecular weights higher than C_5H_{10} together, so SPYRO® simulations were used to determine which higher-molecular-weight species may be important. After extending the Sundaram and Froment model to account for important species indicated by SPYRO® simulations, the resulting 56 reactions in Table 5 were chosen for implementation in PREDICI®.

Table 5 – Ethane pyrolysis free-radical reaction scheme

Reaction	Ref.	No.
$C_2H_6 \xrightarrow{k_1} 2CH_3\cdot$	[11]	**3.1**
$1\text{-}C_4H_8 \xrightarrow{k_2} C_3H_5\cdot + CH_3\cdot$	[12]	**3.2**
$n\text{-}C_4H_{10} \xrightarrow{k_3} 2C_2H_5\cdot$	[11]	**3.3**
$n\text{-}C_4H_{10} \xrightarrow{k_4} 1\text{-}C_3H_7\cdot + CH_3\cdot$	[11]	**3.4**
$C_2H_4 + H\cdot \xrightarrow{k_5} C_2H_3\cdot + H_2$	[11]	**3.5**
$C_2H_6 + H\cdot \xrightarrow{k_6} C_2H_5\cdot + H_2$	[11]	**3.6**
$C_2H_4 + CH_3\cdot \xrightarrow{k_7} C_2H_3\cdot + CH_4$	[11]	**3.7**
$C_2H_6 + CH_3\cdot \xrightarrow{k_8} C_2H_5\cdot + CH_4$	[11]	**3.8**
$C_2H_5\cdot + H_2 \xrightarrow{k_9} C_2H_6 + H\cdot$	[10]	**3.9**
$C_2H_4 + C_2H_5\cdot \xrightarrow{k_{10}} CH_3\cdot + C_3H_6$	[11]	**3.10**
$C_2H_2 + H\cdot \xrightarrow{k_{11}} C_2H_3\cdot$	[11]	**3.11**
$C_2H_4 + H\cdot \xrightarrow{k_{12}} C_2H_5\cdot$	[11]	**3.12**

$C_3H_6 + H\cdot \xrightarrow{k_{13}} 1\text{-}C_3H_7\cdot$	[11]	**3.13**
$C_3H_4 + H\cdot \xrightarrow{k_{14}} C_3H_5\cdot$	[10]	**3.14**
$C_4H_6 + H\cdot \xrightarrow{k_{15}} C_4H_7\cdot$	[14]	**3.15**
$C_2H_4 + CH_3\cdot \xrightarrow{k_{16}} 1\text{-}C_3H_7\cdot$	[11]	**3.16**
$C_2H_4 + C_2H_3\cdot \xrightarrow{k_{17}} C_4H_7\cdot$	[11]	**3.17**
$C_4H_6 + C_2H_3\cdot \xrightarrow{k_{18}} CH_3\cdot + cyC_5H_6$	[46]	**3.18**
$C_4H_6 + C_2H_3\cdot \xrightarrow{k_{19}} C_6H_6 + H_2 + H\cdot$	[46]	**3.19**
$C_2H_4 + C_2H_5\cdot \xrightarrow{k_{20}} 1\text{-}C_4H_9\cdot$	[11]	**3.20**
$C_3H_6 + C_2H_5\cdot \xrightarrow{k_{21}} C_5H_{11}\cdot$	[11]	**3.21**
$C_2H_4 + 1\text{-}C_3H_7\cdot \xrightarrow{k_{22}} C_5H_{11}\cdot$	[11]	**3.22**
$1\text{-}C_4H_9\cdot \xrightarrow{k_{23}} 2\text{-}C_4H_9\cdot$	[46]	**3.23**
$2\text{-}C_4H_9\cdot \xrightarrow{k_{24}} 1\text{-}C_4H_9\cdot$	[46]	**3.24**
$C_2H_3\cdot \xrightarrow{k_{25}} C_2H_2 + H\cdot$	[11]	**3.25**
$C_2H_5\cdot \xrightarrow{k_{26}} C_2H_4 + H\cdot$	[11]	**3.26**
$C_3H_5\cdot \xrightarrow{k_{27}} C_2H_2 + CH_3\cdot$	[11]	**3.27**
$C_3H_5\cdot \xrightarrow{k_{28}} C_3H_4 + H\cdot$	[10]	**3.28**
$1\text{-}C_3H_7\cdot \xrightarrow{k_{29}} C_2H_4 + CH_3\cdot$	[11]	**3.29**
$1\text{-}C_3H_7\cdot \xrightarrow{k_{30}} C_3H_6 + H\cdot$	[11]	**3.30**
$1\text{-}C_4H_7\cdot \xrightarrow{k_{31}} C_4H_6 + H\cdot$	[11]	**3.31**
$1\text{-}C_4H_7\cdot \xrightarrow{k_{32}} C_2H_4 + C_2H_3\cdot$	[11]	**3.32**
$1\text{-}C_4H_9\cdot \xrightarrow{k_{33}} C_2H_4 + C_2H_5\cdot$	[11]	**3.33**
$1\text{-}C_4H_9\cdot \xrightarrow{k_{34}} 1\text{-}C_4H_8 + H\cdot$	[11]	**3.34**
$2\text{-}C_4H_9\cdot \xrightarrow{k_{35}} C_3H_6 + CH_3\cdot$	[47]	**3.35**
$C_5H_{11}\cdot \xrightarrow{k_{36}} cyC_5H_{10} + H\cdot$	[11]	**3.36**
$C_5H_{11}\cdot \xrightarrow{k_{37}} 1\text{-}C_4H_8 + CH_3\cdot$	[11]	**3.37**
$C_5H_{11}\cdot \xrightarrow{k_{38}} C_2H_4 + 1\text{-}C_3H_7\cdot$	[11]	**3.38**

$C_2H_3\cdot + H\cdot \xrightarrow{k_{39}} C_2H_4$	[11]	**3.39**
$C_2H_5\cdot + H\cdot \xrightarrow{k_{40}} C_2H_6$	[15]	**3.40**
$C_3H_5\cdot + H\cdot \xrightarrow{k_{41}} C_3H_6$	[11]	**3.41**
$1\text{-}C_3H_7\cdot + H\cdot \xrightarrow{k_{42}} C_3H_8$	[11]	**3.42**
$1\text{-}C_4H_7\cdot + H\cdot \xrightarrow{k_{43}} 1\text{-}C_4H_8$	[11]	**3.43**
$1\text{-}C_4H_9\cdot + H\cdot \xrightarrow{k_{44}} n\text{-}C_4H_{10}$	[11]	**3.44**
$CH_3\cdot + CH_3\cdot \xrightarrow{k_{45}} C_2H_6$	[11]	**3.45**
$C_2H_5\cdot + CH_3\cdot \xrightarrow{k_{46}} C_3H_8$	[11]	**3.46**
$C_3H_5\cdot + CH_3\cdot \xrightarrow{k_{47}} 1\text{-}C_4H_8$	[11]	**3.47**
$C_2H_3\cdot + C_2H_3\cdot \xrightarrow{k_{48}} C_4H_6$	[11]	**3.48**
$C_2H_5\cdot + C_2H_3\cdot \xrightarrow{k_{49}} 1\text{-}C_4H_8$	[11]	**3.49**
$C_2H_5\cdot + C_2H_5\cdot \xrightarrow{k_{50}} n\text{-}C_4H_{10}$	[11]	**3.50**
$C_2H_5\cdot + C_2H_5\cdot \xrightarrow{k_{51}} C_2H_4 + C_2H_6$	[11]	**3.51**
$1\text{-}C_4H_7\cdot + CH_3\cdot \xrightarrow{k_{52}} cyC_5H_{10}$	[11]	**3.52**
$1\text{-}C_4H_7\cdot + C_2H_3\cdot \xrightarrow{k_{53}} C_6H_{10}$	[11]	**3.53**
$1\text{-}C_4H_7\cdot + C_2H_5\cdot \xrightarrow{k_{54}} C_6H_{12}$	[11]	**3.54**
$1\text{-}C_4H_7\cdot + C_3H_5\cdot \xrightarrow{k_{55}} C_7H_{12}$	[11]	**3.55**
$C_5H_{11}\cdot + H\cdot \xrightarrow{k_{56}} C_5H_{12}$	[11]	**3.56**

The reactions shown in Table 5 are assumed to be elementary reactions so their order corresponds to the molecularity of the pertinent species as listed as assumption 4.3 in Table 4.[11] The rate constants are assumed to follow Arrhenius behaviour in the temperature range of interest. Initial values for rate constants k_0 and activation energies E_A divided by the ideal gas constant R are shown in Table 6.

Table 6 – Ethane pyrolysis kinetic parameters

No.	A (s^{-1} or $m^3mol^{-1}s^{-1}$)	E_a/R (K)	Ref
1	4.0×10^{16}	4.40×10^4	[11]
2	8.0×10^{16}	3.72×10^4	[12]
3	1.5×10^{16}	4.13×10^4	[11]
4	9.0×10^{16}	4.30×10^4	[11]
5	8.0×10^5	2.01×10^3	[11]
6	1.0×10^8	4.88×10^3	[11]
7	1.0×10^7	6.54×10^3	[11]
8	3.8×10^8	8.30×10^3	[11]
9	1.2×10^6	7.05×10^3	[10]
10	3.0×10^6	9.56×10^3	[11]
11	4.0×10^7	6.54×10^2	[11]
12	1.0×10^7	7.55×10^2	[11]
13	1.0×10^7	1.46×10^3	[11]
14	3.5×10^7	7.55×10^2	[10]
15	4.0×10^7	6.54×10^2	[14]
16	2.0×10^5	3.98×10^3	[11]
17	5.0×10^4	5.03×10^2	[11]
18	3.98×10^5	2.51×10^3	[46]
19	1.26×10^5	2.51×10^3	[46]
20	1.5×10^4	3.82×10^3	[11]
21	1.3×10^4	3.77×10^3	[11]
22	2.0×10^4	3.72×10^3	[11]
23	3.16×10^{12}	1.73×10^4	[46]
24	3.16×10^{12}	1.73×10^4	[46]
25	2.0×10^9	1.59×10^4	[11]
26	3.2×10^{13}	2.01×10^4	[11]
27	3.0×10^{10}	1.82×10^4	[11]
28	8.9×10^{12}	2.97×10^4	[10]
29	4.0×10^{13}	1.64×10^4	[11]
30	2.0×10^{13}	1.93×10^4	[11]
31	1.2×10^{14}	2.48×10^4	[11]
32	1.0×10^{11}	1.86×10^4	[11]
33	1.6×10^{12}	1.41×10^4	[11]
34	1.0×10^{13}	1.84×10^4	[11]
35	1.0×10^{14}	1.71×10^4	[46]
36	5.0×10^{13}	1.84×10^4	[11]
37	3.2×10^{13}	1.59×10^4	[11]
38	4.0×10^{12}	1.44×10^4	[11]
39	1.0×10^7	0	[11]
40	4.0×10^7	0	[15]
41	2.0×10^7	0	[11]

42	1.0×10^7	0	[11]
43	2.0×10^7	0	[11]
44	1.0×10^7	0	[11]
45	1.3×10^7	0	[11]
46	3.2×10^6	0	[11]
47	3.2×10^6	0	[11]
48	1.3×10^7	0	[11]
49	1.3×10^7	0	[11]
50	4.0×10^5	0	[11]
51	5.0×10^4	0	[11]
52	3.2×10^6	0	[11]
53	1.3×10^7	0	[11]
54	3.2×10^6	0	[11]
55	1.3×10^7	0	[11]
56	1.0×10^7	0	[11]

3.2.2 Pressure drop

The build-up of a coke layer on the inner surface of the tube walls increases the pressure drop along the length of the tubes over time. To maintain the required outlet pressure for the downstream process, the inlet pressure of the reactor must be increased to account for the increased pressure drop. The resulting increase in average pressure decreases the ethylene selectivity and therefore the product yield.[2] As a result, the inlet pressure is one of the factors that is used to determine when it is necessary to run a decoke cycle and remove the built-up coke layer.

To create a model that accurately predicts product yield and can be used to predict run length before length before decoke, it is important to have an expression to model pressure drop that accounts for accounts for the build-up of the coke layer. Sundaram and Froment[21] proposed the momentum momentum balance shown as the ODE 7.1 in

Table 7.

Table 7 – Model equations

Equation	No.
$$\frac{dP}{dx} = \frac{\frac{d}{dx}\left(\frac{1}{MW_g}\right) + \frac{1}{MW_g}\left(\frac{1}{T_g}\frac{dT_g}{dx} + Fr\right)}{\frac{1}{MW_g P} - \frac{P}{\alpha R T_g}\left(\frac{\pi D_{ic}}{4\dot{m}_g}\right)^2}$$	7.1
$$MW_g = \sum x_{i,g} MW_i$$	7.2
$$Fr = \frac{0.092 {Re_g}^{-0.2}}{D_{ic}}$$	7.3
$$Fr = \frac{0.092 {Re_g}^{-0.2}}{D_{ic}} + \frac{0.0714 + 0.266\frac{D_{ic}}{R_{bend}}}{\pi R_{bend}}$$	7.4
$$Re_g = \frac{4\dot{m}_g}{\pi D_{ic} \mu_g}$$	7.5
$$D_{ic} = D_i + 2s_t$$	7.6
$$\mu_g = \frac{\sum_i x_{i,g} \mu_i(T_g) {MW_i}^{0.5}}{\sum_i x_{i,g} {MW_i}^{0.5}}$$	7.7
$$\mu_i(T) = A_{\mu_i} T^2 + B_{\mu_i} T + C_{\mu_i}$$	7.8
$$C_{p,g} = \frac{\sum x_{i,g} C_{p,i}(T_g)\, MW_i}{MW_g}$$	7.9
$$C_{p,i}(T) = A_{C_{p,i}} T^3 + B_{C_{p,i}} T^2 + C_{C_{p,i}} T + D_{C_{p,i}}$$	7.10
$$r_{crack} = -k_1[\mathrm{C_2H_6}] - k_6[\mathrm{C_2H_6}][\mathrm{H}] - k_8[\mathrm{C_2H_6}][\mathrm{CH_3}]$$	7.11
$$h_{conv,g} = 0.0279 \frac{{\dot{m}_g}^{0.8} {\lambda_g}^{0.6} {C_{p,g}}^{0.4}}{{D_{ic}}^{1.8} {\mu_g}^{0.4}}$$	7.12
$$\lambda_g = \frac{\sum_i x_{i,g} \lambda_i(T_g)}{\sum_m x_m \phi_{im}(T_g)}$$	7.13
$$\phi_{im}(T) = \frac{\left(1 + \left(\frac{\mu_i(T)}{\mu_m(T)}\right)^{0.5} \left(\frac{MW_m}{MW_i}\right)^{0.25}\right)^2}{\sqrt{8}\left(1 + \frac{MW_i}{MW_m}\right)^{0.5}}$$	7.14
$$\lambda_i(T) = A_{\lambda_i} T^2 + B_{\lambda_i} T + C_{\lambda_i}$$	7.15

$$h_{conv+cond} = \left[D_o \left(\frac{1}{h_{conv,g} D_{ic}} + \frac{\lambda_c \ln\left(\frac{D_o}{D_i}\right) + \lambda_t \ln\left(\frac{D_i}{D_{ic}}\right)}{2\lambda_c \lambda_t} \right) \right]^{-1}$$	**7.16**
$$\frac{dT_g}{dx} = \frac{1}{\dot{m}_g C_{p,g}} \left(h_{conv+cond} D_o \pi \left(T_{to} - T_g \right) - r_{crack} \Delta H_{crack} \frac{\pi}{4} {D_{ic}}^2 \right)$$	**7.17**
$$\frac{dq^+}{dz} = \beta \sigma {T_f}^4 + \frac{\varepsilon_t A_t \sigma}{2} \frac{\sum_{i=1}^{n_p} {T_{to,i}}^4}{n_p} - \left(\beta + \frac{\varepsilon_r A_r}{4} + \frac{\varepsilon_t A_t}{2} \right) q^+ + \frac{\varepsilon_r A_r}{4} q^-$$	**7.18**
$$\frac{dq^-}{dz} = -\left(\beta \sigma {T_f}^4 + \frac{\varepsilon_t A_t \sigma}{2} \frac{\sum_{i=1}^{n_p} {T_{to,i}}^4}{n_p} + \frac{\varepsilon_r A_r}{4} q^+ - \left(\beta + \frac{\varepsilon_r A_r}{4} + \frac{\varepsilon_t A_t}{2} \right) q^- \right)$$	**7.19**
$$\frac{dT_f}{dz} = \frac{1}{\dot{m}_f C_{p,f}} \beta A_c \left(q^+ + q^- - 2\sigma {T_f}^4 \right)$$	**7.20**
$$\alpha_{air} = \frac{x_{H_2,fuel} \left(0.5 \frac{x_{N_2,air}}{x_{O_2,air}} + 1 \right) + x_{CH_4,fuel} \left(2 \frac{x_{N_2,air}}{x_{O_2,air}} + 3 \right)}{\left(0.5 x_{H_2,fuel} + 2 x_{CH_4,fuel} \right) \left(\frac{1}{x_{O_2,f}} - \frac{x_{N_2,air}}{x_{O_2,air}} - 1 \right)}$$	**7.21**
$$\dot{m}_f = \dot{n}_f MW_f$$	**7.22**
$$x_{CH_4,fuel} = 1 - x_{H_2,fuel}$$	**7.23**
$$MW_{fuel} = x_{CH_4,fuel} MW_{CH_4} + x_{H_2,fuel} MW_{H_2}$$	**7.24**
$$\dot{n}_{fuel} = \frac{\dot{m}_{fuel}}{MW_{fuel}}$$	**7.25**
$$\dot{n}_{N_2,f} = \frac{x_{N_2,air}}{x_{O_2,air}} \dot{n}_{fuel} (1 + \alpha_{air}) \left(2 x_{CH_4,fuel} + 0.5 x_{H_2,fuel} \right)$$	**7.26**
$$\dot{n}_{O_2,f} = \dot{n}_{fuel} \left[\alpha_{air} \left(2 x_{CH_4,fuel} + 0.5 x_{H_2,fuel} \right) \right]$$	**7.27**
$$\dot{n}_{CO_2,f} = \dot{n}_{fuel} \left(x_{CH_4,fuel} \right)$$	**7.28**
$$\dot{n}_{H_2O,f} = \dot{n}_{fuel} \left(2 x_{CH_4,fuel} + x_{H_2,fuel} \right)$$	**7.29**
$$\dot{n}_f = \sum \dot{n}_{i,f}$$ for i=N_2, O_2,CO_2,H_2O	**7.30**
$$x_{i,f} = \frac{\dot{n}_{i,f}}{\dot{n}_f}$$ for i=N_2, O_2,CO_2,H_2O	**7.31**
$$MW_f = \sum x_{i,f} MW_i$$ for i=N_2, O_2,CO_2,H_2O	**7.32**
$$C_{p.f} = \sum x_{i,f} C_{p,i}$$ for i=N_2, O_2, CO_2, H_2O	**7.33**

$0 = \frac{\varepsilon_t}{2}\left(q^+ + q^- - 2\sigma {T_{to}}^4\right) - h_{conv+cond}\left(T_{to} - T_g\right)$	**7.34**

Equation 7.1 calculates how the absolute pressure P changes with position based on the average molecular weight of the process gas MW_g, the temperature of the process gas T_g, a pressure drop constant α, the ideal gas constant R, the internal diameter at the surface of the coke layer D_{ic}, the mass flow rate of the process gas $\dot{m}_g$, and a friction factor *Fr*. The average molecular weight of the process gas MW_g is calculated by equation 7.2 in

Table 7.

The friction factor depends on the configuration of the tubes and can be calculated by equation 7.3 for the straight sections of tubes and 7.4 for the 180° bends. The Reynolds number Re_g required for the friction factor calculation depends on the internal diameter D_{ic}, and the process-gas density ρ_g, dynamic viscosity μ_g and velocity $\frac{4\dot{m}_g}{\rho_g \pi {D_{ic}}^2}$

$$Re_g = \frac{4\dot{m}_g}{\rho_g \pi {D_{ic}}^2} \frac{\rho_g D_{ic}}{\mu_g} \quad \textbf{21}$$

which reduces to equation 7.5 in

Table 7. The internal diameter D_{ic} and dynamic viscosity μ_g are calculated in equations 7.6 to 7.8 in

Table 7 and the viscosity polynomial coefficients can be found in Table 19 in Appendix B.

3.2.3 Process-side energy balance

The endothermic pyrolysis reactions occur more rapidly when more heat is transferred through the tube walls to the process gas. The formation of coke is also highly temperature dependent and therefore accurate prediction of reaction products and coke formation relies heavily on appropriate governing energy balances. To derive a steady-state energy balance for the tube contents, consider a small section of the tube with a length Δx as shown in Figure 6:

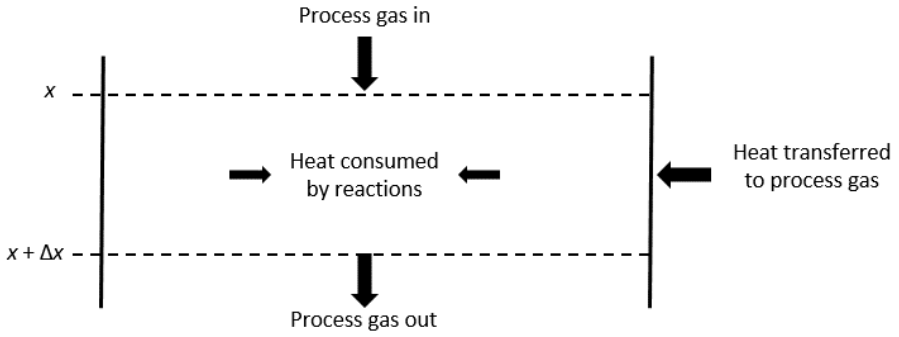

Figure 6 – Process gas energy balance over a small length of tube Δx

$$\text{Accumulation of energy} = \text{enthalpy of mass flow in at top} - \text{enthalpy of mass flow out at bottom} - \text{rate of heat consumption by reactions} + \text{rate of heat transfer to process gas} \quad \textbf{22}$$

The enthalpy of the gas flowing into the section is equal to $\dot{m}_g C_{p,g}(T_g - T_{ref})$ where $\dot{m}_g$ is the mass flow rate of the reacting gases and $C_{p,g}$ is the heat capacity, which is dependent on the reactor gas temperature T_g and calculated by equations 7.9 and 7.10. The first term in equation 22 is at position *x* so that the term is $\dot{m}_g C_{p,g}(T_{g,x} - T_{ref})$ and the second term is at position $x + \Delta x$ so that the term is $\dot{m}_g C_{p,g}(T_{g,x+\Delta x} - T_{ref})$. The difference in the two is $\dot{m}_g C_{p,g}(T_{g,x} - T_{g,x+\Delta x})$.

The heat consumed by the reactions depends on the enthalpy of the reactions ΔH_{rxn} (in kJ mol^{-1}), the rate at which the reactions take place, r_{crack} (in mol s^{-1}m^{-3}), and the reaction volume $\frac{\pi}{4} {D_{ic}}^2 \Delta x$ (in m^3).

For rigorous calculations, the heat of reaction should be determined by considering all of the reactions that occur. However, information about the heat of formation of many of the radical species is not readily available and therefore a rigorous approach is not practical. It is instead assumed that the heat of the reaction calculated by only considering the consumption of ethane is equivalent to the heat of all reactions as listed as assumption 4.6 in Table 4. This is thought to be a reasonable approximation since the feed is composed of ethane and steam, and the steam is assumed to be an inert diluent as stated in assumption 4.8. The heat of reaction r_{crack} is then the sum of the sum of the rates of reactions 1, 6 and 8 where ethane is being consumed, which is shown as equation as equation 7.11 in

Table 7. The third term in equation 22, which accounts for rate of heat consumption by the reactions is:

$$r_{crack}\Delta H_{crack}\frac{\pi}{4}{D_{ic}}^{2}\Delta x \quad \textbf{23}$$

Heat is transferred to the reactor contents from the surface of the coke layer via convection:[48]

$$h_{conv,g}\pi D_{ic}\Delta x\left(T_c - T_g\right) \quad \textbf{24}$$

where T_c is the temperature of the inner surface of the coke layer, as shown in Figure 5 and $h_{conv,g}$ is and $h_{conv,g}$ is the convective heat-transfer coefficient between the coke surface and the reactor reactor contents. The convective heat-transfer coefficient $h_{conv,g}$ is calculated by the empirical empirical equation 7.12 in

Table 7[49,50] and depends on the internal diameter at the coke surface D_{ic}, process gas mass flow rate $\dot{m}_g$, heat capacity C_{pg}, dynamic viscosity μ_g, and conductivity λ_g. Process gas conductivity is calculated by equations 7.13 to 7.15 and the conductivity polynomial coefficients are provided in Appendix B.

At steady state there is no accumulation of heat in the coke layer or the tube walls. The rate of heat transfer from the surface of the coke layer to the process gas is the same as the rate of heat transfer through the coke layer via conduction:[48]

$$\frac{\lambda_c \pi D_{lm} \Delta x (T_{ti} - T_c)}{\frac{D_i - D_{ic}}{2}} \quad \textbf{25}$$

where λ_c is the thermal conductivity of the coke (in kW·m^{-1}K^{-1}), T_{ti} is the inner tube wall temperature, $\pi D_{lm} \Delta x$ is the "average" area for heat transfer, where D_{lm} is the log mean diameter of the coke layer:

$$D_{lm} = \frac{D_i - D_{ic}}{\ln\left(\frac{D_i}{D_{ic}}\right)} \quad \textbf{26}$$

and $\frac{D_i - D_{ic}}{2}$ is the thickness of the coke layer. Expression 25 simplifies to:

$$\frac{2\lambda_c \pi \Delta x (T_{ti} - T_c)}{\ln\left(\frac{D_i}{D_{ic}}\right)} \quad \textbf{27}$$

The rate of heat transfer via conduction through the tube walls takes a similar form as equation 27:

$$\frac{2\lambda_t \pi \Delta x (T_{to} - T_{ti})}{\ln\left(\frac{D_o}{D_i}\right)} \quad \textbf{28}$$

where λ_t is the thermal conductivity of the tube walls and T_{to} is the outer tube wall temperature. Since there is no accumulation of heat in the tube walls or coke layer at steady state, the rates of heat transfer in equations 24, 27, and 28 are equal:

$$\dot{Q}_{transfer} = h_{conv,g}\pi D_{ic}\Delta x\left(T_c - T_g\right) = \frac{2\lambda_c\pi\Delta x(T_{ti} - T_c)}{\ln\left(\frac{D_i}{D_{ic}}\right)} = \frac{2\lambda_t\pi\Delta x(T_{to} - T_{ti})}{\ln\left(\frac{D_o}{D_i}\right)} \quad \textbf{29}$$

29.1 **29.2** **29.3**

The inner tube wall temperature T_{ti} is not of interest so it can be eliminated by combining 29.2 and 29.3 such that:

$$\dot{Q}_{transfer} = \frac{\pi\Delta x(T_{to} - T_c)}{\left(\frac{\lambda_c \ln\left(\frac{D_o}{D_i}\right) + \lambda_t \ln\left(\frac{D_i}{D_{ic}}\right)}{2\lambda_c\lambda_t}\right)} \quad \textbf{30}$$

and therefore:

$$\dot{Q}_{transfer} = h_{conv,g}\pi D_{ic}\Delta x\left(T_c - T_g\right) = \frac{\pi\Delta x(T_{to} - T_c)}{\left(\frac{\lambda_c \ln\left(\frac{D_o}{D_i}\right) + \lambda_t \ln\left(\frac{D_i}{D_{ic}}\right)}{2\lambda_c\lambda_t}\right)} \quad \textbf{31}$$

31.1 **31.2**

By combining equations 31.1 and 31.2, the coke temperature T_c, which is also not of interest, can be eliminated. This results in a single equation describing the rate of heat transfer from the outer tube wall to the process gas:

$$\dot{Q}_{transfer} = \frac{\pi\Delta x\left(T_{to} - T_g\right)}{\left(\frac{1}{h_{conv,g}D_{ic}} + \frac{\lambda_c \ln\left(\frac{D_o}{D_i}\right) + \lambda_t \ln\left(\frac{D_i}{D_{ic}}\right)}{2\lambda_c\lambda_t}\right)} \quad \textbf{32}$$

Equation 32 can be written in a more typical form of heat transfer equation based on the outer tube surface area and a heat transfer coefficient so that:

$$\dot{Q}_{transfer} = h_{conv+cond} D_o \pi \Delta x \left(T_{to} - T_g\right) \quad \textbf{33}$$

where $h_{conv+cond}$ is calculated by equation 7.16.

Equation 22 can then be written as:

$$\frac{\left(T_{g,x+\Delta x} - T_{g,x}\right)}{\Delta x} = \frac{1}{\dot{m}_g C_{p,g}} \left(h_{conv+cond} D_o \pi \Delta x \left(T_{to} - T_g\right) - r_{crack} \Delta H_{crack} \frac{\pi}{4} {D_{ic}}^2 \right) \quad \textbf{34}$$

When Δx approaches zero equation 34 becomes the ODE shown in

Table 7 as equation 7.17.

3.3 Furnace-side model development

The energy balance on the furnace side in the radiant section is complex due to the importance of radiant heat transfer and the difficulties in modeling this type of heat transfer. Radiation beams interact with the furnace gas, refractory-wall and tube-wall surfaces in different directions so that heat can be transferred between adjacent volume elements of gas via radiation. The Roesler flux method with a grey gas assumption is applied to simplify the radiative field into two radiant fluxes, one in the upward direction and one in the downward direction.[40] The derivation of the radiant flux ODEs 7.18 and 7.19 can be found in Appendix A.

A total energy balance on the furnace gas can be performed on a small section of height Δz:

Accumulation	=	enthalpy in with furnace gas flow at bottom	-	enthalpy out with furnace gas flow at top	+	upward radiation absorbed by furnace gas	**35**
	+	downward radiation absorbed by furnace gas	-	radiation emitted by furnace gas			

The flux terms can be converted to energy flows by multiplying by the cross sectional area A_c so that the equation 35 is:

$$0 = \dot{m}_f C_{p,f}(T_{f,z} - T_{ref}) - \dot{m}_f C_{p,f}(T_{f,z+\Delta z} - T_{ref}) + \beta A_c q^{+} \Delta z + \beta A_c q^{-} \Delta z - 2\beta A_c \sigma {T_f}^4 \Delta z \quad \textbf{36}$$

where $\dot{m}_f$ is the mass flow rate of furnace gas, $C_{p,f}$ is the heat capacity of the furnace gas (which (which depends on the temperature of the furnace gas T_f), β is the fraction of radiation that is

that is absorbed by the furnace gas per unit length, A_c is the cross sectional area of the furnace and q^+ and q^- are the upward and downward radiant fluxes, respectively. When the small section of height Δz approaches zero, equation 36 becomes equation 7.20 in

Table 7.

The mass flow rate of furnace gas $\dot{m}_f$ depends on the amount of fuel that is burned and how much excess air is used for combustion. The fuel that is burned at the burners in the radiant section is a mixture of methane (CH_4) and hydrogen (H_2). The two combustion reactions:

$$CH_4 + 2O_2 \rightarrow CO_2 + 2H_2O \quad \textbf{37}$$

$$H_2 + \tfrac{1}{2}O_2 \rightarrow H_2O \quad \textbf{38}$$

are assumed to go to completion due to addition of excess air as stated in assumption 4.13. The mole 4.13. The mole fraction of oxygen in the furnace gas exiting the stack $x_{O_2,f}$ is measured and and controlled so that the fraction of excess air used in combustion α_{air} can be calculated in equation in equation 7.21 from stoichiometry in equations 37 and 38 and the known fuel composition. Equation 7.22 in

Table 7 calculates the total mass flow rate of furnace gas $\dot{m}_f$ in the first and second terms of equation 36 based on this fraction of excess air α_{air}, the known flow rate of fuel $\dot{m}_{fuel}$, and equations 7.23 to 7.32.

The heat capacity of the furnace gas in the first two terms on the right-hand side of equation 36 is the average heat capacity calculated in 7.33. It depends on the composition and temperature of the furnace gas. The heat capacity correlation provided in equation 7.10 is the same correlation that is used on the process-gas side and the coefficients for each species are provided in Table 17 in Appendix B.

The tube wall temperature T_{to} can be determined by performing a steady-state energy balance on the tube walls, assuming that the walls are thin enough so that there is no accumulation of heat in the tube walls. This balance can be performed (in units of $kW \cdot m^{-2}$) to link the process-side model for a single tube to the furnace-side model which considers the entire furnace volume:

0	=	Rate of upward radiation absorbed by tube walls per unit of outer tube surface area	+	Rate of downward radiation absorbed by tube per unit of outer tube surface area	-	Rate of radiation emitted by tube walls per unit of outer tube surface area	-	Rate of heat transferred to process gas per unit of outer tube surface area		**39**

$$0 = \frac{\varepsilon_t}{2} q^{+} + \frac{\varepsilon_t}{2} q^{-} - \varepsilon_t \sigma T_{to} - h_{conv+cond}\left(T_{to} - T_g\right)$$

Equation 39 can be simplified to the non-linear equation shown as equation 7.34 in

Table 7.

Chapter 4 – Model Implementation

4.1 Software selection

For the model to be readily usable by NOVA Chemicals scientists, it should be implemented using a software tool that makes the model easy to run and maintain. In addition, it should be possible to integrate the ethane cracking/coke formation model with related CFD models for the furnace side that will be developed by the company. A number of commercial software packages for simulation of thermal cracking were reviewed. The following simulation programs were identified by NOVA Chemicals as tools that are specifically designed for pyrolysis modeling or that could provide a platform for developing fundamental models for thermal cracking:

i. SPYRO® of Technip Benelux B.V., The Netherlands
ii. Olefin SIM/Lummus® of KBC Advanced Technologies, USA
iii. COILSIM1D of Laboratory of Chemical Technology, University of Gent, Belgium
iv. CRACKER of Korea Advanced Institute of Science and Technology, South Korea
v. SHAHAB of Olefin Research group of Tarbiat Modares University, Iran
vi. ASPEN Custom Modeller® (ACM) of Aspen Technology, Inc., USA
vii. PREDICI® of Computing in Technology GmbH, Germany

The following factors were considered when choosing the software that could be used to develop the proposed model:

i. Coke formation mechanisms: SPYRO® and COILSIM1D do not consider the catalytic mechanism of coke formation. Olefin SIM/Lummus® currently has no coking model.[45]
ii. Flexibility: To the best of our knowledge, the source code for SPYRO®, Olefin SIM/Lummus®, COILSIM1D and CRACKER is not "open" and changeable. Access to simulation codes to make changes that might be required by NOVA Chemicals is impossible without the developers' support.
iii. Dynamic capability: SPYRO®, Olefin SIM/Lummus®, COILSIM1D and CRACKER are all steady-state simulation tools, whereas NOVA Chemicals' interest is to extend the model to predict dynamic operation.
iv. Trade restrictions: This issue nullifies SHAHAB as a candidate modeling tool.

Based on these factors, ASPEN Custom Modeller (ACM)® and PREDICI® are the two software tools that were considered for the proposed modeling research. These programs are not pyrolysis models; they are flexible numerical solvers that can be used to model plug-flow reactors in dynamic or steady state mode, depending on how the code is written. Based on previous experience at NOVA Chemicals and Queen's University, PREDICI® was chosen over ASPEN Custom Modeller® due to its robustness (convergence), its facility in handling complex reaction schemes, and its proficiency at developing equations automatically based on the reaction scheme and other user-specified factors (i.e., plug flow or well mixed reactor). In addition, Dr. Michael

Wulkow, the developer of PREDICI®, has a well-deserved reputation for providing effective and timely support to industrial and academic users of the PREDICI® program.

4.2 Collected data

The steady-state model in this thesis is developed initially for a coke-free tube, with provisions so that it can be extended to simulate operation with coke on the tube walls. As a result, data for testing this initial steady state-model should be collected at early run times, before a significant amount of coke has formed on the tube walls. The primary indicator of coke formation is the increase in pressure drop over the length of the tube. As coke builds-up on the tube walls, the tube diameter decreases, the process gas velocity increases and the pressure drop increases. Regardless of coke formation, pressure drop will also increase with an increase in the mass flow rate of the process gas, in a roughly linear fashion. Therefore, an adjusted pressure drop calculation:

$$\Delta P_{adj} = \frac{|P_{out} - P_{in}|}{\dot{m}_g} \quad \textbf{40}$$

is used to determine whether a significant amount of coke has been formed on the inside of the tube walls, where ΔP_{adj} is the adjusted pressure drop, P_{out} is the outlet pressure, P_{in} is the inlet pressure and $\dot{m}_g$ is the mass flow rate of the process gas. If the adjusted pressure drop has increased by less than 5% since the beginning of the run, it is assumed that there is no significant coke-formation and the tube can be treated as a coke-free tube for the purposes of data collection. It is also assumed that there is no spalling of coke particles from any upstream section, as listed in assumption 4.14 in Table 4.

Typical operating conditions were collected for a Stone and Webster Induced Draft Furnace with the geometry shown in Table 8.

Table 8 – Geometry and typical operating conditions for a Stone and Webster Induced Draft Furnace

Reactor Geometry			
Symbol	**Value**		**Units**
A_c	16.35		m^2
A_t	0.541		m^{-1}
A_r	1.47		m^{-1}
D_i	$0 \leq x \leq 25.2$	0.0754126	m
	$25.2 < x \leq 31.4$	0.0817626	
	$31.4 < x \leq 56.3$	0.0881126	
s_t	0.0064		m
n_p	2		dimensionless
Typical operating conditions			
Symbol	**Value**		**Units**
$\dot{m}_{fuel}$	0.8303		$kg \cdot s^{-1}$
$\dot{m}_g$	0.5094		$kg \cdot s^{-1}$
T_{g0}	936		K
$w_{C_2H_6,g}$	0.772		dimensionless
$w_{H_2O,g}$	0.228		dimensionless
$x_{H_2,fuel}$	0.56		dimensionless
$x_{O_2,f}$	0.0239		dimensionless
$x_{Q_{lost}}$	0.0298		dimensionless

These conditions are used as a base-case for model development and implementation and were determined by considering the beginning of 11 runs, between July 2010 and July 2013. All data were collected from the beginning of the run until the adjusted pressure drop had increased by 5%, indicating significant coke formation. These values were averaged for all runs to determine typical operating conditions for a coke-free tube.

The operating variables that were collected from the plant and used to determine model inputs are:

- inlet process gas pressure (kPa_g)
- inlet process gas temperature (°C)

- inlet ethane mass flow rate (kg/h)
- inlet dilution steam mass flow rate (kg/h)
- ambient air temperature (°C)
- fuel temperature (°C)
- fuel mass flow rate (kg/h)
- volume fraction of hydrogen in fuel (mol%)
- volume fraction of oxygen exiting stack (mol%)

The averages of these variables over the beginning of 11 runs are used to calculate the operating variables that can be input in the model directly, shown in Table 8. These 11 runs can also be used independently as different run conditions for model verification or parameter estimation in future work.

4.3 Initial and boundary conditions

The tubular reactor model developed in Chapter 3 includes 29 ODE mass balances on 29 gas-phase species and 5 additional ODEs (one momentum balance, two energy balances and two radiation balances). As a result, 34 initial or boundary conditions are required to solve the model equations. On the process-gas side, initial conditions ($x = 0$) for all of the species concentrations and the temperature and pressure are known from available data.

On the furnace side the situation is more complicated. The current model considers a floor-fired burner configuration as depicted in Figure 3a). Therefore, is assumed that the combustion gas enters the bottom of the furnace ($z = 0$) at the combustion temperature T_{comb} (assumption 4.15), which provides a boundary condition for the

furnace gas energy balance. This combustion temperature is determined by performing a hypothetical energy balance on the fuel that is combusted with excess air:

$$0 = \begin{array}{c}\text{Rate of heat release by cooling of fuel to reference temperature}\end{array} + \begin{array}{c}\text{Rate of heat release by cooling air to reference temperature}\end{array} + \begin{array}{c}\text{Rate of heat release by the combustion of fuel}\end{array} + \begin{array}{c}\text{Rate of heat consumed by heating furnace gas to combustion temperature}\end{array} + \begin{array}{c}\text{Rate of heat loss to environment}\end{array} \quad \textbf{41}$$

$$0 = \dot{m}_{fuel}\int_{T_{fuel}}^{T_{ref}} C_{p,fuel}dT + \dot{m}_{air}\int_{T_{air}}^{T_{ref}} C_{p,air}dT + \dot{n}_{fuel}\Delta H_{c,fuel} + \dot{m}_f\int_{T_{ref}}^{T_{comb}} C_{p,f}dT + \dot{Q}_{lost}$$

where T_{fuel} is the initial fuel temperature, T_{air} is the initial temperature of the combustion air, $C_{p,fuel}$ is the heat capacity of the fuel calculated by equation 9.1 in Table 9, $C_{p,air}$ is the heat capacity of the air calculated by equation 9.2, $\dot{m}_{air}$ is the flow rate of combustion air calculated by equation 9.3, $\dot{n}_{fuel}$ is the molar flow rate of fuel calculated by equation 9.4 and $\Delta H_{c,fuel}$ is the enthalpy of combustion of fuel calculated by equation 9.6.

Table 9 – Additional model equations required for the calculation of boundary conditions

$C_{p.fuel} = x_{H_2,fuel}C_{p,H_2} + x_{CH_4,fuel}C_{p,CH_4}$	**9.1**
$C_{p.air} = x_{o_2,air}C_{p,O_2} + x_{N_2,air}C_{p,N_2}$	**9.2**
$\dot{m}_{air} = \dot{m}_f - \dot{m}_{fuel}$	**9.3**
$\dot{n}_{fuel} = \frac{\dot{m}_{fuel}}{MW_{fuel}}$	**9.4**
$MW_{fuel} = x_{CH_4,fuel}MW_{CH_4} + x_{H_2,fuel}MW_{H_2}$	**9.5**
$\Delta H_{c,fuel} = x_{H_2,fuel}\Delta H_{c,H_2} + x_{CH_4,fuel}\Delta H_{c,CH_4}$	**9.6**
$0 = \dot{m}_{fuel}\int_{T_{fuel}}^{T_{ref}} C_{p,fuel}\,dT + \dot{m}_{air}\int_{T_{air}}^{T_{ref}} C_{p,air}dT + \left(1 - x_{Q_{lost}}\right)\dot{n}_{fuel}\Delta H_{c,fuel} + \dot{m}_f\int_{T_{ref}}^{T_{comb}} C_{p,f}\,dT$	**9.7**

Equation 41 includes a heat loss term. It is assumed that the furnace walls are well insulated so the heat is lost from the burners at the bottom of the furnace before the hot combustion gas enters the furnace as stated in assumption 4.16 in Table 4. The rate of heat loss $\dot{Q}_{lost}$ is unknown, but if it is assumed that the rate of heat lost at each of the burners is the same (assumption 4.17), then the average rate of heat loss can be determined using plant operating data and an overall steady-state energy balance on the radiant section and the burners:

0 =	Enthalpy of furnace gas in	-	Enthalpy of furnace gas out	+	Enthalpy of process gas in	
-	Enthalpy of process gas out	-	Rate of heat consumption by reactions	-	Rate of heat loss to the environment	

42

$$0 = \dot{m}_f \int_{T_{ref}}^{T_{f,z=0}} C_{p,f}\,dT - \dot{m}_f \int_{T_{ref}}^{T_{f,z=Z}} C_{p,f}\,dT + n_t \dot{m}_g \int_{T_{ref}}^{T_{g,x=0}} C_{p,g}\,dT - n_t \dot{m}_g \int_{T_{ref}}^{T_{g,x=X}} C_{p,g}\,dT - \dot{n}_{C_2H_6,cons} \Delta H_{crack} - \dot{Q}_{lost}$$

where the mass flow rate of the process gas to a single tube $\dot{m}_g$ is multiplied by the number of tubes n_t to account for the total flow of process gas to the radiant section, and $\dot{n}_{C_2H_6,cons}$ is the number of moles of ethane consumed in the radiant section per second, equal to:

$$\dot{n}_{C_2H_6,cons} = \%\text{conversion}\left(\frac{w_{C_2H_6,g} n_t \dot{m}_g}{MW_{C_2H_6}}\right) \quad \textbf{43}$$

The fraction of the heat provided by combustion that is lost to the environment can be expressed as:

$$x_{Q,lost} = \frac{\dot{m}_f \int_{T_{f,z=Z}}^{T_{f,z=0}} C_{p,f} dT + n_t \dot{m}_g \int_{T_{ref}}^{T_{g,x=X}} C_{p,g} dT - \dot{n}_{C_2H_6,cons} \Delta H_{crack}}{\dot{n}_{fuel} \Delta H_{c,fuel}} \quad (44)$$

so that the combustion temperature T_{comb} (at the bottom of the furnace) can be calculated by equation 9.7 in Table 10.

Initial and boundary conditions for the radiant fluxes $q^+$and q^- are unknown. However, as stated in assumption 4.18, it is assumed that the top of the furnace and the bottom of the furnace are covered by a refractory wall that is radiatively adiabatic. As a result, the upward radiation entering the refractory wall at the top of the furnace must equal the downward radiation leaving the refractory wall at the top of the furnace $q^+{}_{z=Z} = q^-{}_{z=Z}$. Similarly, the downward radiation entering the refractory wall at the bottom of the furnace must equal the upward radiation leaving the refractory wall at the bottom of the furnace $q^+{}_{z=0} = q^-{}_{z=0}$ which gives two conditions that must be satisfied when solving the two radiation-balance ODEs.

4.4 Implementation of ethane pyrolysis kinetics in PREDICI®

The reaction kinetics shown in Table 5 can be implemented in PREDICI® using the built-in reaction modules. The general kinetic step reaction module can be used for all of the reactions. The module accepts inputs of stoichiometric coefficients for reactants and products along with the reaction order for the reactants. In this model, all reactions are considered to be elementary, so the reaction order field is left blank and PREDICI® defaults to an order of one. The general kinetic step reaction module also accepts inputs for forward and backward rate constants. When a rate constant is declared in the reaction module, a new "coefficient" is added in PREDICI®. This new coefficient can be given a

numerical value or, for the case of a rate constant that follows the Arrhenius law, a pre-exponential factor and activation energy divided by the ideal gas constant (as provided in Table 6) can be indicated and PREDICI® will calculate rate constant value at the reaction temperature.

When a new component is entered in the reaction module it is added as an "elemental species" for the particular reactor in PREDICI®. As a default, the new "elemental species" will have a molecular weight of zero and no associated properties. The molecular weight and heat capacity polynomial coefficients for each new "elemental species" must be entered manually when a new species is added. The PREDICI® heat capacity is shown as equation 7.10 and the coefficients for each of the species are provided Appendix B. The heat capacity polynomial coefficients are not known for some of the radical species and are therefore omitted. However, the concentration of radical species in the reactor is low and therefore it is assumed that the effect of neglecting the heat capacity information for these species will be negligible in the calculation of the average process gas heat capacity (assumption 4.19).

As stated in assumption 4.20, it is assumed that the process gas behaves as an ideal gas, so the density of each species can be calculated from the ideal gas law. This option can be indicated for each "elemental species" in PREDICI® in the Elemental Species dialog box. This information, along with the reaction kinetic information, molecular weights, heat capacities, temperature pressure and reactor volume are used by PREDICI® in the automatic calculation of process gas density ρ_g, molecular weight MW_g and heat capacity $C_{p,g}$.

A recipe is a convenient way to specify the feed streams in PREDICI®. There are two types of recipe modules: recipe and tank recipe.[51] The two modules are similar except that the tank recipe allows for reactants to collect in tanks (not relevant to this application), and for the temperature and pressure to be specified outside of the "workshop" where information is entered in PREDICI®. The standard recipe module gathers the temperature and pressure from the reactor settings, whereas the tank recipe allows for the temperature and pressure to be input directly into the recipe. The tank recipe option was chosen for this model so that the initial temperature, pressure, mass flow and mass fraction of components can be input together. Their initial values are shown in Table 8.

4.5 Implementation of the process-side energy balance in PREDICI®

PREDICI® has a built-in energy-balance function for tubular reactors that takes inputs for: heat capacities of the reactor contents and feed, temperature of the feed, the jacket temperature external to the tube, the overall heat-transfer coefficient and area, and the heats of reaction in the form of constant values or functions.[51] The current radiative heat-transfer problem is too complicated to use the built-in energy-balance function and, as a result, the ODEs that were presented in section 3.3 are implemented directly in PREDICI® using the ODE module.

To use the ODE module, the state variables must be defined in the model library, along with their initial values. The state variables can then be called into the ODE function as "variants". Each state variable is defined in the model library as an "equation" variable which allows for the specification of an initial value. An "equation" variable requires an

interpreter function file, but since the value is calculated in the ODE module, a dummy function is used in its place as shown in Figure 7.

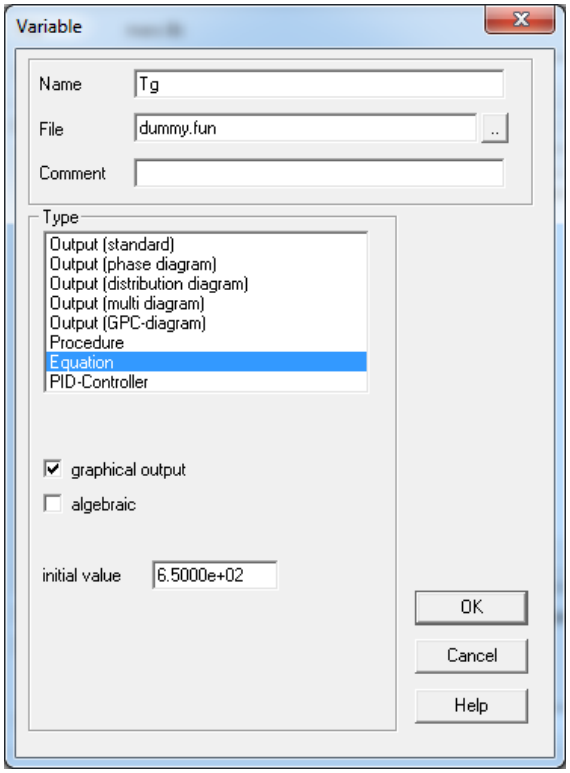

Figure 7 – Variable dialog box in PREDICI®

PREDICI® is primarily designed to model continuous stirred tank reactors (CSTR) and batch reactors. It handles tubular reactors by exploiting the analogy between time in a batch reactor, and position in a tubular reactor. Unfortunately, when built-in modules are used in PREDICI® (such as the kinetic module used to describe the reaction steps) the ODEs created in the background by PREDICI® are created with respect to time rather than position, as can be seen in the .bak file that is automatically created in PREDICI®. The .bak file compiles all of the modules into a single function file, listing all of the PREDICI®-generated ODEs. For example, methane is generated in two reactions:

reactions 3.7 and 3.8 in Table 5. Therefore, the rate of change in the methane concentration as the process gas flows along the tube (in $mol \cdot m^{-3} m^{-1}$) is:

$$\frac{d[CH_4]}{dx} = \frac{dt}{dx}(k_7[C_2H_4][CH_3] + k_8[C_2H_6][CH_3]) \quad \textbf{45}$$

where dt/dx is the reciprocal of the velocity. In the .bak file created automatically by PREDICI® the rate of change of methane concentration (that would have occurred in the corresponding batch reactor) appears:

$$\frac{d[CH_4]}{dt} = k_7[C_2H_4][CH_3] + k_8[C_2H_6][CH_3] \quad \textbf{46}$$

which has the units of $mol \cdot m^{-3} s^{-1}$. Therefore, all of the user-supplied ODEs that are entered directly in PREDICI® need to be written with respect to changes with time to match the PREDICI®-generated equations. Equation 7.17 for

Table 7:

$$\frac{dT_g}{dx} = \frac{1}{\dot{m}_g C_{p,g}} \left(h_{conv+cond} D_o \pi \left(T_{to} - T_g \right) - r_{crack} \Delta H_{crack} \frac{\pi}{4} {D_{ic}}^2 \right) \quad \textbf{7.17}$$

needs to be transformed from a change in temperature with respect to position, to a change in temperature with respect to time. This transformation is accomplished by multiplying equation 7.17 by the local process gas velocity in a coke-free tube:

$$\frac{dx}{dt} = \frac{\dot{m}_g}{\rho_g \frac{\pi}{4} {D_i}^2} \quad \textbf{47}$$

to give:

$$\frac{dT_g}{dt} = \frac{1}{\rho_g \frac{\pi}{4} {D_i}^2 C_{p,g}} \left(h_{conv+cond} D_o \pi \left(T_{to} - T_g \right) - r_{crack} \Delta H_{crack} \frac{\pi}{4} {D_{ic}}^2 \right) \quad \textbf{48}$$

Note that it is appropriate to use the coke-free internal tube diameter D_i instead of the internal diameter at the coke surface layer D_{ic} in the velocity expression, even when coke is present. The actual velocity inside the tube changes as a result of coke build-up, but when PREDICI® creates material balance equations like equation 46, it does not recognize this change in diameter due to coking. PREDICI®'s automatic transformations between position and time only consider the fixed cross-sectional area of a coke-free tube $\frac{\pi}{4} {D_i}^2$. Changes in the actual velocity due to coke formation along the tube need to be subsequently accounted for using a "library" function in PREDICI®.

A similar consideration must be made in the volume calculation in the second term on the right hand side of equation 7.17. The term r_{crack} is the rate of ethane cracking in $mol \cdot m^{-3} s^{-1}$ calculated by equation 7.11 in

Table 7:

$$r_{crack} = -k_1[C_2H_6] - k_6[C_2H_6][H] - k_8[C_2H_6][CH_3] \quad \textbf{7.11}$$

The molar concentrations in equation 7.11 are determined by PREDICI® from the specified reaction kinetics and the reactor feed composition. The feed composition is specified in the recipe in PREDICI® using mass flow rates of each species. PREDICI® converts these mass flow rates to molar concentrations based on molecular weight, temperature, pressure and volume using the ideal gas law. The volume that PREDICI® uses for these calculations is based on the fixed internal tube diameter. Therefore, when the molar concentrations are converted to the number of moles by multiplying by volume, as in equation 7.17, the internal tube diameter D_i should be used for the calculations. Equation 7.17 becomes equation 10.2 in Table 10.

Table 10 – Updated ODEs for implementation in PREDICI® using the tubular reactor mode and the user-input ODE module

0 m ≤ x ≤ 25.2 m	
$$\frac{dP}{dt} = \frac{4\dot{m}_g}{\rho_g \pi {D_i}^2}\left(\frac{\frac{d}{dx}\left(\frac{1}{MW_g}\right) + \frac{1}{MW_g}\left(\frac{1}{T_g}\frac{dT_g}{dx} + Fr\right)}{\frac{1}{MW_g P} - \frac{P}{\alpha R T_g}\left(\frac{\pi D_{ic}}{4\dot{m}_g}\right)^2}\right)$$	**10.1**
$$\frac{dT_g}{dt} = \frac{1}{\rho_g \frac{\pi}{4} {D_i}^2 C_{p,g}}\left(h_{conv+cond}\pi D_o\left(T_{to} - T_g\right) - \frac{r_{crack}\Delta H_{crack}\pi {D_i}^2}{4}\right)$$	**10.2**
0.0 m ≤ x < 12.6 m	
$$\frac{dq^+}{dt} = \frac{-4\dot{m}_g}{\rho_g \pi {D_i}^2}\left(\beta\sigma {T_f}^4 + \frac{\varepsilon_t A_t \sigma}{2}\frac{\sum_{i=1}^{n} {T_{to,i}}^4}{n} - \left(\beta + \frac{\varepsilon_r A_r}{4} + \frac{\varepsilon_t A_t}{2}\right)q^+ + \frac{\varepsilon_r A_r}{4}q^-\right)$$	**10.3**
$$\frac{dq^-}{dt} = \frac{4\dot{m}_g}{\rho_g \pi {D_i}^2}\left(\beta\sigma {T_f}^4 + \frac{\varepsilon_t A_t \sigma}{2}\frac{\sum_{i=1}^{n} {T_{to,i}}^4}{n} + \frac{\varepsilon_r A_r}{4}q^+ - \left(\beta + \frac{\varepsilon_r A_r}{4} + \frac{\varepsilon_t A_t}{2}\right)q^-\right)$$	**10.4**
$$\frac{dT_f}{dt} = \frac{-4\dot{m}_g}{\rho_g \pi {D_i}^2 \dot{m}_f C_{p,f}}\left(\beta A_c\left(q^+ + q^- - 2\sigma {T_f}^4\right)\right)$$	**10.5**
12.6 m ≤ x < 25.2 m	
$$q^+(x) = q^+(25.2 - x)$$	**10.6**
$$q^-(x) = q^-(25.2 - x)$$	**10.7**
$$T_f(x) = T_f(25.2 - x)$$	**10.8**

4.6 Implementation of the furnace-side energy balance in PREDICI®

4.6.1 Implementation of the furnace-side energy balance as an initial value problem in PREDICI®

As described in section 3.1, the furnace is divided into a cold box and a hot box, with a cross-over tube in between the two boxes (see Figure 3). To model the furnace side, these two sections are considered separately. A model of the cold box was developed first, and was then extended to include the hot box and the cross-over tube. It is assumed that half of the total mass flow of the furnace gas to the radiant section enters at the bottom of the

cold box, and half of the total mass flow rate of furnace gas to the radiant section enters at the bottom of the hot box. Assumption 4.21 states that the furnace gas that enters at the bottom of the cold box, flows upward in plug flow and leaves at the top of the cold box. Similarly, the furnace gas that enters the bottom of the hot box flows upward in plug flow and leaves at the top of the hot box. Any crossover of furnace gas between the hot box and the cold box is neglected.

The ODEs derived in section 3.3 for the furnace-side are based on the vertical position *z* within the furnace, where $z = 0$ m is at the bottom. To implement these equations in PREDICI®, this vertical position *z* must be related to the position *x* along the tube length. In section 4.3, boundary conditions were identified by assuming that the top and bottom of the furnace are covered with refractory walls that are radiatively adiabatic. To relate tube position *x* to vertical position *z*, it is also assumed that the tube passes run the full height between the top and bottom refractory walls as shown in Figure 8 (assumption 4.22). The U-bend (shown using dashes in Figure 8) is neglected in the model and any reactions that occur in these sections are ignored. This is a reasonable assumption because the height of the furnace is large compared to the length of the bends. It is important, however, to consider the impact of the U-bends on the process gas pressure. This is done by adding the friction factor for a U-bend to the momentum balance in the small tube sections before and after where the U-bend physically exists. As a result, there is a section of tube (half the length of the U-bend) that has an increased friction factor at the bottom of both of the tubes.

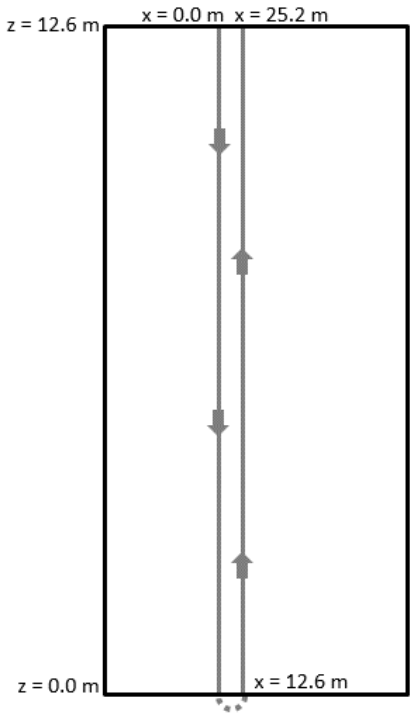

Figure 8 – Relative tube position *x* with furnace height *z* in cold box

The second column of Table 11 shows the linear relationships between *x* and *z* that apply in each of the downward and upward tube passes. Differentiating these expressions with respect to *x* results in the differential equations in the third column of Table 11. Implementation of ODEs 7.18 to 7.20 from

Table 7 in PREDICI® requires that the left-hand sides be derivatives with respect to time rather than position. Relationships between vertical location and time, required to transform ODEs 7.18 to 7.20, are provided in the fourth column of Table 11, and are calculated by multiplying the corresponding expressions for dz/dx by the velocity dx/dt in a coke-free tube.

Table 11 – Relationship between location in tube *x* and vertical location in the radiant section *z*

Reactor location	Vertical location	Relationship between reactor position and vertical location	Relationship between vertical location and PREDICI® time
$0.0 \leq x < 12.6$	$z = 12.6 - x$	$\frac{dz}{dx} = -1$	$\frac{dz}{dt} = \frac{-4\dot{m}_g}{\rho_g \pi {D_i}^2}$
$12.6 \leq x < 25.2$	$z = x - 12.6$	$\frac{dz}{dx} = 1$	$\frac{dz}{dt} = \frac{4\dot{m}_g}{\rho_g \pi {D_i}^2}$

For example, equation 7.18 from

Table 7 can be multiplied on both sides by $\frac{dz}{dt}$ to give:

$$\frac{dq^+}{dt} = \frac{-4\dot{m}_g}{\rho_g \pi {D_i}^2}\left(\beta\sigma {T_f}^4 + \frac{\varepsilon_t A_t \sigma}{2}\frac{\sum_{i=1}^{n} {T_{to,i}}^4}{n} - \left(\beta + \frac{\varepsilon_r A_r}{4} + \frac{\varepsilon_t A_t}{2}\right)q^+ + \frac{\varepsilon_r A_r}{4} q^-\right) \quad \textbf{49}$$

for the first pass ($x = 0.0$ m to 12.6 m) and

$$\frac{dq^+}{dt} = \frac{4\dot{m}_g}{\rho_g \pi {D_i}^2}\left(\beta\sigma {T_f}^4 + \frac{\varepsilon_t A_t \sigma}{2}\frac{\sum_{i=1}^{n} {T_{to,i}}^4}{n} - \left(\beta + \frac{\varepsilon_r A_r}{4} + \frac{\varepsilon_t A_t}{2}\right)q^+ + \frac{\varepsilon_r A_r}{4} q^-\right) \quad \textbf{50}$$

for the second pass ($x = 12.6$ m to 25.2 m).

The furnace gas temperature and radiant fluxes change in the vertical direction in the furnace, but are assumed to be constant in the horizontal direction (assumption 4.11). This means, for example, that the furnace gas temperature is the same at each given vertical position *z* in the cold box. As a result, the upward tube pass is subjected to the same furnace gas temperature and radiative environment as the downward tube pass, so that the ODEs for T_f, q^+ and q^- can be solved for the downward pass (in equations 10.3, 10.4 and 10.5) and the calculated results can be imposed on the upward pass, as shown in equations 10.6, 10.7 and 10.8 in Table 10. Note that solving for T_f, q^+ and q^- for the downward pass requires knowledge of the outer tube wall temperature profile for the upward pass. Additional details are provided below.

With the geometry shown in Figure 8, the various ODE boundary conditions for the radiant fluxes and furnace gas temperature are known at $z = 0$ m and $z = 12.6$ m and therefore $x = 0$ m, $x = 12.6$ m and $x = 25.2$ m. Since the values of q^+, $q^-$and T_f must be the same at $x = 0$ m and $x = 25.2$ m the boundary and initial conditions for the furnace-side ODEs can be defined as:

i. $T_{f\ x=12.6} = T_{comb}$

ii. $q^{+}_{x=0} = q^{-}_{x=0}$

iii. $q^{+}_{x=12.6} = q^{-}_{x=12.6}$

PREDICI® is only able to handle ODEs as initial value problems, and therefore, the first attempt to implement this model in PREDICI® solves this boundary value problem via a shooting method. To do so, initial values (at $x = 0$ m) of T_f, q^+ and q^- are guessed, in the hope that the desired boundary values for $q^{+}_{x=12.6} = q^{-}_{x=12.6}$ and $T_{f\ x=12.6} = T_{comb}$ will be obtained. Based on the simulation results, better guesses for initial values are searched (e.g., using bisection) until initial values are obtained that result in the fulfilment of the specified boundary conditions.

In addition to shooting for the boundary values at $x = 12.6$ m, the unknown tube wall temperature profile for the second (upward) tube pass must be considered. The summation terms used to calculate the radiant fluxes in equations 10.3 and 10.4 require the outer tube wall temperatures $T_{to,i}$ for each tube pass at every vertical position z. The outer tube wall temperature profile on the second pass is unknown when the ODEs are solved for the first (downward) tube pass, so a guess is made for the upward temperature profile (i.e., T_{to} = 900 °C for 12.6 m $< x <$ 25.2 m). After ODEs 10.3 to 10.5 are solved along with the other PREDICI® equations (i.e., material, momentum energy and balances within the tube) between $x = 0$ m and $x = 12.6$ m, an updated tube-wall temperature profile can be calculated by solving the equations between $x = 12.6$ m and $x = 25.2$ m, assuming that the downward tube-wall temperature profile is correct. Iterations can continue until the tube-wall temperature profiles for the downward and upward tube

passes converge. Shooting iterations to satisfy boundary conditions *i.* and *iii.* could then be performed in an outer loop where $q^+{}_{x=0} = q^-{}_{x=0}$ and $T_{f\,x=0}$ are updated.

To simplify the problem, and assess whether this scheme would work in PREDICI®, several simpler cases were attempted. In the first case (see Table 12) the model was solved for the first pass alone, assuming that $q^+{}_{x=0} = q^-{}_{x=0}$ and $T_{f\,x=0}$ are known, and that the tube-wall temperature for the second pass is fixed at 900 °C. From typical plant measurements, the expected temperature of the furnace gas leaving the top of the furnace $(x = 0)$ is ~1018 °C. This value of $T_{f\,x=0}$ was specified for Case 1. The upward radiation absorbed by the refractory wall $\left(\frac{\varepsilon_r A_r}{2} q^+\right)$ must equal the radiation emitted in the downward direction by the refractory wall, which obeys the Stefan-Boltzmann law $\left(\frac{\varepsilon_r A_r}{2} \sigma T_r{}^4\right)$. The value specified for $q^+{}_{x=0} = q^-{}_{x=0}$ was determined by assuming that the refractory wall temperature at the top of the furnace is also 1018 °C, which gives values of $q^+{}_{x=0} = q^-{}_{x=0} = 157.5$ kW·m^2.

Table 12 – Cases used to implement initial value problem in PREDICI®

Case	Purpose	$q^+_{x=0} = q^-_{x=0}$ (kW·m^{-2})	β (m^{-1})	$T_{to=12.6\text{ to }25.2}$ (°C)
1	Initial implementation in PREDICI®	157.5	0.1	900
2	Shooting to satisfy and $q^+_{x=12.6} = q^-_{x=12.6}$	111.055	0.1	900
3	Adjusting β to satisfy $T_{f\,x=12.6} = T_{comb}$ while shooting for $q^+_{x=12.6} = q^-_{x=12.6}$	132.810	0.25	900
4	Iterating to update second-pass tube wall temperature profile	132.810	0.25	$1.464x^2 - 73.98x + 1768.6$
5	Updating second-pass tube wall temperature profile while shooting for $q^+_{x=12.6} = q^-_{x=12.6}$	128.8946	0.25	$1.561x^2 - 80.44x + 1867.3$

The Case 1 results from PREDICI® for the furnace gas temperature and radiant fluxes resulting from the first guesses of initial values are shown in Figure 9.

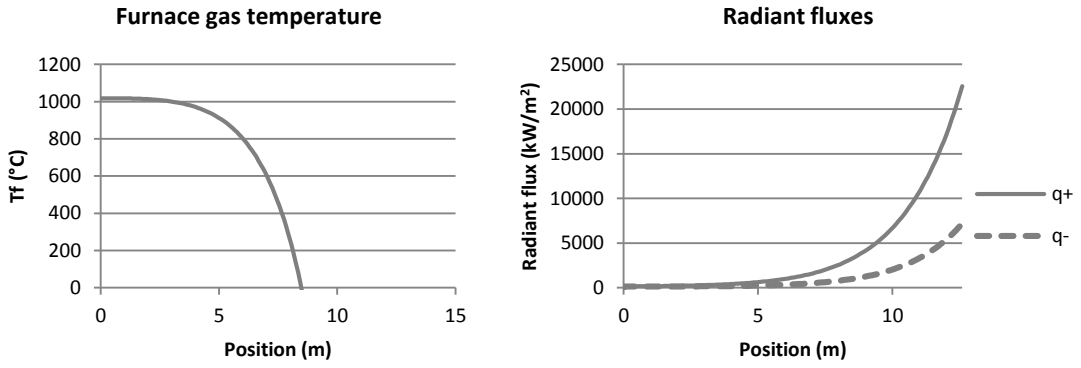

Figure 9 – Furnace gas temperature and radiant flux profiles resulting from Case 1 simulations in PREDICI®

Figure 9 shows that the initial guesses for the values of $q^+_{x=0} = q^-_{x=0}$ chosen for Case 1 were not sufficiently accurate to satisfy the boundary conditions, as expected. These initial values result in the values of the two radiant fluxes diverging towards the bottom of the furnace, and an unrealistic furnace gas temperature profile.

The second case introduced shooting to Case 1 to satisfy the boundary condition $q^+_{x=12.6} = q^-_{x=12.6}$ by adjusting $q^+_{x=0} = q^-_{x=0}$. To keep the simulations simple, no adjustments to $T_{f\,x=0}$ were made in Case 2 to match boundary condition *i.* and it was assumed that the upward-pass tube-wall temperature is fixed at 900 °C. To achieve the results presented in Figure 10 a value of $q^+_{x=0} = q^-_{x=0}$ = 111.055 kW·m^{-2} is used, which corresponds to a refractory wall temperature at the top of the furnace of 910 °C.

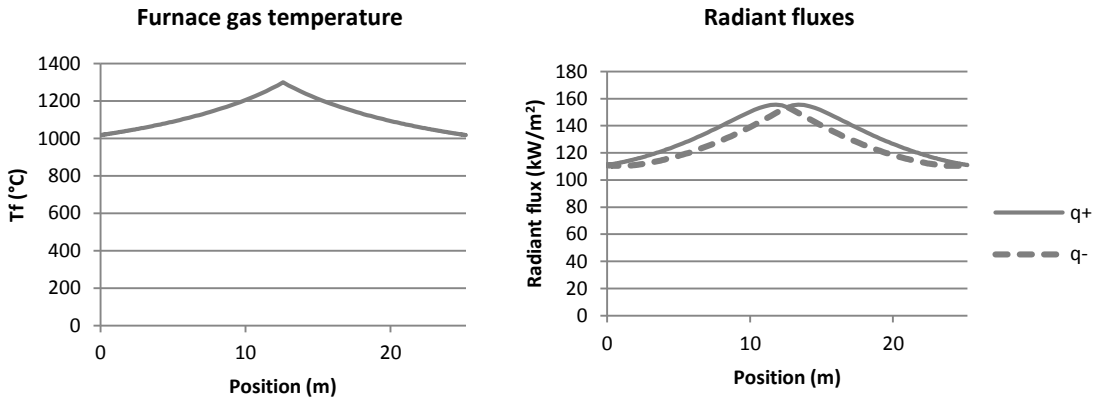

Figure 10 – Furnace gas temperature and radiant flux profiles resulting from Case 2 simulations in PREDICI®

With the fuel composition, mass flow, and residual O_2 indicated in Table 8, the combustion temperature T_{comb} is 1844 °C. As can be seen in Figure 10, the furnace gas temperature is 1300 °C at the bottom of the furnace (x = 12.6 m) in Case 2.

Case 3 is the same as Case 2, except that different values of the parameter β were used in an attempt to get closer to satisfying boundary condition *i.* while still adjusting $q^+_{x=0} = q^-_{x=0}$ to satisfy boundary condition *ii.* β is the fraction of the upward or downward radiation that is absorbed by the furnace gas per meter. This parameter was selected to adjust because it has a strong influence on the furnace-gas temperature profile and its

value is poorly known. Figure 11 shows the result of an increase in β on the furnace gas temperature and radiant flux profiles.

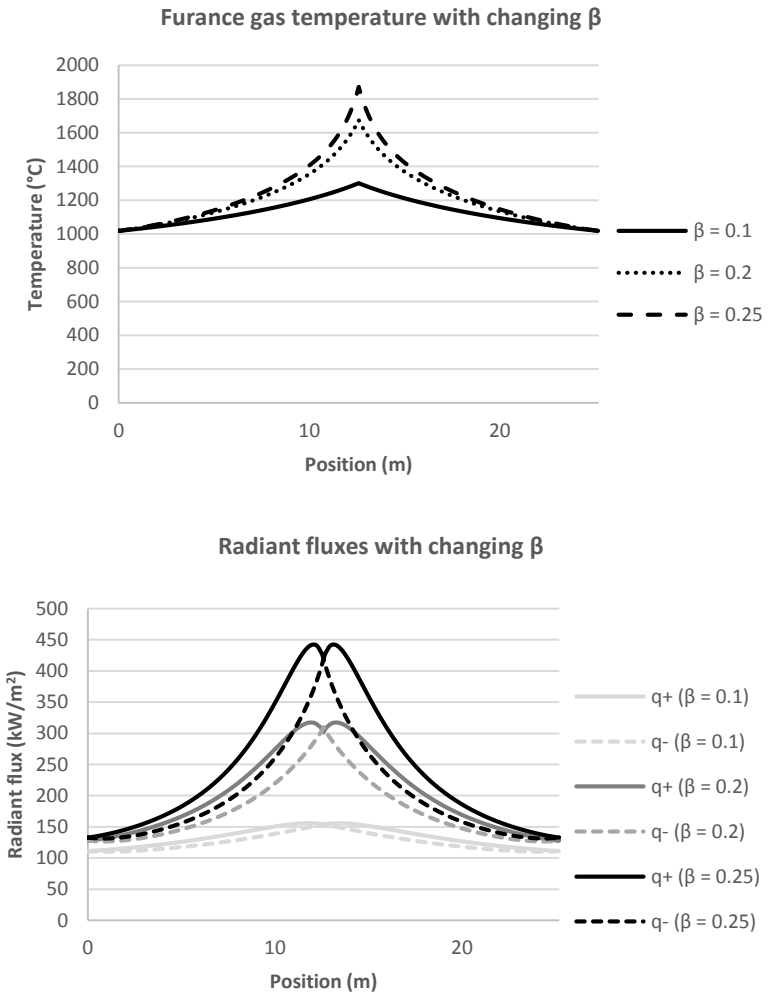

Figure 11 – Furnace gas temperature and radiant flux profiles resulting from Case 3 simulations in PREDICI®

It can be seen in Figure 11 that a choice of $\beta = 0.25$ results in a furnace gas temperature at the bottom of the furnace of 1871 °C, which is close to the combustion temperature of 1844 °C, with $q^+_{x=0} = q^-_{x=0} = 132.810$ kW·m^{-2}. These values of $q^+_{x=0} = q^-_{x=0}$ correspond to a refractory wall temperature at the top of the furnace of 964.1 °C. An increase in β means that there is more interaction of the furnace gas with radiation and, as

a result, radiant flux and furnace gas temperature profiles are more sensitive to changes in $q^+_{x=0} = q^-_{x=0}$. Figure 12 shows how small changes in an equivalent refractory wall temperature T_r at x = 0 m (and therefore $q^+_{x=0} = q^-_{x=0}$) affect the furnace gas temperature and radiant flux profiles when all other values are held constant.

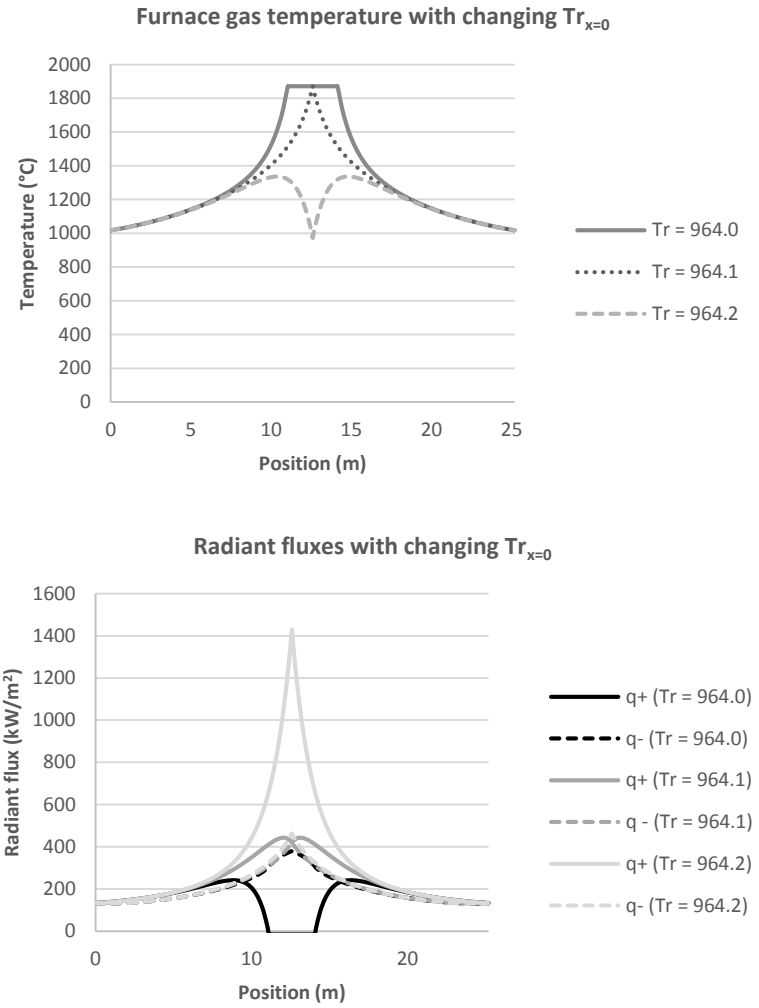

Figure 12 – Effect of changes in refractory wall temperature at the top of the furnace on furnace gas temperature and radiant flux profiles

Case 3 assumed a fixed tube wall temperature for the second pass of 900 °C. Case 4 adds an iteratively-updated tube-wall temperature profile for the second pass generated from Case 3 (fitted by a polynomial) to solve from $x = 0$ m to $x = 12.6$ m. Solving from $x = 12.6$ m to $x = 25.2$ m uses the q^+ and q^- profiles obtained while solving from $x = 0$ m to

$x = 12.6$ m, resulting in an updated tube wall-temperature profile for the second pass, which is then summarized using a polynomial fit.

Several attempts were made to iteratively update the downward and upward pass calculations based on the most recent temperature and radiation profiles, without changing β or $q^{+}{}_{x=0} = q^{-}{}_{x=0}$. Unfortunately, the results did not converge, as shown in Figure 13.

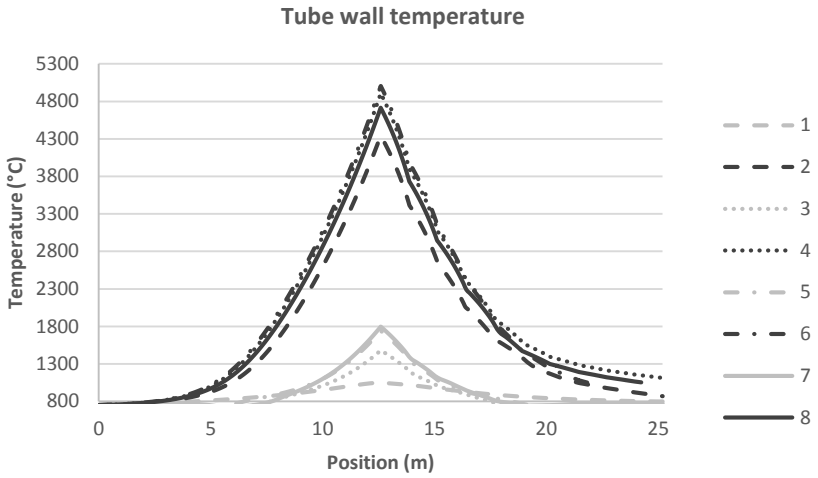

Figure 13 – Tube wall temperature profiles for 8 iterations of Case 4 in PREDICI®. Iteration 1 is the same as Case 3.

As shown in Figure 13, the tube wall temperature profile does not seem to converge, but oscillates up and down as the iterations proceed. This peculiar behavior can be better understood by examining the furnace gas temperature profile for the same runs in Figure 14.

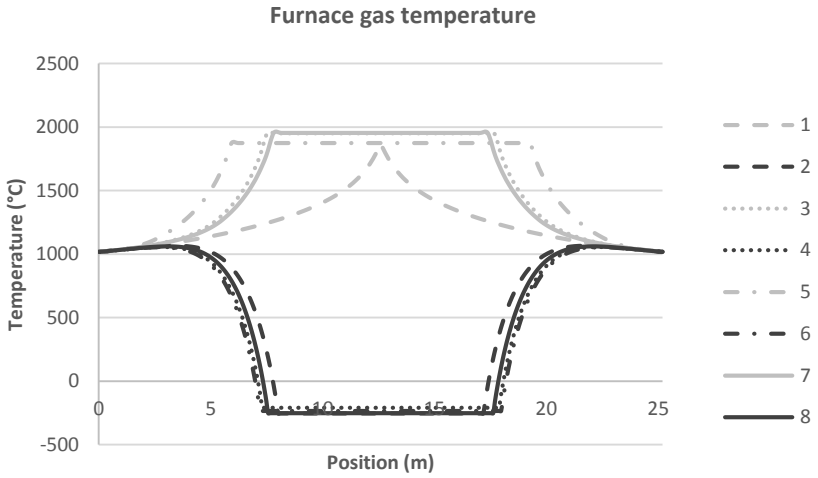

Figure 14 – Furnace gas temperature profiles resulting from 8 iterations of Case 4 in PREDICI® with limits on furnace gas temperature

Limits were set on the furnace gas temperature ODEs so that if the furnace gas temperature became lower than 0 °C or higher than T_{comb} (at any location) then the derivative would be set to zero so that the furnace gas temperature would stop decreasing or increasing to wholly unrealistic values. Figure 14 shows that each alternating iteration with updated tube wall temperature profiles results in either the top or bottom limit of furnace gas temperature being reached. The enforced constant values of the furnace gas temperature at the top and bottom limits keeps the simulations from failing numerically. When these limits are removed, the tube wall temperature profiles do not converge, and the simulation fails at $x = 12.63$ m on the second iteration as shown in Figure 15.

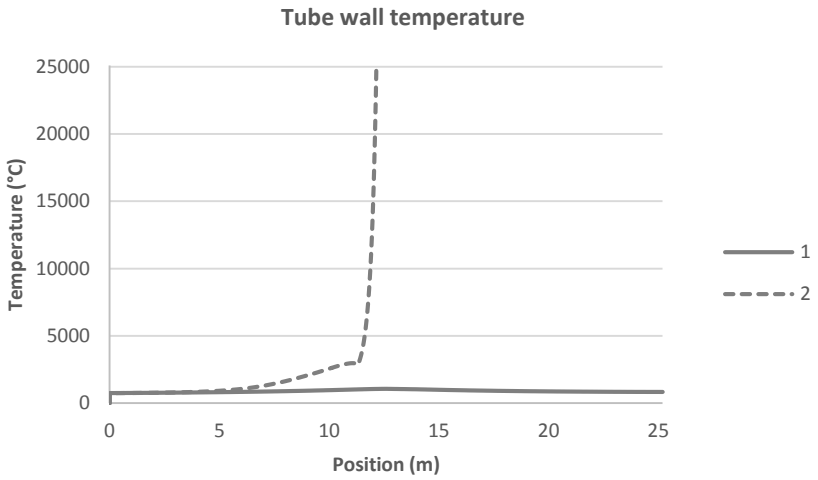

Figure 15 – Tube wall temperature profiles resulting from two iterations of Case 4 in PREDICI® without limits on furnace gas temperature

Figure 14 demonstrates how updating the tube-wall temperature profile can have a significant effect on the furnace gas temperature profile, causing it to reach physically unrealistic values. This result is due to the effect of the values of ${q^+}_{x=0} = {q^-}_{x=0}$ on the furnace gas temperature profile as demonstrated in Figure 12. Case 5 was used to find out whether updating the values of ${q^+}_{x=0} = {q^-}_{x=0}$ to satisfy boundary condition *iii*. (after updating the tube wall temperature profile in each iteration) would be helpful. This approach produced more reasonable results, as shown in Figure 16.

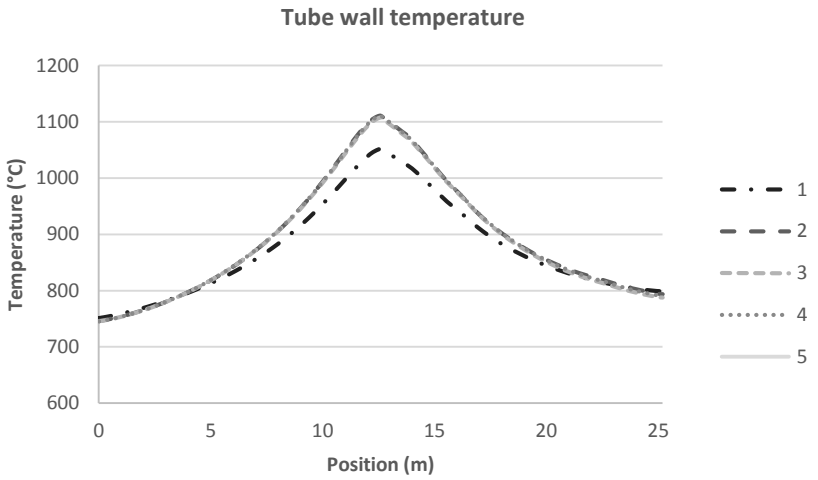

Figure 16 – Updated tube wall temperature profiles for five iterations of Case 5 in PREDICI®

It can be seen in Figure 16 that the tube wall temperature profile converges nicely, but even though the tube wall temperature profiles are nearly identical for the last four iterations, each iteration still requires a unique and precise initial value of q^+ and q^- as shown in Table 13.

Table 13 – Updated second-pass tube wall temperature profiles with associated radiant flux initial conditions for implementation in PREDICI®

Iteration	$\boldsymbol{T_{to}}$ (°C)	$\boldsymbol{q^+_{x=0} = q^-_{x=0}}$ (kW·m^{-2})
1	900	132.810
2	$1.447x^2 - 75.24x + 1775.4$	127.4537
3	$1.719x^2 - 90.62x + 1985.3$	127.3528
4	$1.663x^2 - 88.72x + 1966.8$	127.1122
5	$1.6912x^2 - 89.78x + 1978.8$	127.2550

The furnace gas and radiant flux profiles resulting from the fifth iteration in Table 13 are shown in Figure 17.

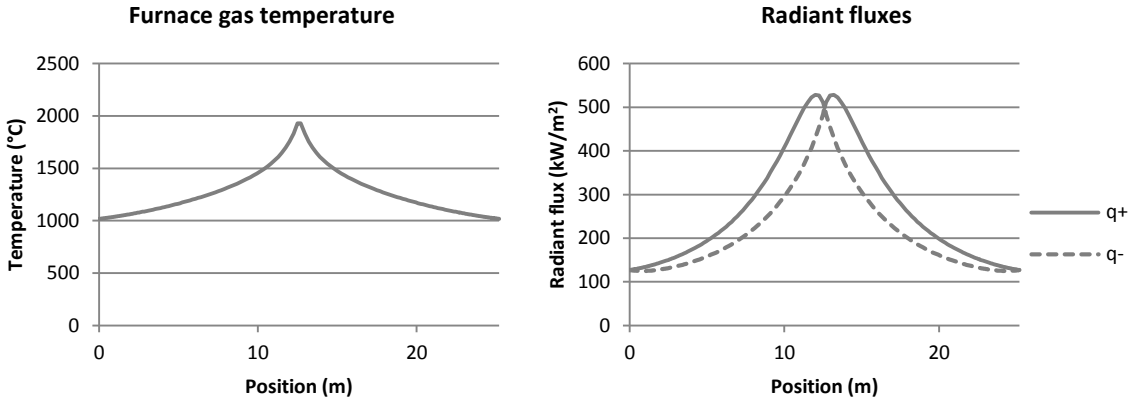

Figure 17 – Furnace gas temperature and radiant flux profiles resulting from Case 5 in PREDICI®

Figure 17 shows that boundary conditions *i*. and *iii*. are nearly met with the updated tube wall temperature profile shown in Figure 16. The process gas temperature, conversion of ethane and yield of ethylene for the same case are shown in Figure 18.

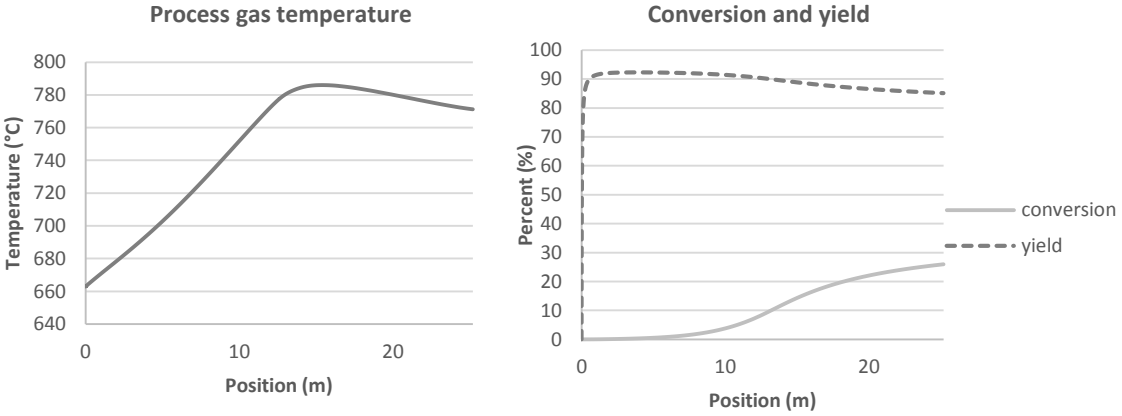

Figure 18 – Process gas temperature, conversion and yield profiles resulting from Case 5 simulations in PREDICI®

The development of Case 1 through Case 5 shows that solving this boundary value problem via shooting and the corresponding initial value problem in PREDICI® requires many iterations. The results in Figures 17 and 18 were obtained using considerable manual intervention (e.g., fitting of the updated tube wall temperature profiles and restarting PREDICI® using the updated profile as an input). Apart from the significant effort required to produce simulation results for a single operating condition, the results

are also very unstable, with only a small change in the initial values of q^+ and q^- often resulting in physically unrealistic furnace gas temperature profiles. Therefore, it was concluded that these model equations do not solve well as an initial value problem in PREDICI®.

One of the overall objectives for this modeling project is to obtain updated estimates for key model parameters, using plant data. Parameter estimation involves repeated solution of the model equations for a variety of parameter values. Based on the preliminary results above, a more robust means of solving the model equations is desirable so that the model can be used for parameter estimation.

4.6.2 Implementation of the furnace-side energy balance as a boundary value problem in MATLAB®

Instead of solving the model equations as an initial value problem with shooting, they can be solved be solved with fewer computational difficulties in other ways. One simple method to solve the solve the boundary value problem is to discretize the ODEs using finite differences and then solve the then solve the resulting system of algebraic equations. This approach eliminates the convergence convergence problems associated with shooting. After backward-difference discretization using discretization using finite differences, the process-gas energy balance, equation 7.17 in

Table 7:

$$\frac{dT_g}{dx} = \frac{1}{\dot{m}_g C_{p,g}}\left(h_{conv+cond} D_o \pi \left(T_{to} - T_g\right) - r_{crack} \Delta H_{crack} \frac{\pi}{4} {D_{ic}}^2\right) \quad \textbf{7.17}$$

becomes:

$$\frac{T_{g,i} - T_{g,i-1}}{\Delta x} = \frac{1}{\dot{m}_g C_{p,g}}\left(h_{conv+cond} D_o \pi \left(T_{to} - T_{g,i}\right) - r_{crack} \Delta H_{crack} \frac{\pi}{4} {D_{ic}}^2\right) \quad \textbf{51}$$

at discrete positions i for $i = 1$ to n_s where n_s is the number of sections used in the discretization. If $n_s = 6$ then there are 6 algebraic equations to approximate the single ODE, with discrete values of T_g at 7 locations. The value of T_g is known at position $x = 0$ m which results in unknown values of T_g at 6 locations and 6 algebraic equations. The same approach can be used to discretize the other process-gas side ODEs.

The ODEs on the furnace-gas side are also discretized using backward-difference approximations. The furnace gas temperature $T_{f\ x=12.6}$ is known, which results in 6 equations and 6 unknowns. The values of the radiant fluxes are unknown at all 7 positions, but adding the known conditions ${q^+}_{x=0} = {q^-}_{x=0}$ and ${q^+}_{x=12.6} = {q^-}_{x=12.6}$ results in 14 algebraic equations and 14 unknowns.

The smaller the choice of Δx, the better the set of algebraic equations approximates the ODEs, but with a decrease in Δx there is an increase in the number of model equations to be solved. A coarse, 6-section discretization (Δx = 4.2 m) for all the ODEs developed in Chapter 3 would result in 198 equations, without considering coke formation or the change in any properties (e.g. density, molecular weight, heat capacity, viscosity, conductivity, etc.) with changes in temperature, pressure or composition. If the number of

sections is increased to 40 (Δx = 0.63 m), the resulting number of algebraic equations increases to 1320.

The goal of this preliminary MATLAB® study was to determine whether this radiative heat-transfer boundary-value problem can be readily solved, without numerical problems, using the discretization approach. One way to reduce the number of equations that have to be solved is to simplify the treatment of the process gas. Nearly all of the heat consumed by reactions on the process-gas side is due to the main cracking reaction:

$$C_2H_6 \rightarrow C_2H_4 + H_2 \qquad \textbf{52}$$

To reduce the number of algebraic equations that need to be solved, only this reaction and its associated species were considered in this preliminary model, which was implemented using MATLAB®. Neglecting the other process-side species decreases the number of algebraic equations (using 6 discrete sections) from 198 to 56. The MATLAB® code for the discretized ODEs and related algebraic equations are shown in Appendix C for the case where Δx = 4.2 m. Similar equations were developed and solved for smaller values of Δx.

Figure 19 shows the furnace gas temperature and radiant flux profiles resulting from discretization into 6 (Δx = 4.2 m), 12 (Δx = 2.1 m), 20 (Δx = 1.26 m) and 40 (Δx = 0.63 m) sections of reactor length.

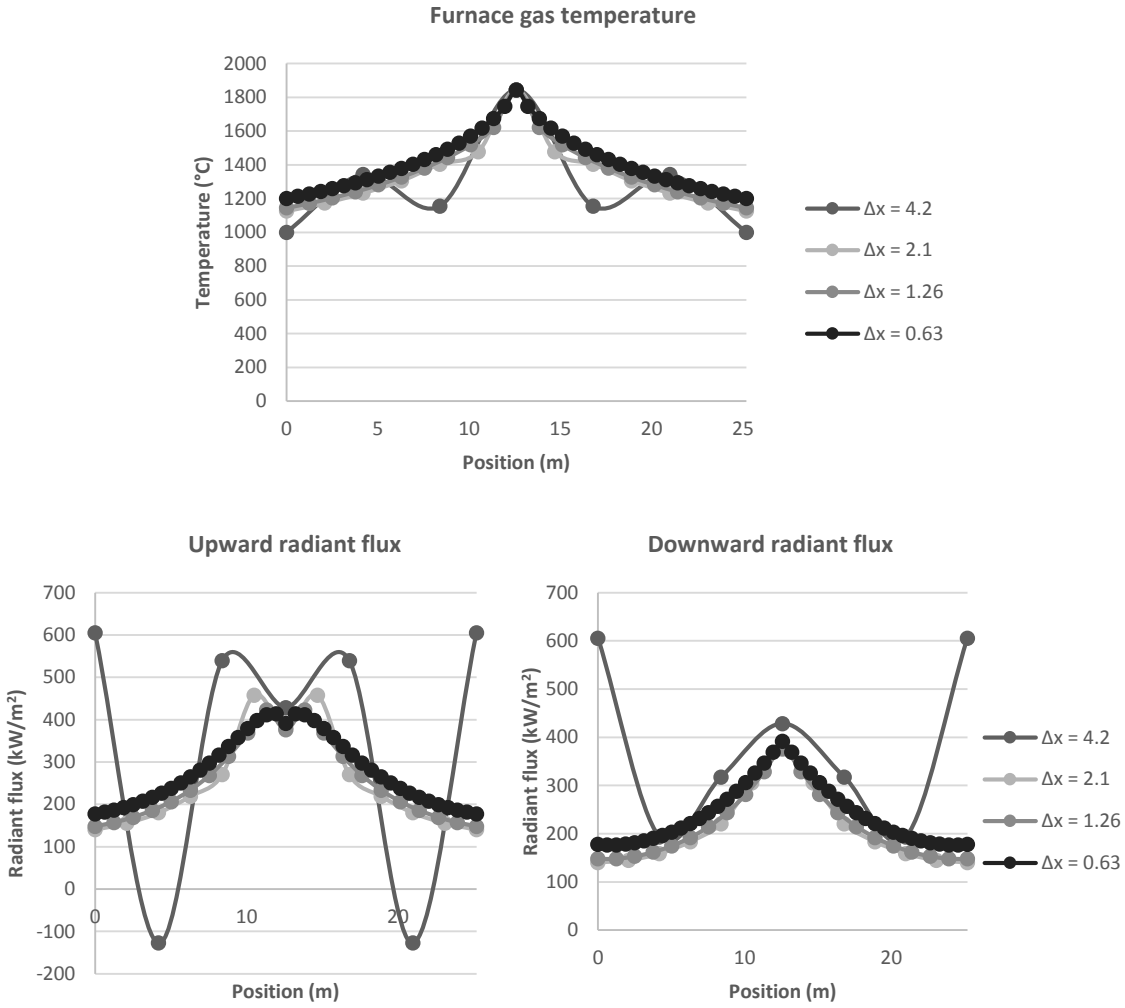

Figure 19 – Furnace gas temperature and radiant flux profiles from simple discretized model in MATLAB® with varying discrete tube section lengths Δx

As can been seen in Figure 19, a decrease in Δx provides smoother results. Dividing the tube into 40 sections, corresponding to $\Delta x = 0.63$ m, appears to be a fine enough discretization to produce reasonably smooth results, which do not change appreciably from the 20-section discretization. This 40-section discretization corresponds to solving a system of 1385 equations and 1385 unknowns.

The furnace gas temperature profile in Figure 19 shows the temperature ranging from the combustion temperature of 1844 °C at the bottom of the furnace, to a temperature of 1200

°C at the top. The value of β can be adjusted so that the temperature at the top of the furnace better matches the typical operating condition of 1018 °C, the same as in the initial value problem in section 4.6.1. In the case of the boundary value problem, the system of unknowns can be adjusted so that $T_{f\ x=0}$ is known at 1018 °C, $T_{f\ x=12.6}$ is known at T_{comb} and β is unknown. The result is $\beta = 0.4357$ m^{-1} corresponding to the furnace gas temperature and radiant flux profiles shown in Figure 20.

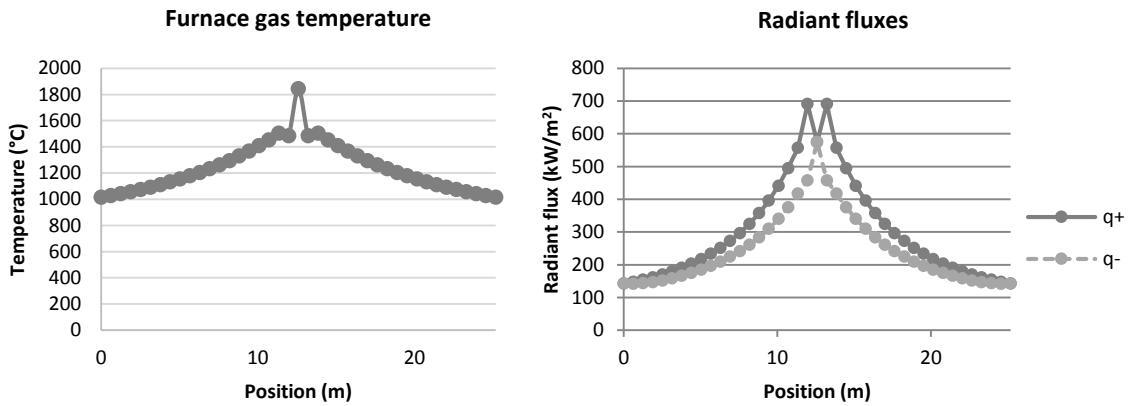

Figure 20 – Furnace gas temperature profile from simple discretized model in MATLAB® with β = 0.4357 m^{-1} and Δx = 0.63 m

When β is increased to 0.4357 m^{-1} it appears that a discretization of $\Delta x = 0.63$ m may not be fine enough. The furnace gas temperature profile shown in Figure 20 exhibits strange up-and-down behaviour at the bottom of the furnace, for which there is no obvious physical explanation. As expected, using a finer discretization (Δx = 0.315 m) eliminates this oscillatory behavior in predicted furnace gas temperature and creates a profile that increases smoothly from the top of the furnace to the bottom as shown in Figure 21.

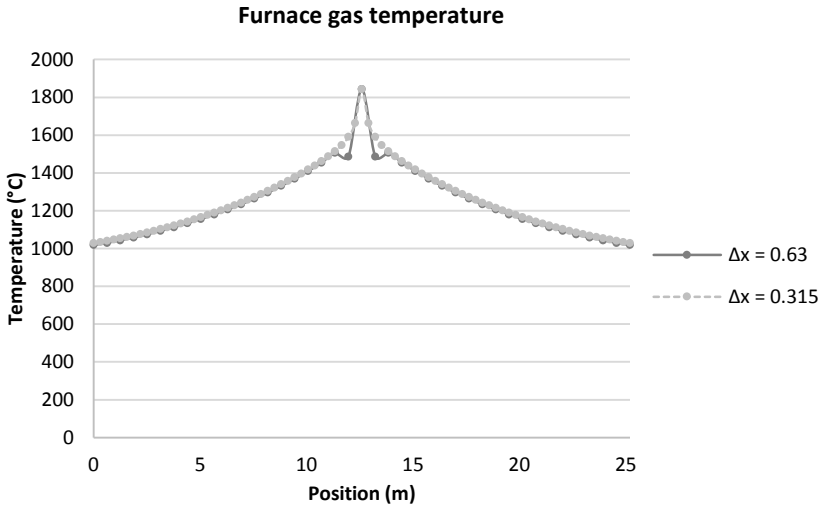

Figure 21 – Furnace gas temperature profile from simple discretized model in MATLAB® for Δx = 0.63 m and Δx = 0.315 m with β = 0.4357 m^{-1}

With an increase in the number of sections used for discretization, there is a slight difference in furnace gas temperature profile as shown in Figure 21. With $\beta = 0.4357$ m^{-1} the temperature of the furnace gas exiting at the top is 1029 °C, slightly different than the typical operating value of 1018 °C. If β is once again adjusted so that $\beta = 0.5460$ m^{-1} then the temperature of the furnace gas exiting the furnace is 1018 °C as shown in Figure 22.

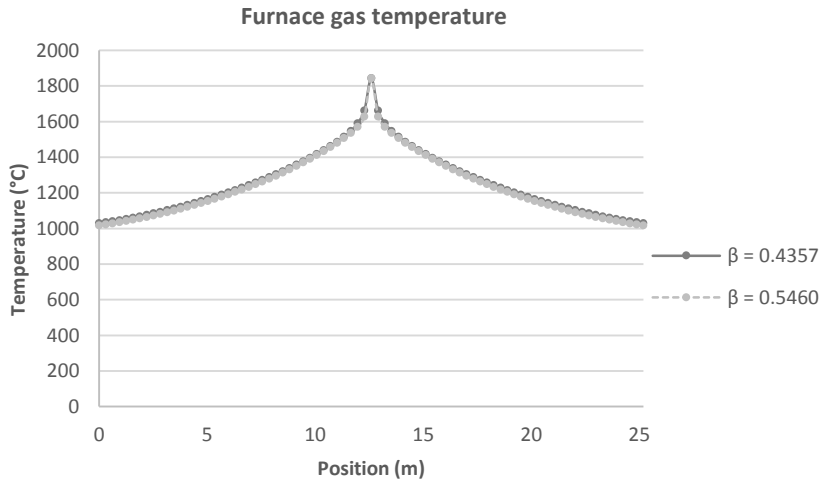

Figure 22 – Furnace gas temperature profile from simple discretized model in MATLAB® for Δx = 0.315 m with β = 0.4357 m^{-1} and β = 0.5460 m^{-1}

This value of β is used as an initial guess for the parameter value and can be tuned using parameter estimation in future work. The discretization with (Δx = 0.315 m) results in a system of 2745 equations and 2745 unknowns.

Figure 23 shows the radiant-flux, furnace gas temperature, tube wall temperature and process gas temperature profiles resulting from the simplified discretized model for different values of β when Δx = 0.315 m.

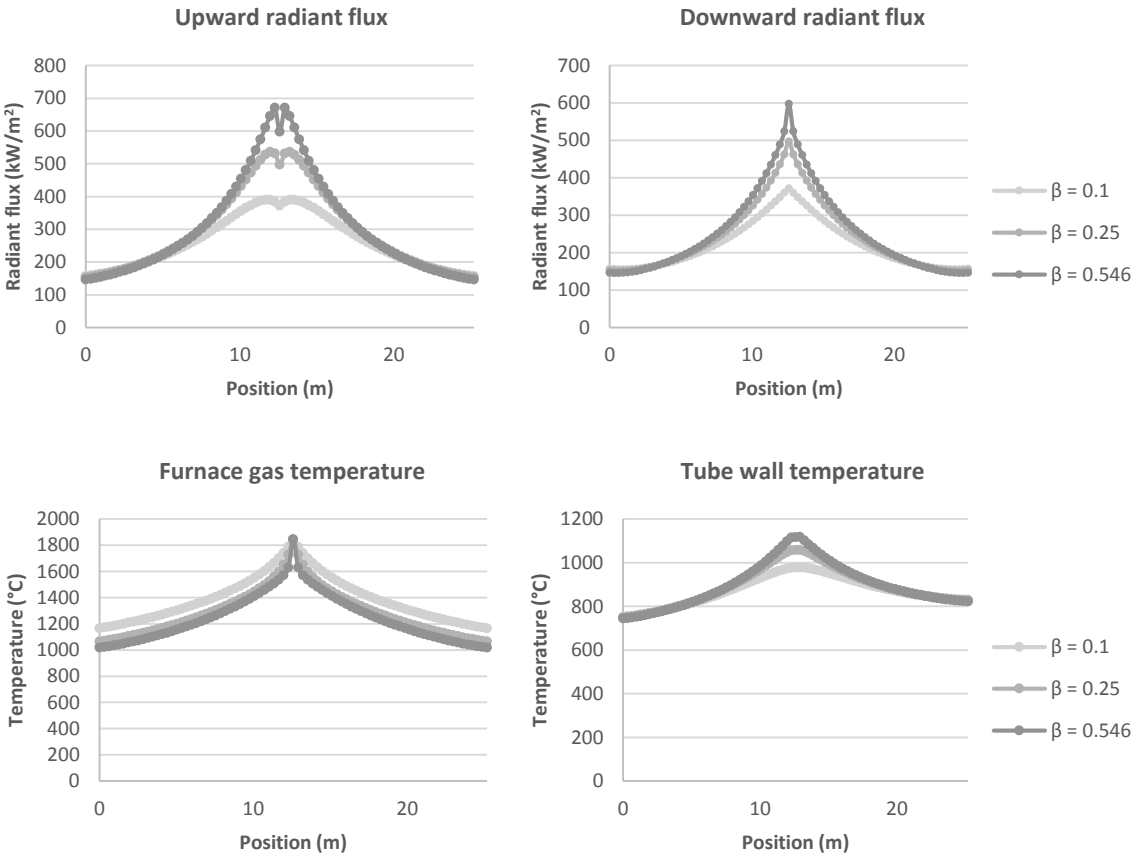

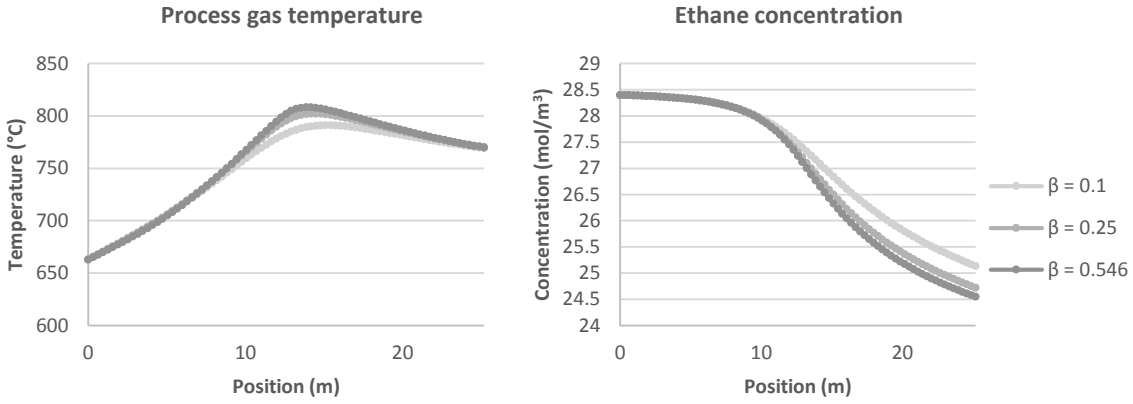

Figure 23 – Radiant flux, furnace gas temperature, tube wall temperature, process gas temperature and ethane concentration profiles from simplified discretized MATLAB® model ($\Delta x = 0.315$ m) for different values of β

This MATLAB® study shows that this radiative heat-transfer boundary-value problem can be readily solved with different parameter values using discretization, without any numerical problems.

4.6.3 Implementation of the furnace-side energy balance a boundary value problem in PREDICI®

One practical way to solve the radiant heat-transfer problem inside the furnace is to calculate the furnace gas temperature and radiant flux profiles (using the discretized simplified model) and then impose those results on the full process-gas side model in PREDICI®. Figure 24 shows the process gas temperature, tube wall temperature, ethane conversion and ethylene yield profiles resulting from imposing the radiant flux profiles calculated in MATLAB® on the full process-gas side model in PREDICI®.

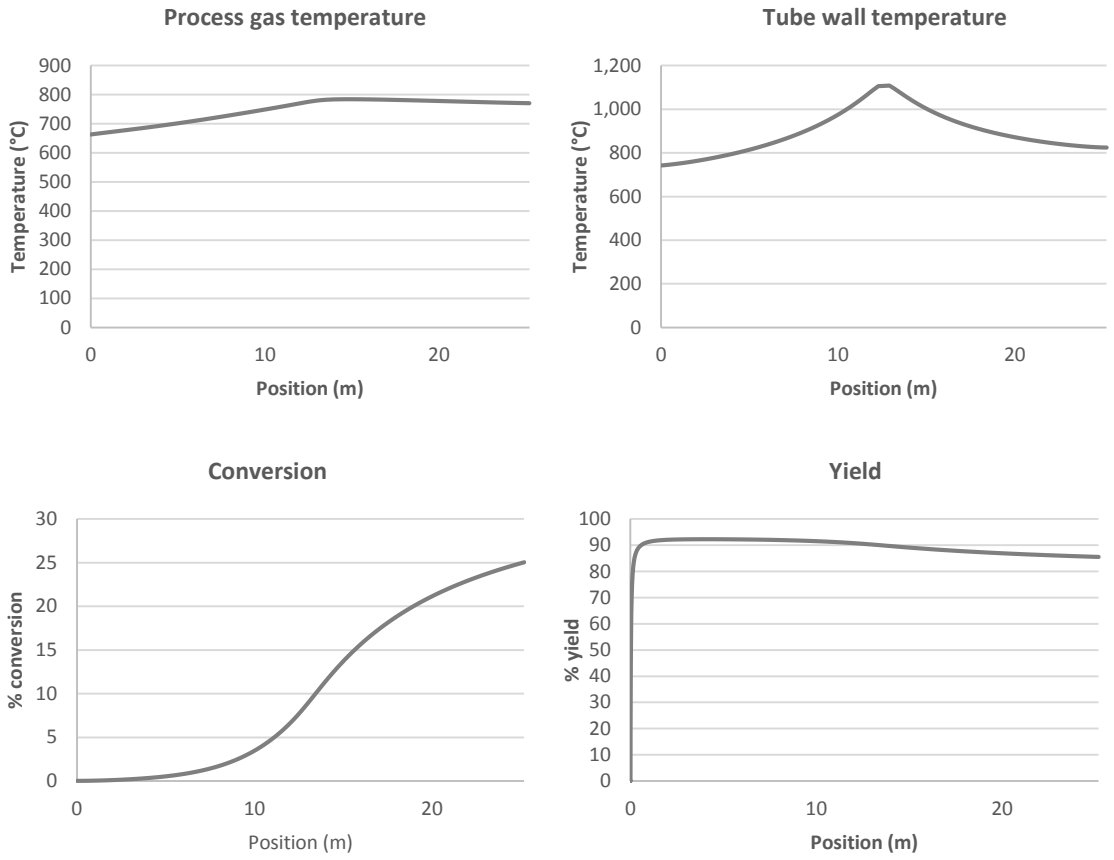

Figure 24 – Process gas temperature, tube wall temperature, conversion and yield profiles resulting from imposing radiant flux profile calculated in MATLAB® ($\Delta x = 0.315$ m, $\beta = 0.5460 m^{-1}$) on full process-side model in PREDICI®

It is not practical, however, for model users from NOVA Chemicals to have to solve for the radiant flux profile in MATLAB®, and then insert it manually into the PREDICI® model. Therefore, it is desirable to solve this system of 2745 equations and 2745 unknowns directly in PREDICI®.

The system of algebraic equations and unknowns can be solved in PREDICI® using an additional "imaginary" reactor. The "imaginary" reactor is first used to solve the system of algebraic equations, and then these results are called into the "real" reactor. This approach was used successfully by Armitage et al.[52] and was recommended to me by Dr. Michael Wulkow, the developer of PREDICI®.

Unfortunately, the current version of PREDICI® cannot easily solve "imaginary" reactor equations along with a *tubular* reactor model because of the complicated way that tubular reactors are handled by PREDICI®. Instead, the tubular reactor model (described in section 4.5) is implemented using the simpler PREDICI® batch reactor features, without any implicit conversion between position and time. The PREDICI® batch reactor model is then converted explicitly to account for tubular reactor operation. The implementation is not straightforward, and a full description is provided in Appendix D.

From the results of the MATLAB® study in section 4.6.2, it was determined that an 80-section discretization is appropriate to solve for the radiant fluxes using a simplified model. An 80-section discretization corresponds to a system of 2745 equations and 2745 unknowns. Early attempts to solve the discretized, simplified model in an "imaginary" reactor in PREDICI® used coarser discretization to limit the number of required equations while verifying that the proposed approach would work. The approach was successful for discretization using 6 sections, 20 sections and 40 sections over the length of the tube in the cold box (i.e., 3 sections, 10 sections and 20 sections over the height of the furnace). The model predictions for process gas temperature, tube wall temperature, conversion and yield are shown in dashed lines in Figure 25 for the model that uses 40 sections of tube length. The solid line Figure 25 shows that solving the system of equations in MATLAB® and imposing the resulting radiant flux profiles in PREDICI® yields the same model predictions as solving the system of equations directly in PREDICI®.

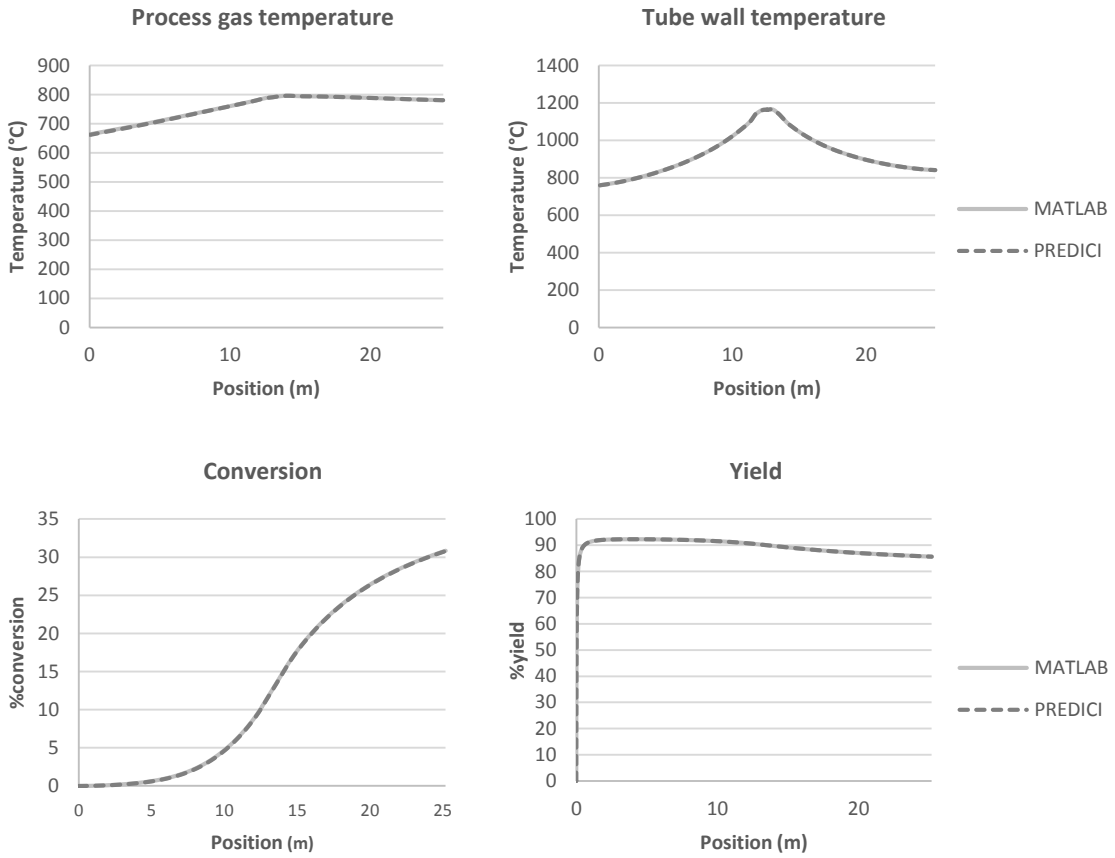

Figure 25 – Comparison of process gas temperature, tube wall temperature, conversion and yield profiles resulting from imposing fluxes calculated in MATLAB® vs PREDICI®

When the more accurate model with 80 discrete sections along the length of the reactor (40 sections over the height of the furnace) was implemented in PREDICI® (with 2745 equations and 2745 unknowns), the program crashed at a position around 11 m, without displaying an error message. The lack of an error message suggests that PREDICI® may not be able to handle the large number of equations and unknowns. To evaluate whether the use of the 40-section model ($\Delta x = 0.63$ m), as opposed to the 80-section model ($\Delta x = 0.315$ m), would significantly affect model predictions, the flux profiles calculated in MATLAB® for the two models with $\beta = 0.4357$ m^{-1} were imposed in PREDICI®. The results are shown in Figure 26.

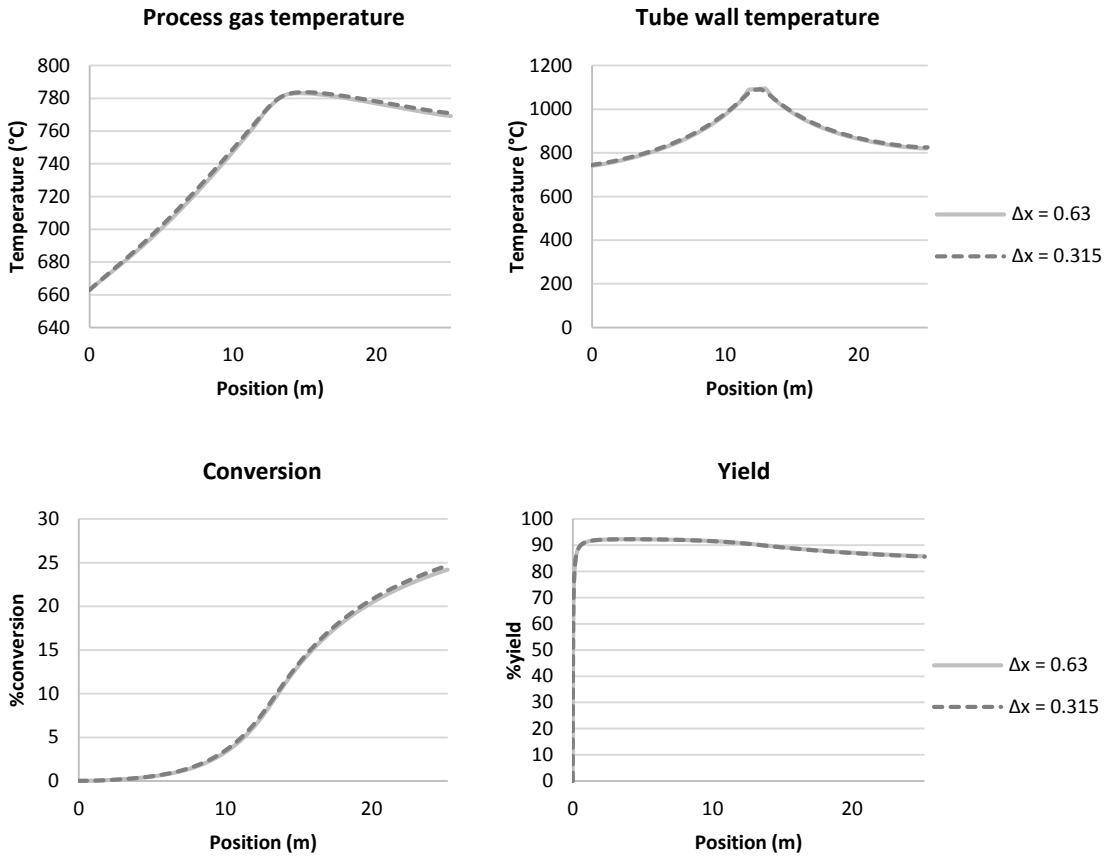

Figure 26 – Comparison of tube wall temperature, process gas temperature, conversion and yield profiles resulting from imposing flux profiles from discretized model with $\Delta x = 0.63$ m and $\Delta x = 0.315$ m in PREDICI®

The results in Figure 26 show that there is not a significant difference in tube wall temperature, process gas temperature, conversion or yield between using the 40-section discretization and the 80-section discretization. Therefore, the 40-section discretization is used throughout the remainder of this thesis.

4.6.4 Extension of the cold-box furnace-side energy balance to include the hot box in PREDICI®

As discussed in section 4.3, the hot box of the radiant section was excluded from initial implementation attempts in PREDICI® as a simplification. With the cold-box model successfully implemented, the model was extended to include the hot box. First,

PREDICI® solves the 1385 equations with 1385 unknowns to obtain the radiant flux profiles in the cold box. Next, PREDICI® integrates the model equations up to $x = 25.2$ m where the tube leaves the cold box and enters the cross-over part of the furnace between the cold and hot boxes. In this cross-over part of the furnace, the radiant conditions are assumed to be the same as those at the top of the cold box as stated in assumption 4.23. PREDICI® uses this flux information while integrating from $x = 25.2$ m to $x = 31.4$ m where the tube enters the hot box. At this point, PREDICI® is used to solve the 1385 equations with 1385 unknowns that apply in the hot box, before continuing the model integration to $x = 56.6$ m.

The geometry in the hot box is assumed to be similar to the geometry in the cold box, so the 1385 hot-box equations are the same as the 1385 cold-box equations. The only differences are the inlet conditions associated with the temperature, pressure and composition of the gas within the tube and the slightly larger tube diameter that is used within the hot box. This larger diameter was used in the furnace design because more coke tends to form in the hot box than in the cold box.

Note that some numerical issues were encountered using this approach due to the quality of the initial guesses for solving the 1385 hot-box equations, as discussed in detail in Appendix D. Resolution of these numerical issues using improved initial guess resulted in successful solution of the PREDICI® model for the full radiant section, as shown in Figure 27 for the base-case conditions in Table 8.

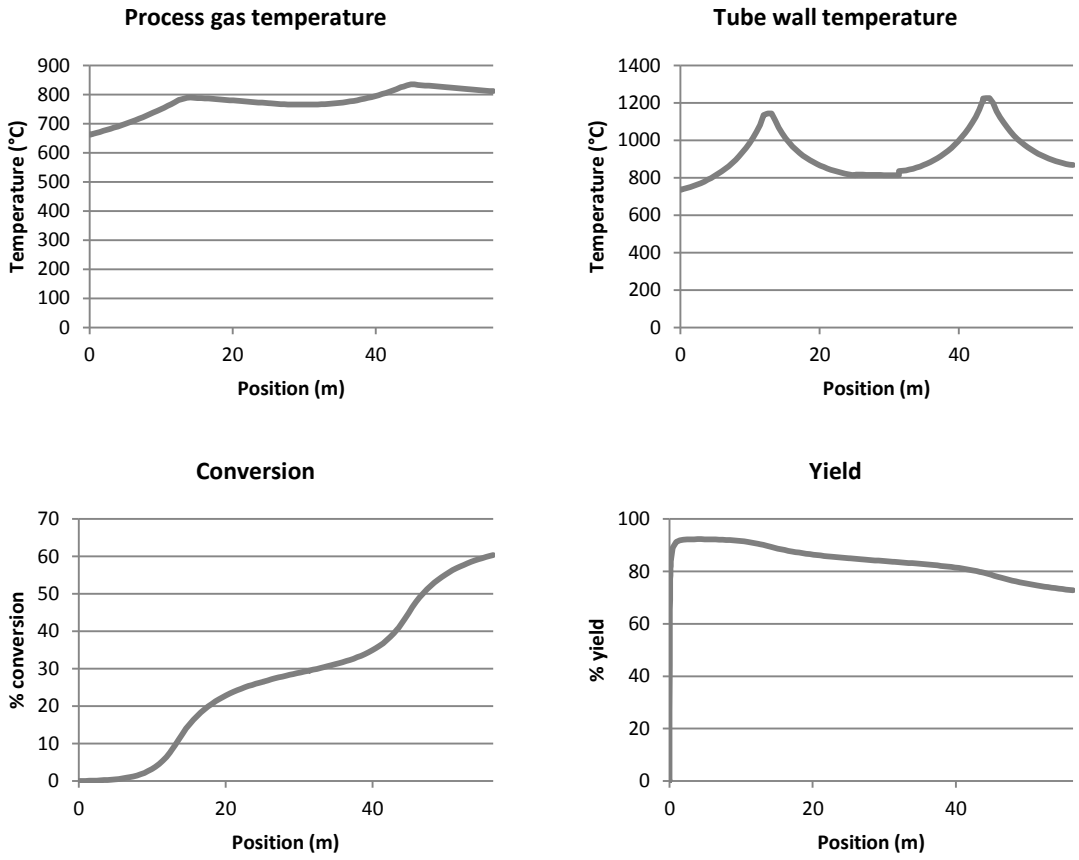

Figure 27 – Process gas temperature, tube wall temperature, conversion and yield profiles resulting from the full radiant-section model solved in PREDICI®

Chapter 5 – Simulation study

The performance of the floor-fired, radiant-section ethane-pyrolysis model implemented in PREDICI® in Chapter 4 was explored using a simulation study. Unfortunately, the operating data that have been collected so far are for a side-fired furnace and therefore model predictions cannot be directly compared to industrial operating data. Model predictions can however be compared to SPYRO® predictions to examine how the proposed model compares to the industrially available (but less flexible and less understood) software. The results are shown in Table 14.

Table 14 – Comparison of model predictions from the proposed PREDICI® model to SPYRO® model predictions

Predicted variable	PREDICI®	SPYRO®	Difference
Outlet ethane conversion (%)	60.4	59.0	2.4%
Outlet ethylene yield (%)	72.8	81.9	12.5%
Outlet process gas pressure (bar_{abs})	1.6	1.7	6.2%
Outlet process gas temperature (°C)	813	840.5	3.4%

Without any tuning of the proposed PREDICI® model, the outlet ethane conversion, ethylene yield, process gas temperature and process gas pressure predicted by the PREDICI® model are similar to the SPYRO® predictions. The conversion predicted by PREDICI® is only 2.4 % higher than the conversion predicted by SPYRO®, as seen in Table 14, and the greatest difference in model predictions comes from the prediction of the outlet ethylene yield. The PREDICI® model predicts an outlet ethylene yield of 72.8%, 12.5% lower than the 81.9% yield predicted by SPYRO®.

It is a good sign that the predictions from the PREDICI® model are similar to the predictions from the SPYRO® model. Although plant engineers rely on SPYRO® industrially, it has its own limitations in terms of accuracy. Comparisons of model predictions to industrial data are a much better means of evaluating model performance. It should also be noted that some model inputs specified in the PREDICI® model could not be specified in the SPYRO® model (i.e. inlet coil pressure, mass flow rate of fuel, etc.).

Model performance was also investigated by observing how model predictions change in response to changes in key model inputs, and how much these model inputs could be changed from their base values before PREDICI® could no longer solve the model equations without manual intervention (i.e., updating of initial guesses). The key model

inputs that were investigated in this simulation study and their base values are presented in Table 15.

Table 15 – Model inputs varied in simulation study sensitivity analysis

Symbol	Description	Base value	Units
$\dot{m}_{fuel}$	Mass flow rate of fuel	0.830	kg/s
$\dot{m}_g$	Mass flow rate of process gas	0.509	kg/s
T_{g0}	Inlet process gas temperature	663	°C
$\dot{m}_{H_2O}:\dot{m}_{C_2H_6}$	Steam to ethane ratio	0.291	dimensionless

Table 16 shows how much model inputs could be either increased or decreased (one at a time) from their base value before PREDICI® produced an error message while solving the model equations. The cells shaded in light grey in Table 16 indicate successful simulations whereas the cells shaded in dark grey indicate conditions where the model solution fails.

Table 16 – Evaluation of model capability to handle changes in mass flow rate of fuel, mass flow rate of process gas, inlet temperature of process gas and steam to ethane mass flow ratio

Symbol	-50%	-30%	-20%	-10%	-5%	base	+5%	+10%	+20%	+30%	+50%
$\dot{m}_{fuel}$											
$\dot{m}_g$											
T_{g0}											
$\dot{m}_{H_2O}:\dot{m}_{C_2H_6}$											

Table 16 indicates that the current model is limited in the range of operating conditions that it is able to simulate without manual intervention. In the cases where the model fails, it is due to the same numerical issues mentioned in section 4.6.4 and discussed in Appendix D, which have to do with the quality of initial guesses for solving the 1385 algebraic equations (usually in the hot box, but sometimes in the cold box). In some cases, numerical issues can be resolved by manually updating initial guesses, however

future work should resolve these numerical issues so that manual intervention will not be required during parameter estimation studies.

Model predictions for process gas temperature, process gas pressure and conversion profiles obtained by perturbing the absolute inlet process gas temperature by ± 5% and the mass flow rate of fuel, mass flow rate of process gas, and steam to ethane mass ratio by ± 10% (one at a time) are shown in Figure 28 through Figure 31. The furnace gas temperature, tube wall temperature and yield profiles resulting from the same changes in model inputs are provided in Appendix E.

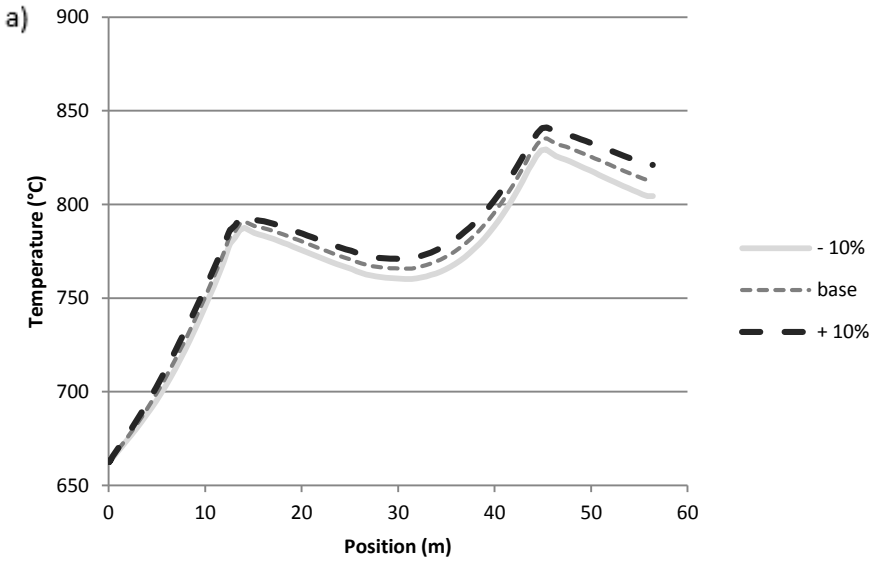

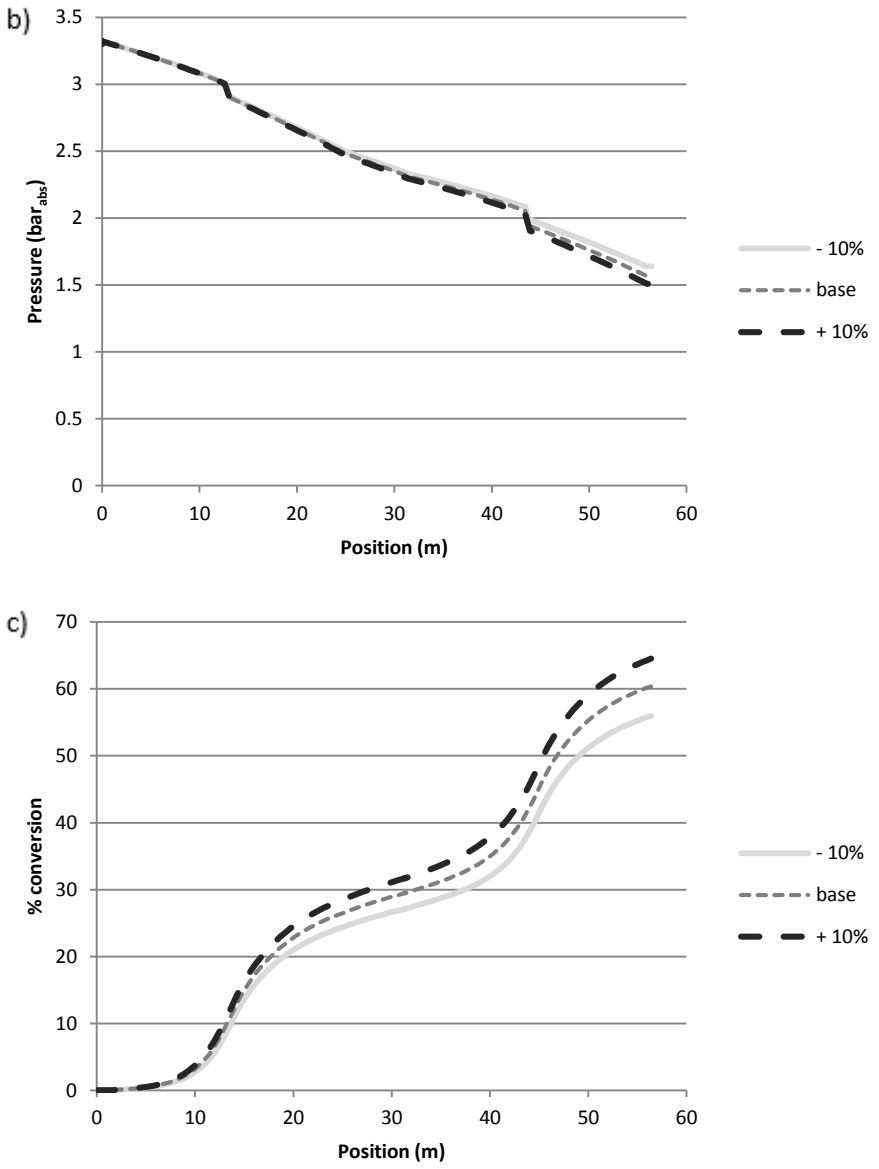

Figure 28 – Model predictions of a) process gas temperature, b) process gas pressure and c) ethane conversion in response to changes in mass flow rate of fuel

With an increase in mass flow rate of fuel there is an increase of heat input to the furnace and therefore it is expected that the rate of heat transfer to the tubes would increase. Figure 28 shows that the temperature of the process gas and conversion are both increased with an increase in the mass flow rate of fuel, as expected. Since the ethane cracking reaction is endothermic, the only way that there can be an increase in both conversion and process gas temperature is if there is an increase in heat transferred to the

process gas. Therefore, the model predictions of conversion and process gas temperature in response to a change in the mass flow rate of fuel behave as expected. The pressure profile shown in Figure 28 does not change significantly with an increase in mass flow rate of fuel, decreasing only slightly.

Figure 29 presents the effect of a change of ± 10% in the process gas flow rate $\dot{m}_g$ on the process gas temperature, pressure and ethane conversion.

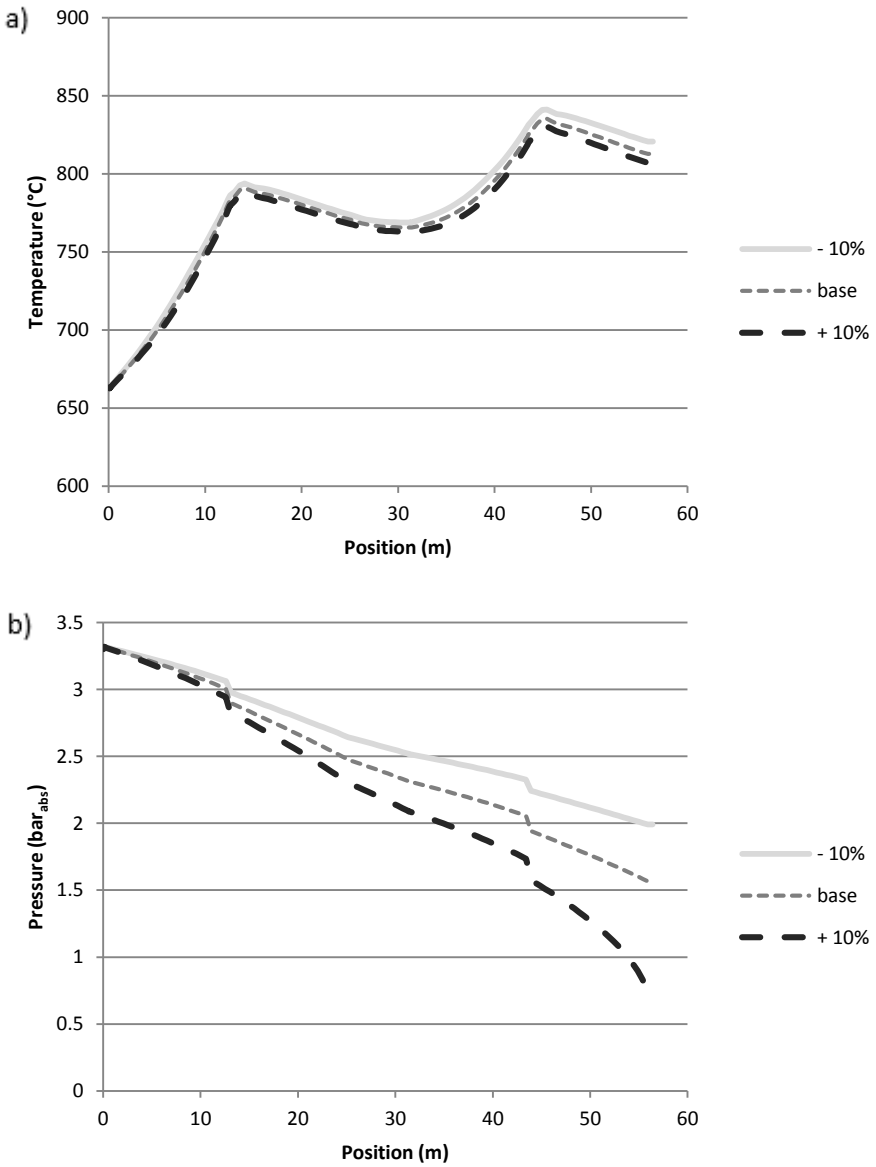

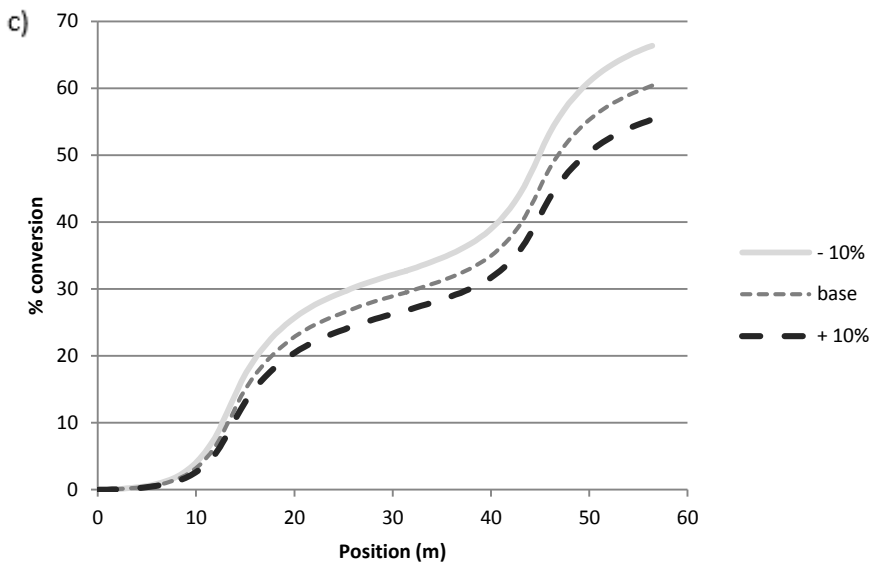

Figure 29 – Model predictions of a) process gas temperature, b) process gas pressure and c) ethane conversion in response to changes in mass flow rate of process gas

Figure 29 shows that the pressure drop profile is influenced the most by a change in the process gas flow rate. A greater pressure drop over the length of the reactor is expected with an increase in mass flow rate and the model responds as expected, with pressure drop increasing with an increase in mass flow rate.

If the rate of heat transfer to the reactor contents were constant then it would be expected that an increase in mass flow rate would result in a decrease in process gas temperature. However, since the rate of heat transfer also depends on the mass flow rate of the process gas the results are harder to anticipate. Figure 29 shows that process-gas temperature profile does decrease slightly with an increase in process gas flow rate. As is expected, with a decrease in process gas temperature along the reactor, the conversion is decreased with an increase in mass flow rate since decreased process temperature causes reactions to proceed at a slower rate and the residence time in the reactor is decreased.

The resulting process gas temperature, pressure and ethane conversion profiles from increasing the absolute process gas temperature by 5% to 889 K (616 °C) and decreasing the absolute inlet process gas temperature by 5% to 983 K (710 °C) are shown in Figure 30.

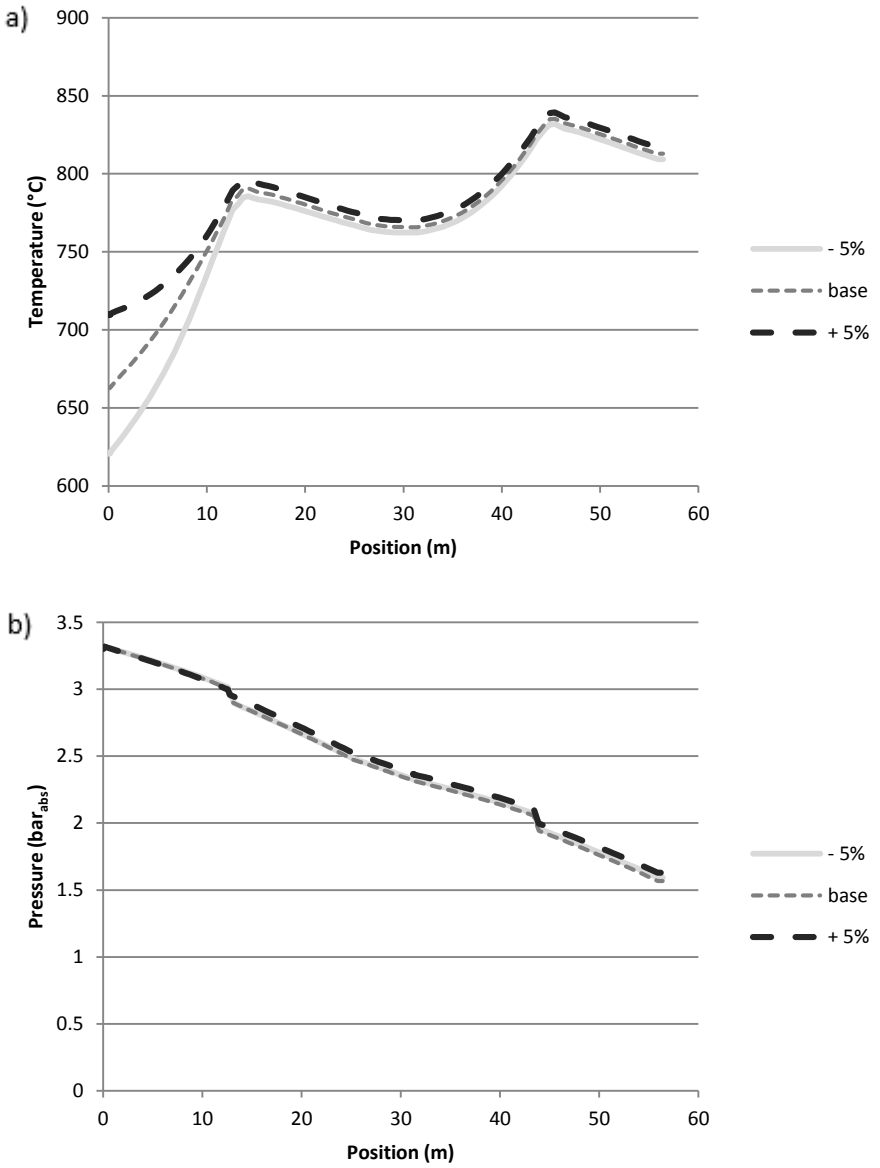

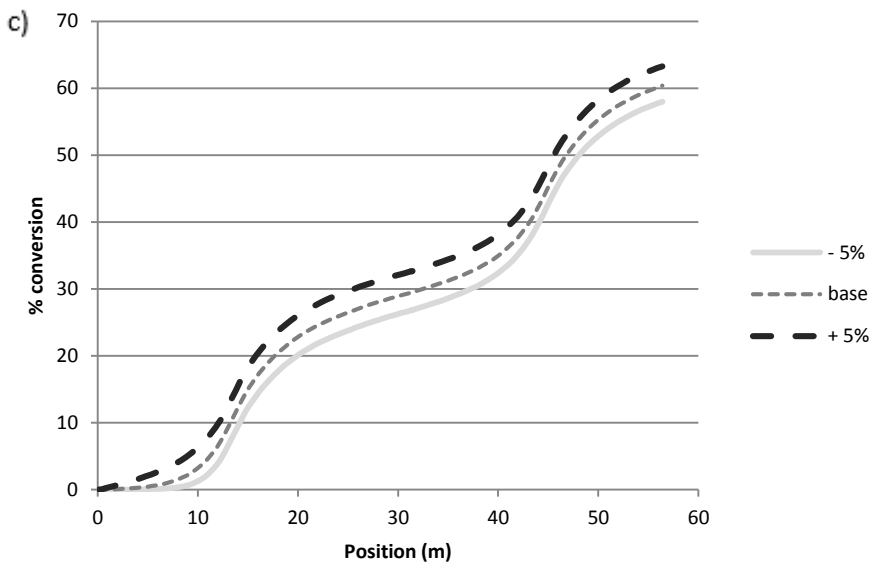

Figure 30 – Model predictions of a) process gas temperature, b) process gas pressure and c) ethane conversion in response to changes in process gas inlet temperature

The process gas temperature profile shows that, although the process gas temperature is different at the inlet, the temperature profiles converge along the length of the reactor. This result corresponds to the conversion profiles that are also shown in Figure 30. With an increase of inlet process-gas temperature, the rate of ethane cracking at the inlet of the tube is higher. Since ethane cracking is endothermic, higher rates lead to greater heat consumption and a slower increase in process gas temperature. The process gas pressure profile is not significantly affected by a change in the inlet process-gas temperature.

Figure 31 shows that the model predicts that an increase or decrease in the steam to ethane mass flow rate ratio by ± 10 % has a minimal effect on the process gas temperature, pressure or ethane conversion profile.

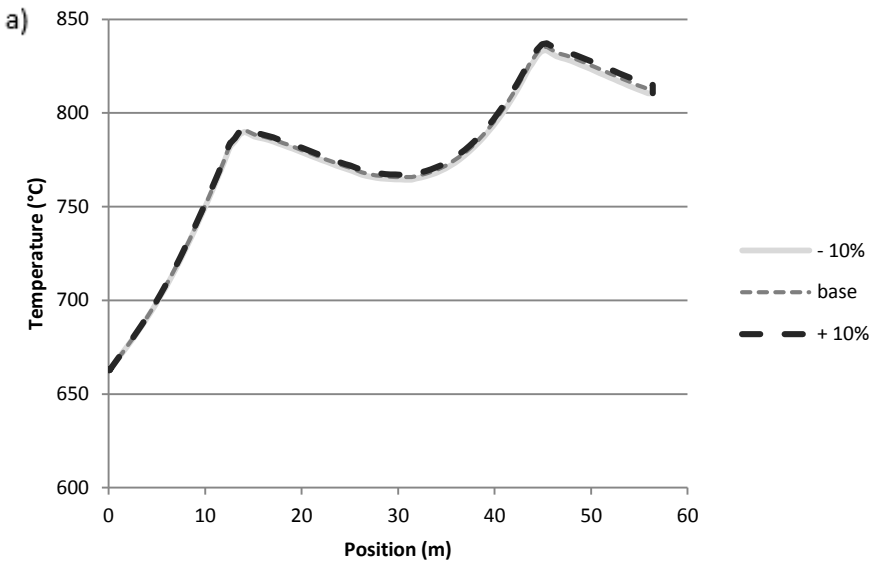
a)
850
800
750
700
650
600
Temperature (°C)
0
10
20
30
40
50
60
Position (m)
- 10%
base
+ 10%

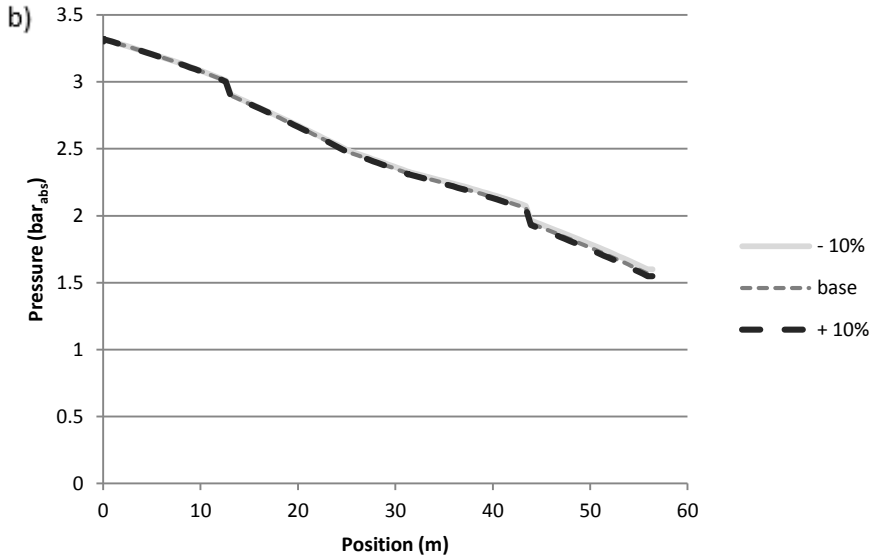
b)
3.5
3
2.5
2
1.5
1
0.5
0
Pressure (bar$_{abs}$)
0
10
20
30
40
50
60
Position (m)
- 10%
base
+ 10%

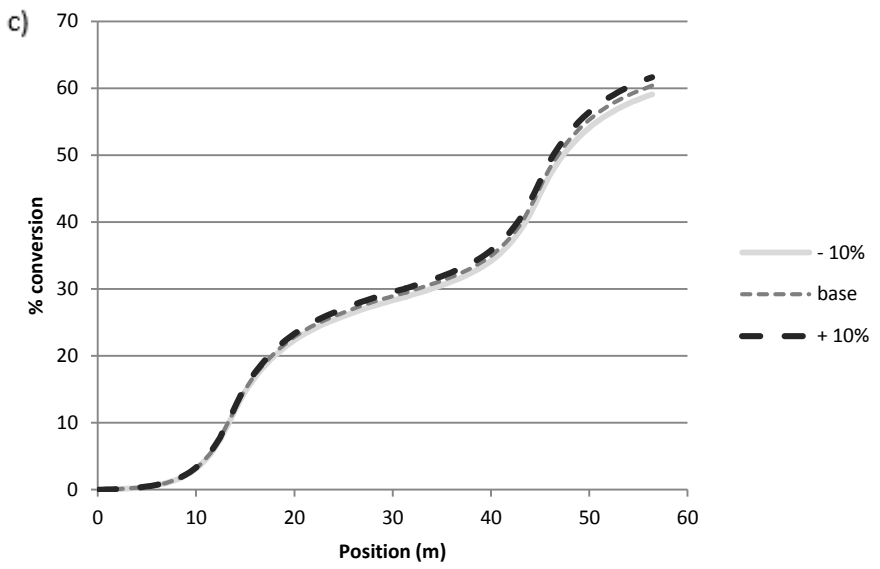

Figure 31 – Model predictions of a) process gas temperature, b) process gas pressure and c) ethane conversion in response to changes in steam to ethane mass flow ratio

Changing the steam to ethane ratio does not change the total mass flow rate through the reactor, and only minimally changes the heat capacity of the reactor contents. Therefore, it is physically reasonable that the process gas temperature and pressure profiles are not significantly affected by a change of 10% in the steam to ethane ratio. The conversion of ethane depends on the process gas temperature and therefore if the process gas temperature profile does not change significantly then the conversion profile should not change significantly either, as seen in Figure 31. There is only a slight increase in conversion with a 10% increase in steam to ethane ratio which also corresponds to the slight increase in process gas temperature. Note that increasing the relative amount of steam to the tubes does not affect the conversion very much, but it does affect the amount of ethylene that is produced per unit time. Increasing the steam to ethane ratio by 10% decreases the amount of ethylene produced per unit time by 5.2%.

In summary, this sensitivity analysis shows that model responses to physical changes in mass flow rate of fuel, mass flow rate of process gas, inlet process gas temperature and

steam-to-ethane mass-flow ratio make physical sense. The current model produces predictions that are fairly similar to SPYRO® predictions and provides a good starting point for future model developments. These future developments will address numerical problems, account for a side-fired furnace configuration and implement steady-state coke-formation mechanisms. The resulting steady-state model will then be extended to a dynamic model that can predict coke build-up over time and cycling between regular operation with coke formation and decoking.

Chapter 6 – Conclusions and recommendations

6.1 Conclusions

A steady-state mathematical model was developed for the radiant section of a floor-fired ethane-pyrolysis furnace. This tubular-reactor model considers 56 pyrolysis reactions involving 28 species plus inert diluent steam. The concentrations of all of the species are tracked along the length of the reactor using 29 material balances. A momentum balance is used to calculate the changes in pressure along the length of the reactor, and an energy balance calculates the process gas temperature profile. Radiant heat transfer to the reactor contents is accounted for using the Roesler flux method with a grey-gas assumption, which simplifies the radiant field into two radiant fluxes in the vertical direction (one upwards and one downwards).

The process-side mathematical model (29 material balances, 1 momentum balance and 1 energy balance) was implemented in PREDICI® as an initial value problem. The concentration of all 29 species, the process gas temperature and process gas pressure are

all known at the inlet of the reactor. Unfortunately, the radiant fluxes and furnace gas temperature are not known at the inlet of the reactor. Trying to solve the radiant flux and furnace gas ODEs as an initial value problem, which is updated via shooting, led to numerical issues.

To avoid this problem, the furnace-side model was solved first (using simplifying assumptions about reactions within the tubes and discretization by finite differences) and then the resulting radiant flux profiles were imposed on the full process-side model in PREDICI®. Initial attempts to solve for the radiant fluxes were conducted in MATLAB®, which was able to solve the resulting algebraic equations with a wide range of parameter values. Unfortunately, solving for the radiant flux profiles in MATLAB® and then manually inserting the results into the full process-side model in PREDICI® is not an attractive approach for future model users.

To make the model more practical for use in an industrial setting, the set of algebraic equations resulting from the discretization of the simplified model was solved directly in PREDICI®. These algebraic equations, which calculate the radiant flux-profiles, are solved in the first 0.075 m of the cold box and then imposed for the rest of the length of the cold box (25.125 m) and in the 0.1 m before the entrance of the hot box and then imposed in the hot box. Solving all of the model equations directly in PREDICI® is a practical approach for future use, but the implementation is not straightforward, making future maintenance or changes to the model more difficult. Furthermore, this approach leads to increased simulation times, and is limited in the range of operating conditions it can simulate without manual intervention.

Model predictions from the proposed model were similar to SPYRO® model predictions and a preliminary investigation of model performance concluded that model predictions respond to changes in i) mass flow rate of fuel, ii) mass flow rate of process gas, iii) inlet process-gas temperature, and iv) steam-to-ethane mass-flow ratio. The process gas temperature, process gas pressure and ethane conversion profiles all respond in a physically expected manner, which indicates that the model is a good starting point for future work.

6.2 Recommendations for future work

To meet the objective of NOVA Chemicals to create a reliable dynamic coke formation model, the following model-development research should be completed:

1. **Implement side-fired furnace geometry**. The current model considered relatively simple floor-fired furnace geometry, but the industrial data that have been collected are for a side-fired furnace. Therefore, to use these data for parameter estimation and model validation, the model must be extended to account for side-fired operation. Unfortunately, early attempts to model side-fired furnaces were unsuccessful. A description of these attempts and ideas for future attempts are given in Appendix F. Note that NOVA Chemicals operates both floor-fired and side-fired cracking furnaces and would like the model to handle both types of geometry.
2. **Improve the range of operating conditions that PREDICI® can accept as model inputs, without manual intervention**. Numerical errors were encountered in PREDICI® when changes as small as 10% were made to key model inputs such as inlet absolute temperature of the process gas. These numerical errors have to do with the quality of initial guesses and the way that PREDICI® is used to solve the system

of algebraic equations. Future work should resolve these issues before parameter estimation is attempted. The resolution of numerical issues may require support from the software developer Dr. Michael Wulkow, who was extremely helpful in the research presented in this thesis.

3. **Add coke formation mechanisms.** Coke formation mechanisms were discussed in section 2.2, however, they were not implemented in this initial ethane pyrolysis model. Only coke formation rates will be determined in the steady-state model, future dynamic models will account for build-up of a coke layer over time.
4. **Perform parameter estimation on steady-state, side-fired, coke-free model.** The steady-state model should be tuned to better match operating data available for a coke-free, side-fired furnace. PREDICI® has built-in parameter estimation capabilities and an estimability analysis[53] and model selection criterion[54] can be used to determine which parameters should be estimated. Model adjustments to reduce simulation times should be investigated to reduce the required time for parameter estimation.
5. **Couple radiant section model with models for the convection section and downstream heat exchangers (USX and TLE).** The model presented in this thesis considers only the radiant section of an ethane pyrolysis furnace. However, NOVA Chemicals would like a model that includes all sections of the ethane pyrolysis unit. Models for the convection section, the USX and the TLE have been developed by NOVA Chemicals and implemented in PREDICI®, so all of these models can be combined.

6. **Extend steady-state model to account for dynamic operation.** The key objective for NOVA Chemicals is to have a dynamic model that can accurately predict coke formation over time. Once the steady-state model has been improved and tuned (based on previous recommendations) it can be extended to dynamic operation. The residence time of the process gas in the furnace is very small relative to the time over which coke builds up on the tube walls. Therefore, it is recommended that a series of steady-state models (ODEs in x) are used to simulate dynamic operation and then update the thickness of the coke layer over time, rather than deriving and implementing a dynamic model (PDEs) in PREDICI®. Michael Wulkow should be consulted to discuss the various options that might be available.
7. **Tune coke-formation mechanisms and kinetics using dynamic industrial data.** Currently, there is a lack of available literature on the kinetics of coke formation. Therefore, it can be expected that the coke-formation mechanisms and kinetic data implemented in the steady-state model and used in the proposed dynamic model will need significant tuning for model predictions to match industrial operating data.
8. **Add decoke cycles to dynamic operation.** Part of the dynamic operation of an ethane pyrolysis furnace is alternating between normal pyrolysis operation and decoking operation. NOVA Chemicals would like their dynamic model to be able to simulate both operational states and the transition between the two.

References

1. K. M. Sundaram, G. F. Froment, *Chem. Eng. Sci.* **1976**, *32*, 601.

2. M. E. Masoumi, S. M. Sadrameli, J. Towfighi, A. Niaei, *Energy* **2006**, *31*, 516.

3. D. W. Brunett, G. E. Totten, P. M. Matlock, *Fuel Lubr. Handb. Technol.* **2009**.

4. L. F. Albright, J. C. Marek, *Ind. Eng. Chem. Res.* **1988**, *27*, 751.

5. E. Schools, G. Froment, *AIChE J.* **1997**, *43*, 118.

6. A. Mohamadalizadeh, J. Towfighi, R. Karimzadeh, *J. Anal. Appl. Pyrolysis* **2008**, *82*, 134.

7. G. J. Heynderickx, E. M. Schools, G. B. Marin, *Ind. Eng. Chem. Res.* **2006**, *45*, 7520.

8. H. Cai, A. Krzywicki, M. C. Oballa, *Chem. Eng. Process. Process Intensif.* **2002**, *41*, 199.

9. P. Ranjan, P. Kannan, A. Al Shoaibi, C. Srinivasakannan, *Chem. Eng. Technol.* **2012**, *35*, 1093.

10. M. Dente, E. Ranzi, A. Goossens, *Comput. Chem. Eng.* **1979**, *3*, 61.

11. K. M. Sundaram, G. F. Froment, *Ind. Eng. Chem. Fundam.* **1978**, *17*, 174.

12. T. Kunugi, T. Sakai, *Ind. Eng. Chem. Fundam.* **1969**, *8*, 374.

13. M. Lin, M. Back, *Can. J. Chem.* **1966**, *44*, 2369.

14. K. Yang, *J. Am. Chem. Soc.* **1962**, *719*, 91.

15. M. J. Kurylo, N. C. Peterson, W. Braun, *J. Chem. Phys.* **1970**, *53*, 2776.

16. R. Hiatt, S. Benson, *J. Am. Chem. Soc.* **1972**, *94*, 25.

17. A. Lalonde, S. Price, *Can. J. Chem.* **1971**, *49*, 3367.

18. Technip, **2005**, at <http://www.technip.com/sites/default/files/technip/page/attachments/SPYRO_descr.pdf>.

19. G. C. Reyniers, G. F. Froment, F. D. Kopinke, G. Zimmermann, *Ind. Eng. Chem. Res.* **1994**, *33*, 2584.

20. F. Kopinke, G. Zimmermann, S. Nowak, *Carbon N. Y.* **1988**, *26*, 117.

21. K. M. Sundaram, G. F. Froment, *Chem. Eng. Sci.* **1978**, *34*, 635.

22. L. F. Albright, J. C. Marek, *Ind. Eng. Chem. …* **1988**, *27*, 743.

23. K. M. Sundaram, P. S. VanDamme, G. F. Froment, *AIChE J.* **1981**, *27*, 946.

24. P. Kumar, D. Kunzru, *Can. J. Chem. Eng.* **1985**, *63*, 598.

25. P. Kumar, D. Kunzru, *Can. J. Chem. Eng.* **1987**, *65*, 280.

26. F. Kopinke, G. Zimmermann, *Ind. …* **1993**, *32*, 56.

27. R. Zou, Q. Lou, S. Mo, S. Feng, *Ind. Eng. Chem. …* **1993**, *32*, 843.

28. L. F. Albright, J. C. Marek, *Ind. Eng. Chem. Res.* **1988**, *27*, 755.

29. J. Towfighi, J. Modarres, M. Omidkhah, *Int. J. Eng.* **2004**, *17*, 319.

30. K. Sundaram, G. Froment, *Chem. Eng. Sci.* **1979**, *34*, 635.

31. F. Liu, H. A. Becker, Y. Bindar, *Int. J. Heat Mass Transf.* **1998**, *41*, 3357.

32. F. Farhadi, M. Bahrami Babaheidari, M. M. Y. Motamed Hashemi, *Appl. Therm. Eng.* **2005**, *25*, 2398.

33. X. Lan, J. Gao, C. Xu, H. Zhang, *Chem. Eng. Res. Des.* **2007**, *85*, 1565.

34. G. J. Heynderickx, G. F. Froment, *Ind. Eng. Chem. …* **1998**, *5885*, 914.

35. M. V. Ramana Rao, P. M. Plehiers, G. F. Froment, *Chem. Eng. Sci.* **1988**, *43*, 1223.

36. F. C. Roesler, *Chem. Eng. Sci.* **1967**, *22*, 1325.

37. A. Schuster, *Astrophys. J.* **1905**, *21*, 1.

38. K. Schwarzschild, *Nachr. Akad. Wiss. Göttingen, Math.-phys.* **1906**, *195*, 41.

39. M. Jakob, *Proc. Phys. Soc.* **1946**, *59*, 726.

40. R. G. Siddall, N. Selçuk, *Heat Transf. Flames* **1974**.

41. C. V. S. Murty, M. V. K. Murthy, *Ind. Eng. Chem. Res.* **1988**, *27*, 1832.

42. N. Selçuk, R. Siddall, J. Beer, *Chem. Eng. Sci.* **1975**, *30*, 871.

43. M. A. Soliman, S. El-Nashaie, *Chem. Eng. Sci.* **1988**, *43*, 1801.

44. D. A. Latham, K. B. McAuley, B. A. Peppley, T. M. Raybold, *Fuel Process. Technol.* **2011**, *92*, 1574.

45. B. Olayiwola, **2012**.

46. M. W. M. van Goethem *et al.*, *Chem. Eng. Res. Des.* **2013**, *91*, 1106.

47. M. Yan, **2000**, 1.

48. W. M. Rohsenow, J. P. Hartnett, Y. I. Cho, **1998**, 7.81.

49. J. Nemeth, G. Bucsky, *Hungarian J. Ind. Chem.* **1997**, *25*, 91.

50. M. Vasudevaiah, R. Patturaj, *Int. J. Math. Math. Sci.* **1994**, *17*, 553.

51. M. Wulkow, **2008**.

52. P. Armitage, J. De La Cal, J. Asua, *J. Appl. Polym. …* **1994**, *51*, 1985.

53. D. E. Thompson, K. B. McAuley, P. J. McLellan, *Macromol. React. Eng.* **2009**, *3*, 160.

54. S. Wu, K. B. McAuley, T. J. Harris, *Can. J. Chem. Eng.* **2011**, *89*, 325.

55. VDI-Waermeatlas, **2006**, *10*.

Appendix A Radiative heat transfer

The Roesler flux method accounts for a radiation field with a net flux in the vertical direction by considering radiation in two directions (up and down) and two colours (band and window). Band radiation is made up of all of the wavelengths that can be absorbed by the gas, whereas window radiation is all of the wavelengths that will always pass through the gas unaffected.[36] The two directions and two colours give a total of four radiation streams to be considered, whose changes in intensity can be represented by ODEs:

i. $A(z)$ – window radiation flux in the positive z direction (upward) in $kW \cdot m^{-2}$
ii. $B(z)$ – window radiation flux in the negative z direction (downward) in $kW \cdot m^{-2}$
iii. $F(z)$ – band radiation flux in the positive z direction (upward) in $kW \cdot m^{-2}$
iv. $G(z)$ – band radiation flux in the negative z direction (downward) in $kW \cdot m^{-2}$

Figure 32 shows the absorption and emission of upward band radiation that needs to be considered as it passes through a volume of gas with a height Δz.

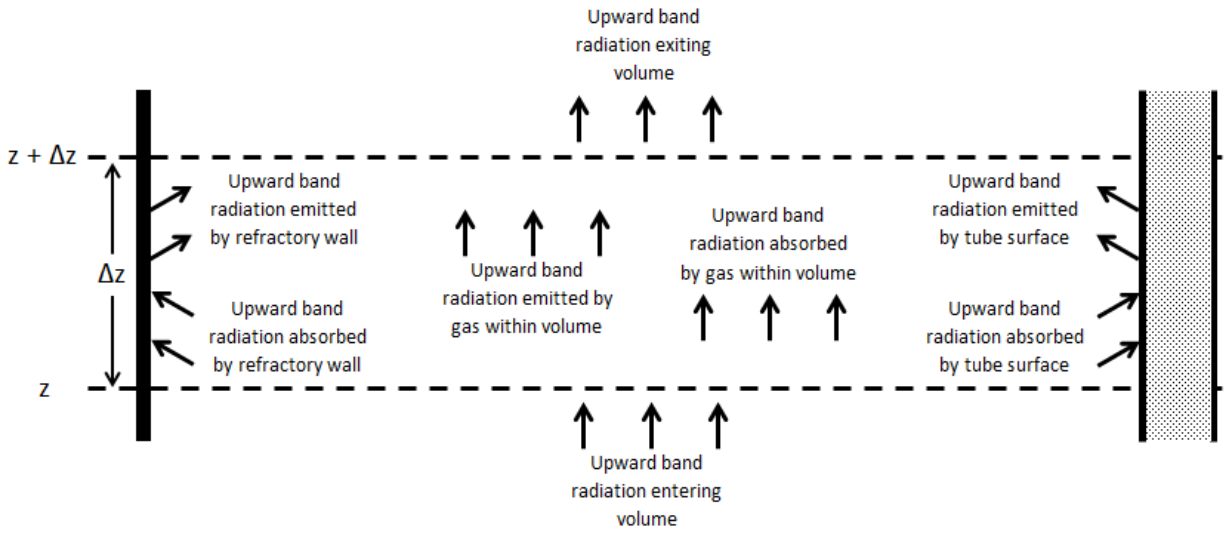

Figure 32 – Upward band radiation passing through and being absorbed and emitted within a volume of gas with height Δz

A balance (in kW) can be performed on the upward band radiation over the height Δz.

Accumulation	=	upward band radiation in at z (1)	-	upward band radiation out at $z + \Delta z$ (2)	+	upward band radiation generated by gas in the volume (3)	-	upward band radiation absorbed by gas in the volume (4)
	+	upward band radiation emitted by tube walls in the height Δz (5)	-	upward band radiation absorbed by tube walls in the height Δz (6)	+	upward band radiation emitted by refractory walls in the height Δz (7)	-	upward band radiation absorbed by refractory walls in the height Δz (8)

53

The amount of upward band radiation absorbed by the gas (in the fourth term) can be calculated as a fraction of the incoming upward band radiation. A volumetric absorption coefficient β is the fraction of band radiation absorbed along a unit of vertical length so that the rate of absorption of upward band radiation by the gas is equal to $\beta F A_c \Delta z$ where A_c is the constant cross-sectional area, and β has units of m^{-1}.[36] The parameter β takes into account the ability of the gas to absorb radiation, and also accounts for the fact that

the upward radiation enters the volume element at different directions. To obtain the third term in equation 53, consider that the emission of radiation (in both directions) per unit volume of gas is $4\varepsilon'\sigma {T_f}^4$ according to the Koenigsberger equation[39] where:

$$\varepsilon' = \frac{\tau\beta}{2} \qquad \textbf{54}$$

and τ is the fraction of radiation that is emitted as band radiation (as opposed to window radiation). Half of the energy radiated by a volume element will be radiated in the upward direction and half of the energy will be radiated in the downward direction, so the rate of emission of band radiation in the upward direction is $\tau\beta\sigma {T_f}^4 A_c \Delta z$[36].

With these terms, energy balance 53 can be updated to:

0 =	$F_z A_c$ (1)	-	$F_{z+\Delta z} A_c$ (2)	+	$\tau\beta\sigma {T_f}^4 A_c \Delta z$ (3)	-	$\beta F A_c \Delta z$ (4)		
+	upward band radiation emitted by tube walls in the height Δz (5)	-	upward band radiation absorbed by tube walls in the height Δz (6)	+	upward band radiation emitted by refractory walls in the height Δz (7)	-	upward band radiation absorbed by refractory walls in the height Δz (8)		**55**

The upward band radiation that is absorbed by the tube walls over the height Δz (term 6) can also be described as a fraction of the incoming upward band radiation as $\gamma_t F A_c$ where γ_t is an unknown coefficient that will be determined below. The fifth term in equation 53 is the rate of upward band radiation emitted by the tube walls and must follow the Stefan-Boltzmann law.[36] Half of the emitted band radiation will be in the positive direction and half will be in the negative direction so the amount of band radiation emitted in the upward direction per unit surface area of tube is:

$$\frac{\tau \varepsilon_t \sigma {T_{to}}^4}{2} \quad \textbf{56}$$

For the balance on the small volume of gas with height Δz, the rate of emission of upward band radiation from the tube surfaces (in kW) is:

$$\frac{\tau \varepsilon_t A_t \sigma {T_{to}}^4}{2} A_c \Delta z \quad \textbf{57}$$

where A_t is the tube surface area per unit volume of gas.[36]

Since the coefficient γ_t only depends on the gas, the geometry and the tube surface material, it can be shown that the unknown coefficient $\gamma_t = \varepsilon_t A_t \Delta z/2$ by examining a simpler case at a uniform temperature *T*, where there is no change in the upward (or downward) band radiation over the height Δz. In this simple situation, all of the upward band radiation absorbed by the surface is emitted as upward and downward band radiation as shown in Figure 33. Similarly, the downward band radiation (which equals the upward band radiation) that is absorbed by the surface is emitted by the surface as upward and downward band radiation. Furthermore, the upward and downward band radiation that is absorbed by the gas is emitted by the gas.

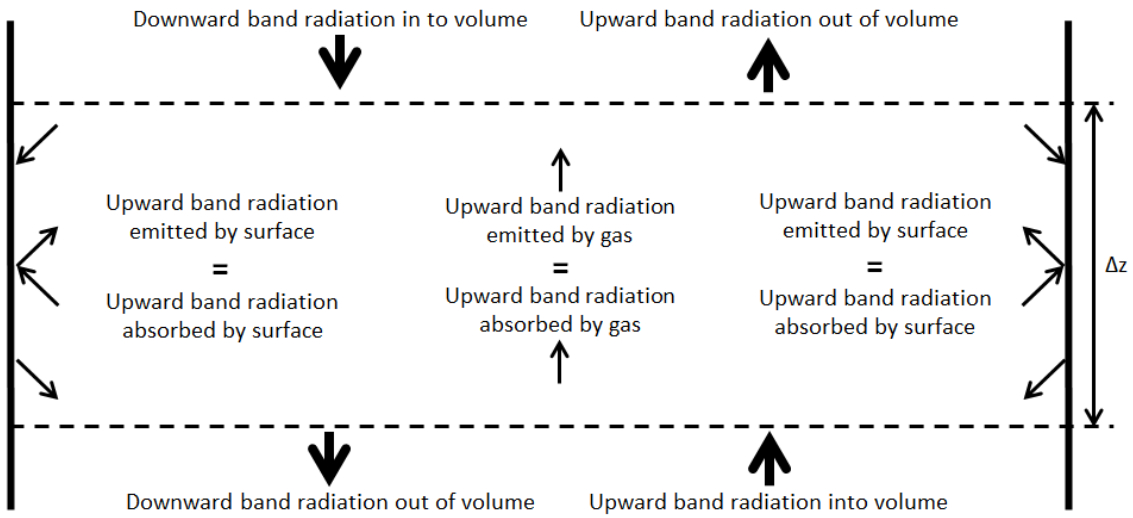

Figure 33 – Simple case where all upward band radiation that is absorbed is emitted as upward band radiation

Since the upward band radiation absorbed by the gas is equal to the upward band radiation emitted by the gas then:

$$\beta F A_c \Delta z = \tau \beta \sigma T^4 A_c \Delta z \qquad \textbf{58}$$

and therefore:

$$F = \tau \sigma T^4 \qquad \textbf{59}$$

in this simple system. Also, since the upward band radiation absorbed by the surface is equal to the upward band radiation emitted by surface then:

$$\gamma_t F A_c = \frac{\tau \varepsilon_t A_t \sigma T^4}{2} A_c \Delta z \qquad \textbf{60}$$

and equation 59 can be substituted into equation 60 to show that:

$$\gamma_t = \frac{\varepsilon_t A_t}{2} \Delta z \qquad \textbf{61}$$

Since this is true for the simple system, it is also true for the more complex system in Figure 32 because γ and A_t are properties of the gas and the geometry of the system. Therefore the balance on the upward band radiation initially presented in equation 53 will be:

$$0 = F_z A_c - F_{z+\Delta z} A_c + \beta\tau\sigma {T_f}^4 A_c \Delta z - \beta F A_c \Delta z + \frac{\varepsilon_t A_t \tau\sigma {T_{to}}^4}{2} A_c \Delta z - \frac{\varepsilon_t A_t F}{2} A_c \Delta z + \begin{matrix}\text{upward band}\\ \text{radiation emitted by}\\ \text{refractory walls}\end{matrix} - \begin{matrix}\text{upward band}\\ \text{radiation absorbed}\\ \text{by refractory walls}\end{matrix} \quad (62)$$

The derivation of the terms associated with the refractory wall is approached differently than the terms associated with the tube surface so that the temperature of the refractory wall will not need to be calculated. It is assumed that the refractory walls are both grey and radiatively adiabatic. Any radiation that is absorbed by the refractory wall will be re-emitted as band or window radiation, half in the positive *z* direction and half in the negative *z* direction. Figure 34 depicts how incident radiation interacts with the refractory wall, using an upward beam of incident band radiation as an example.

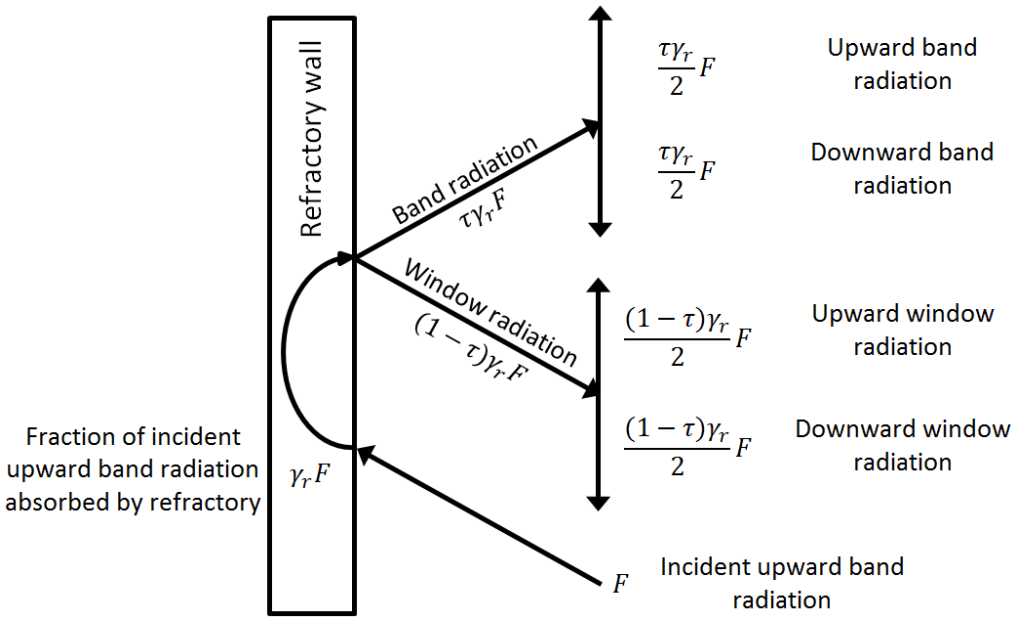

Figure 34 – Interaction of band and window radiation with refractory wall

Figure 34 shows the upward band radiation that is absorbed by the refractory wall. This radiation is then emitted by the refractory. Some will be emitted as band radiation and some will be emitted as window radiation. Half will be emitted in the positive direction and half in the negative direction.[36] Note that downward band radiation (not shown in

Figure 34), will also be absorbed and then emitted in a similar fashion (some band, some window, half up and half down). Furthermore window radiation (not shown in Figure 34) coming from both directions will be absorbed and emitted as band and window radiation in both directions.

Therefore the terms in equation 53 that account for the upward band radiation that is absorbed and emitted by the refractory wall are:

Fraction of upward band radiation absorbed and re-emitted as upward band radiation	+	Fraction of downward band radiation absorbed and re-emitted as upward band radiation	+	Fraction of upward window radiation absorbed and re-emitted as upward band radiation	+	Fraction of downward window radiation absorbed and re-emitted as upward band radiation	-	Fraction of upward band radiation absorbed	**63**
(7.1)		(7.2)		(7.3)		(7.4)		(8.1)	
$\frac{\tau\gamma_r}{2}FA_c$	+	$\frac{\tau\gamma_r}{2}GA_c$	+	$\frac{\tau\gamma_r}{2}AA_c$	+	$\frac{\tau\gamma_r}{2}BA_c$	-	$\gamma_r FA_c$	
(7.1)		(7.2)		(7.3)		(7.4)		(8.1)	

where γ_r is an unknown coefficient. It can be shown that $\gamma_r = \varepsilon_r A_r \Delta z/2$ where A_r is the refractory surface area per unit volume of furnace gas by once again considering the simpler case presented in Figure 33, where $F = \tau\sigma T^4$ as shown in equation 59. The absorption of upward band radiation can be expressed as:

$$\gamma_r F A_c \quad \textbf{64}$$

as shown in term 8.1 of equation 63. The rate of emission of band radiation per unit area of surface follows the Stefan-Boltzmann law. Half of the band radiation will be emitted in the positive direction, and half will be emitted in the negative direction as in equation 56. The rate of emission of upward band radiation in this simple case can be written as:

$$\frac{\tau\varepsilon_r\sigma T^4 A_r}{2} A_c \Delta z \quad \textbf{65}$$

where A_r is the surface area per unit volume. Since the absorption of upward band radiation from the surface will be equal to the emission of upward band radiation in this simple case:

$$\gamma_r F A_c = \frac{\tau\varepsilon_r\sigma T^4 A_r}{2} A_c \Delta z \quad \textbf{66}$$

and with the substitution of the expression for *F* in the simple case:

$$\gamma_r = \frac{\varepsilon_r A_r}{2} \Delta z \quad \textbf{67}$$

Again, γ_r is a property of the gas and the system geometry so that equation 67, which was derived for the simple case, will also be valid for the more complex system shown in Figure 32.

With the addition of the refractory wall terms, equation 53 becomes:

$$0 = F_z A_c - F_{z+\Delta z} A_c + \beta\tau\sigma {T_f}^4 A_c \Delta z - \beta F A_c \Delta z + \frac{\varepsilon_t A_t \tau\sigma {T_{to}}^4}{2} A_c \Delta z - \frac{\varepsilon_t A_t F}{2} A_c \Delta z + \frac{\tau\varepsilon_r A_r}{4} (F + G + A + B) A_c \Delta z - \frac{\varepsilon_r A_r F}{2} A_c \Delta z \quad \textbf{68}$$

When Δz approaches zero the total steady-state energy balance on the upward band radiation will become the ODE:

$$\frac{dF}{dz} = \beta\sigma\tau {T_f}^4 - \left(\beta + \frac{\varepsilon_t A_t + \varepsilon_r A_r}{2}\right) F + \frac{\tau\varepsilon_r A_r}{4} (F + G + A + B) + \frac{\varepsilon_t A_t \sigma\tau {T_{to}}^4}{2} \quad \textbf{69}$$

where *F* is upward band radiation per unit cross sectional area (in $kW \cdot m^{-2}$).

Following a similar derivation, the ODEs for the other radiation streams can be determined:

$$-\frac{dG}{dz} = \beta\sigma\tau {T_f}^4 - \left(\beta + \frac{\varepsilon_t A_t + \varepsilon_r A_r}{2}\right) G + \frac{\tau\varepsilon_r A_r}{4}(F + G + A + B) + \frac{\varepsilon_t A_t \sigma\tau {T_{to}}^4}{2} \quad \textbf{70}$$

$$\frac{dA}{dz} = \frac{(1-\tau)\varepsilon_r A_r}{4}(F + G + A + B) - \left(\frac{\varepsilon_t A_t + \varepsilon_r A_r}{2}\right) A + \frac{\varepsilon_t A_t \sigma(1-\tau) {T_{to}}^4}{2} \quad \textbf{71}$$

$$-\frac{dB}{dz} = \frac{(1-\tau)\varepsilon_r A_r}{4}(F + G + A + B) - \left(\frac{\varepsilon_t A_t + \varepsilon_r A_r}{2}\right) B + \frac{\varepsilon_t A_t \sigma(1-\tau) {T_{to}}^4}{2} \quad \textbf{72}$$

It can be noted that the terms for window radiation do not include absorption or emission by the furnace gas. Window radiation cannot be absorbed by the furnace gas so only interaction with the tube walls and the refractory are considered.

When Siddall and Selcuk[40] applied the Roesler two-flux method to a process gas heater, they added a grey-gas assumption. That is, the emission of soot associated with luminous flames effectively covers the window regions of the gas radiation spectrum and therefore all radiation can be considered as band radiation.[41] As a result, the entire radiative field can be accounted for by two fluxes, one in the positive direction q^+ and one in the negative direction q^-. A balance (in kW) on the upward radiation in a volume element with a height Δz will be:

Accumulation	=	upward radiation in at z	-	upward radiation out at $z + \Delta z$	+	upward radiation emitted by gas in volume	-	upward radiation absorbed by gas in volume
	+	upward radiation emitted by tube walls in height Δz	-	upward radiation absorbed by tube walls in height Δz	+	upward radiation emitted by refractory walls in height Δz	-	upward radiation absorbed by refractory walls in height Δz

By assuming no window radiation, the variable τ, which accounts for the fraction of radiation that is emitted as band radiation will always be equal to one. Therefore the total rate of radiation emitted by the gas in the upward direction will be $\beta\sigma {T_f}^4 A_c \Delta z$ and the

rate of absorption will be $\beta q^{+} A_c \Delta z$. The amount of upward radiation emitted by the tube walls will be half of the total emission by the tube walls according to the Stefan-Boltzmann law $\frac{\varepsilon_t A_t \sigma {T_{to}}^4}{2} A_c \Delta z$ and the absorption term will follow the same form derived above as $\frac{\varepsilon_t A_t}{2} q^{+} A_c \Delta z$.

Figure 35 shows the interaction of both the upwards and downwards radiation with the refractory wall.

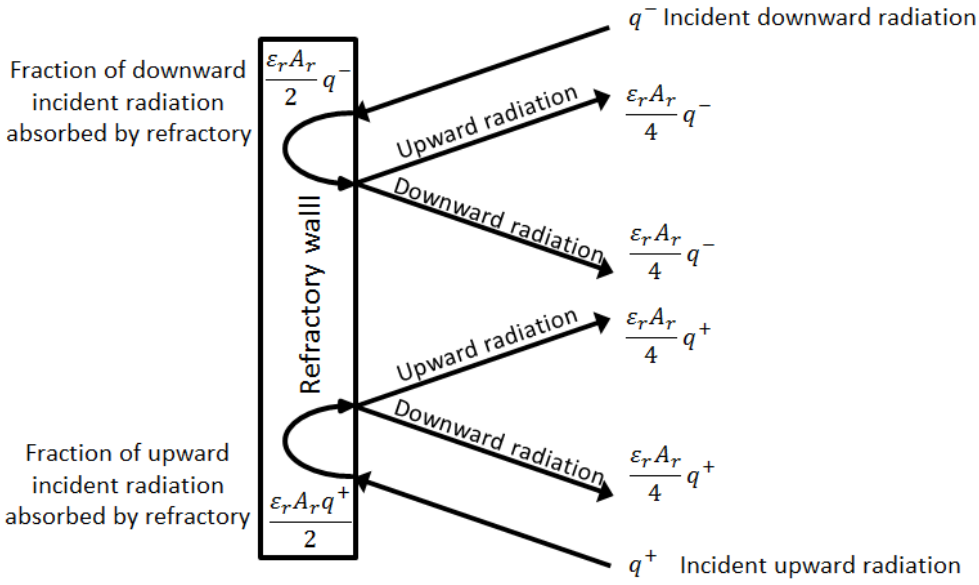

Figure 35 – Interaction of radiation with refractory wall

By showing both the upward and downward incident radiation beams it can be seen that the change in upward radiation will be equal to the emitted upward radiation minus the absorbed upward radiation. Since half of the radiation is emitted in the negative direction, and half is emitted in the positive direction, the radiation emitted by the refractory wall in the positive direction will simply be half of the absorbed upward radiation $\frac{\varepsilon_r A_r}{4} q^{+} A_c \Delta z$

plus half of the absorbed downward radiation $\frac{\varepsilon_r A_r}{4} q^- A_c \Delta z$. The absorption term will be $\frac{\varepsilon_r A_r}{2} q^+ A_c \Delta z$ as shown in Figure 35.

By combining these terms and letting the height Δz approach zero the ODE describing the change in the radiant flux in the upward direction with position is:

$$\frac{dq^+}{dz} = \beta\sigma {T_f}^4 + \frac{\varepsilon_t A_t \sigma {T_{to}}^4}{2} - \left(\beta + \frac{\varepsilon_r A_r}{4} + \frac{\varepsilon_t A_t}{2}\right) q^+ + \frac{\varepsilon_r A_r}{4} q^- \quad \textbf{73}$$

Following a similar derivation an equation for the radiant flux in the negative direction can be determined:

$$-\frac{dq^-}{dz} = \beta\sigma {T_f}^4 + \frac{\varepsilon_t A_t \sigma {T_{to}}^4}{2} + \frac{\varepsilon_r A_r}{4} q^+ - \left(\beta + \frac{\varepsilon_r A_r}{4} + \frac{\varepsilon_t A_t}{2}\right) q^- \quad \textbf{74}$$

The steam-naptha reformer discussed in Roesler's work included only single pass process tubes and therefore the tube wall temperature of each tube was assumed to be the same at each position *z*. The process gas heater presented by Siddall and Selcuk however, described multi-pass tubes where the tube walls will have different surface temperatures at different *z* positions. To account for the difference in tube wall temperatures between passes, Siddall and Selcuk used the average radiant emission terms of all tubes at a given position *z*, with different tube wall temperatures $T_{to,i}$. With this addition to equations 73 and 74 take following form:

$$\frac{dq^+}{dz} = \beta\sigma {T_f}^4 + \frac{\varepsilon_t A_t \sigma}{2} \frac{\sum_{i=1}^{n_p} {T_{to,i}}^4}{n_p} - \left(\beta + \frac{\varepsilon_r A_r}{4} + \frac{\varepsilon_t A_t}{2}\right) q^+ + \frac{\varepsilon_r A_r}{4} q^- \quad \textbf{75}$$

$$-\frac{dq^-}{dz} = \beta\sigma {T_f}^4 + \frac{\varepsilon_t A_t \sigma}{2} \frac{\sum_{i=1}^{n_p} {T_{to,i}}^4}{n_p} + \frac{\varepsilon_r A_r}{4} q^+ - \left(\beta + \frac{\varepsilon_r A_r}{4} + \frac{\varepsilon_t A_t}{2}\right) q^- \quad \textbf{76}$$

where n_p refers to the number of tube passes.

Appendix B Species properties

Table 17 – Heat capacity coefficients for equation 7.10[55]

Species	$A_{C_{p.i}}$	$B_{C_{p.i}}$ (x 10^3)	$C_{C_{p.i}}$ (x 10^6)	$D_{C_{p.i}}$ (x 10^{11})
O_2	0.8061	0.4164	-0.1586	2.10
N_2	0.9334	0.3056	-0.0779	0.618
CO_2	0.6173	0.9500	-0.388	5.00
H_2	13.937	1.256	-0.8920	66.0
H_2O	1.5267	0.9645	-0.1873	1.45
CH_4	1.2825	2.828	1.3080	-87.9
C_2H_2	0.7835	3.816	-2.837	84.3
C_2H_4	0.4167	4.215	-1.200	-4.50
C_2H_6	0.2384	5.630	-1.926	14.2
C_3H_4	0.3209	4.639	-2.602	56.9
C_3H_6	0.3043	4.585	-1.398	-3.80
C_3H_8	0.2031	5.628	-2.004	14.7
C_4H_6	-0.0916	6.491	-4.181	100
C_4H_8	0.1867	5.213	-2.169	27.5
C_4H_{10}	0.2695	5.496	-1.992	15.3
cyC_5H_6	-0.6247	7.400	-5.000	200
cyC_5H_{10}	-0.6433	7.233	-3.724	69.4
C_5H_{12}	-0.0158	6.569	-3.255	60.7
C_6H_{10}	-0.4169	6.601	-3.489	67.2

Table 18 – Conductivity polynomial coefficients for equation 7.15

Species	A_{λ_i} (x 10^8)	B_{λ_i} (x 10^5)	C_{λ_i} (x 10^2)
H_2	-6.5974	47.258	4.5217
H_2O	3.0933	7.1725	- 0.6255
CH_4	1.3287	16.291	- 1.7395
C_2H_2	-0.4323	10.963	- 0.9651
C_2H_4	2.0211	15.200	- 2.9343
C_2H_6	5.4595	12.471	-2.226
C_3H_4	0.1714	11.166	- 1.8109
C_3H_6	4.3567	10.070	- 1.7693
C_3H_8	6.9461	9.2939	- 1.7518
C_4H_6	0.5101	10.475	- 1.9261
C_4H_8	4.7676	8.8634	- 1.6691
C_4H_{10}	5.5097	10.311	- 2.1303
cyC_5H_6	9.9373	5.8845	- 1.5466
cyC_5H_{10}	0.5994	12.193	- 2.6941
C_5H_{12}	7.9465	5.6496	- 0.9965
C_6H_{10}	3.3188	8.1793	- 1.4419

*Generated in ASPEN Plus® using ideal gas law

Table 19 – Viscosity polynomial coefficients for equation 7.8

Species	A_{μ_i} (x 10^{12})	B_{μ_i} (x 10^{8})	C_{μ_i} (x 10^{7})
H_2	-3.358	2.0646	31.592
H_2O	3.001	3.5967	12.742
CH_4	-6.055	3.1621	25.597
C_2H_2	-2.100	3.0245	17.100
C_2H_4	-7.423	3.3785	10.470
C_2H_6	-4.546	2.9244	12.231
C_3H_4	-5.106	2.5153	14.149
C_3H_6	-5.596	3.0181	2.9810
C_3H_8	-1.405	2.5251	9.7989
C_4H_6	-4.734	2.3456	10.393
C_4H_8	-5.004	2.8519	-1.7233
C_4H_{10}	-0.757	2.3973	4.8542
cyC_5H_6	-5.045	2.8549	1.4487
cyC_5H_{10}	-3.861	2.5428	4.2216
C_5H_{12}	-1.891	2.2758	4.1134
C_6H_{10}	-4.971	2.6472	-2.3040

*Generated in ASPEN Plus® using ideal gas law

Appendix C Example of MATLAB® code for a 6-section discretized model

The system of 229 algebraic equations resulting from the 6-section discretization of the simplified model was solved in MATLAB® using the *fsolve* function. The *fsolve* function takes a *.fun* file and a 1 x 229 matrix of initial guesses for the 229 unknowns as inputs, and outputs a 1 x 229 matrix of solutions. The code for the *.fun* file required to solve the system of 229 algebraic equations and 229 unknowns is provided.

```
function fcns = eqns6(z)

Tf1 = z(1);
Tf2 = z(2);
Tf3 = z(3);
Tf4 = z(4);
Tf5 = z(5);
Tf6 = z(6);
Tg1 = z(7);
Tg2 = z(8);
Tg3 = z(9);
Tg4 = z(10);
Tg5 = z(11);
Tg6 = z(12);
qp0 = z(13);
qp1 = z(14);
qp2 = z(15);
qp3 = z(16);
qp4 = z(17);
qp5 = z(18);
qp6 = z(19);
qn0 = z(20);
```

```
qn1 = z(21);
qn2 = z(22);
qn3 = z(23);
qn4 = z(24);
qn5 = z(25);
qn6 = z(26);
Tto0 = z(27);
Tto1 = z(28);
Tto2 = z(29);
Tto3 = z(30);
Tto4 = z(31);
Tto5 = z(32);
Tto6 = z(33);
k1  = z(34);
k2  = z(35);
k3  = z(36);
k4  = z(37);
k5  = z(38);
k6  = z(39);
ea1  = z(40);
ea2  = z(41);
ea3  = z(42);
ea4  = z(43);
ea5  = z(44);
ea6  = z(45);
ee1  = z(46);
ee2  = z(47);
ee3  = z(48);
ee4  = z(49);
ee5  = z(50);
ee6  = z(51);
hy1  = z(52);
hy2  = z(53);
```

```
hy3  = z(54);
hy4  = z(55);
hy5  = z(56);
hy6  = z(57);
v1   = z(58);
v2   = z(59);
v3   = z(60);
v4   = z(61);
v5   = z(62);
v6   = z(63);
hcc0 = z(64);
hcc1 = z(65);
hcc2 = z(66);
hcc3 = z(67);
hcc4 = z(68);
hcc5 = z(69);
hcc6 = z(70);
hcoke0 = z(71);
hcoke1 = z(72);
hcoke2 = z(73);
hcoke3 = z(74);
hcoke4 = z(75);
hcoke5 = z(76);
hcoke6 = z(77);
Dic0 = z(78);
Dic1 = z(79);
Dic2 = z(80);
Dic3 = z(81);
Dic4 = z(82);
Dic5 = z(83);
Dic6 = z(84);
pos1 = z(85);
pos2 = z(86);
```

```
pos3 = z(87);
pos4 = z(88);
pos5 = z(89);
pos6 = z(90);
vH2O0 = z(91);
vH2O1 = z(92);
vH2O2 = z(93);
vH2O3 = z(94);
vH2O4 = z(95);
vH2O5 = z(96);
vH2O6 = z(97);
vC2H60 = z(98);
vC2H61 = z(99);
vC2H62 = z(100);
vC2H63 = z(101);
vC2H64 = z(102);
vC2H65 = z(103);
vC2H66 = z(104);
kH2O0 = z(105);
kH2O1 = z(106);
kH2O2 = z(107);
kH2O3 = z(108);
kH2O4 = z(109);
kH2O5 = z(110);
kH2O6 = z(111);
kC2H60 = z(112);
kC2H61 = z(113);
kC2H62 = z(114);
kC2H63 = z(115);
kC2H64 = z(116);
kC2H65 = z(117);
kC2H66 = z(118);
xH2O0 = z(119);
```

```
xH2O1 = z(120);
xH2O2 = z(121);
xH2O3 = z(122);
xH2O4 = z(123);
xH2O5 = z(124);
xH2O6 = z(125);
xHC0 = z(126);
xHC1 = z(127);
xHC2 = z(128);
xHC3 = z(129);
xHC4 = z(130);
xHC5 = z(131);
xHC6 = z(132);
visc0 = z(133);
visc1 = z(134);
visc2 = z(135);
visc3 = z(136);
visc4 = z(137);
visc5 = z(138);
visc6 = z(139);
phiHC_H2O0 = z(140);
phiHC_H2O1 = z(141);
phiHC_H2O2 = z(142);
phiHC_H2O3 = z(143);
phiHC_H2O4 = z(144);
phiHC_H2O5 = z(145);
phiHC_H2O6 = z(146);
phiH2O_HC0 = z(147);
phiH2O_HC1 = z(148);
phiH2O_HC2 = z(149);
phiH2O_HC3 = z(150);
phiH2O_HC4 = z(151);
phiH2O_HC5 = z(152);
```

```
phiH2O_HC6 = z(153);
cond0 = z(154);
cond1 = z(155);
cond2 = z(156);
cond3 = z(157);
cond4 = z(158);
cond5 = z(159);
cond6 = z(160);
CpH2O0 = z(161);
CpH2O1 = z(162);
CpH2O2 = z(163);
CpH2O3 = z(164);
CpH2O4 = z(165);
CpH2O5 = z(166);
CpH2O6 = z(167);
CpC2H60 = z(168);
CpC2H61 = z(169);
CpC2H62 = z(170);
CpC2H63 = z(171);
CpC2H64 = z(172);
CpC2H65 = z(173);
CpC2H66 = z(174);
Cp0 = z(175);
Cp1 = z(176);
Cp2 = z(177);
Cp3 = z(178);
Cp4 = z(179);
Cp5 = z(180);
Cp6 = z(181);
hconv0 = z(182);
hconv1 = z(183);
hconv2 = z(184);
hconv3 = z(185);
```

```
hconv4 = z(186);
hconv5 = z(187);
hconv6 = z(188);
Re0 = z(189);
Re1 = z(190);
Re2 = z(191);
Re3 = z(192);
Re4 = z(193);
Re5 = z(194);
Re6 = z(195);
Fr0 = z(196);
Fr1 = z(197);
Fr2 = z(198);
Fr3 = z(199);
Fr4 = z(200);
Fr5 = z(201);
Fr6 = z(202);
MW0 = z(203);
MW1 = z(204);
MW2 = z(205);
MW3 = z(206);
MW4 = z(207);
MW5 = z(208);
MW6 = z(209);
P1 = z(210);
P2 = z(211);
P3 = z(212);
P4 = z(213);
P5 = z(214);
P6 = z(215);
nHC0 = z(216);
nHC1 = z(217);
nHC2 = z(218);
```

```
nHC3 = z(219);
nHC4 = z(220);
nHC5 = z(221);
nHC6 = z(222);
V0 = z(223);
V1 = z(224);
V2 = z(225);
V3 = z(226);
V4 = z(227);
V5 = z(228);
V6 = z(229);

Tf0 = 1291;
B = 0.1;
sig = 5.67e-11;
et = 0.6;
At = 0.541;
er = 0.8;
Ar = 1.47;
mf = 9.6895;
Tg0 = 936;
Cpf = 1.46;
Ac = 16.35;
mg = 0.5259;
Cpg = 3.70;
pi = 3.14159;
Do = 0.088;
Hcrack = 140.29;
ea0 = 28.4;
Di = 0.0754;
x = 4.2;
A = 4.6e13;
Ea = 272838;
```

```
R = 8.3145;
ee0 = 0;
hy0 = 0;
pos0 = 0;
MW_H2O = 0.018;
MW_C2H6 = 0.030;
MW_C2H4 = 0.028;
MW_H2 = 0.002;
kcoke = 1.19e-2;
ktube = 3.03e-2;
P0 = 330000;
alpha = 1;
nH2O = 6.66;


fcns(1)= qn0 - qp0;
fcns(2)= qn3 - qp3;
fcns(3) = -B*sig*Tf1^4 - et*At*sig/4*(Tto1^4 + Tto5^4) + (B
+ er*Ar/4 + et*At/2)*qp1 - er*Ar/4*qn1 - (qp1 - qp0)/x;
fcns(4) = -B*sig*Tf2^4 - et*At*sig/4*(Tto2^4 + Tto4^4) + (B
+ er*Ar/4 + et*At/2)*qp2 - er*Ar/4*qn2 - (qp2 - qp1)/x;
fcns(5) = -B*sig*Tf3^4 - et*At*sig/2*Tto3^4 + (B + er*Ar/4
+ et*At/2)*qp3 - er*Ar/4*qn3 - (qp3 - qp2)/x;
fcns(6) = qp2 - qp4;
fcns(7) = qp1 - qp5;
fcns(8) = qp0 - qp6;
fcns(9) = B*sig*Tf1^4 + et*At*sig/4*(Tto1^4 + Tto5^4) - (B
+ er*Ar/4 + et*At/2)*qn1 + er*Ar/4*qp1 - (qn1 - qn0)/x;
fcns(10) = B*sig*Tf2^4 + et*At*sig/4*(Tto2^4 + Tto4^4) - (B
+ er*Ar/4 + et*At/2)*qn2 + er*Ar/4*qp2 - (qn2 - qn1)/x;
fcns(11) = B*sig*Tf3^4 + et*At*sig/2*Tto3^4 - (B + er*Ar/4
+ et*At/2)*qn3 + er*Ar/4*qp3 - (qn3 - qn2)/x;
fcns(12) = qn2 - qn4;
fcns(13) = qn1 - qn5;
fcns(14) = qn0 - qn6;
```

```
fcns(15) = 1/(mf*Cpf)*(B*Ac*(2*sig*Tf1^4 - qp1 - qn1)) -
(Tf1 - Tf0)/x;

fcns(16) = 1/(mf*Cpf)*(B*Ac*(2*sig*Tf2^4 - qp2 - qn2)) -
(Tf2 - Tf1)/x;

fcns(17) = 1/(mf*Cpf)*(B*Ac*(2*sig*Tf3^4 - qp3 - qn3)) -
(Tf3 - Tf2)/x;

fcns(18) = Tf2 - Tf4;

fcns(19) = Tf1 - Tf5;

fcns(20) = Tf0 - Tf6;

fcns(21) = 1/(mg*Cpg)*(hcc1*pi*Do*(Tto1 - Tg1) -
k1*ea1*Hcrack*pi*Di^2/4) - (Tg1 - Tg0)/x;

fcns(22) = 1/(mg*Cpg)*(hcc2*pi*Do*(Tto2 - Tg2) -
k2*ea2*Hcrack*pi*Di^2/4) - (Tg2 - Tg1)/x;

fcns(23) = 1/(mg*Cpg)*(hcc3*pi*Do*(Tto3 - Tg3) -
k3*ea3*Hcrack*pi*Di^2/4) - (Tg3 - Tg2)/x;

fcns(24) = 1/(mg*Cpg)*(hcc4*pi*Do*(Tto4 - Tg4) -
k4*ea4*Hcrack*pi*Di^2/4) - (Tg4 - Tg3)/x;

fcns(25) = 1/(mg*Cpg)*(hcc5*pi*Do*(Tto5 - Tg5) -
k5*ea5*Hcrack*pi*Di^2/4) - (Tg5 - Tg4)/x;

fcns(26) = 1/(mg*Cpg)*(hcc6*pi*Do*(Tto6 - Tg6) -
k6*ea6*Hcrack*pi*Di^2/4) - (Tg6 - Tg5)/x;

fcns(27) = et/2*(qp0 + qn0 - 2*sig*Tto0^4) - hcc0*(Tto0 -
Tg0);

fcns(28) = et/2*(qp1 + qn1 - 2*sig*Tto1^4) - hcc1*(Tto1 -
Tg1);

fcns(29) = et/2*(qp2 + qn2 - 2*sig*Tto2^4) - hcc2*(Tto2 -
Tg2);

fcns(30) = et/2*(qp3 + qn3 - 2*sig*Tto3^4) - hcc3*(Tto3 -
Tg3);

fcns(31) = et/2*(qp4 + qn4 - 2*sig*Tto4^4) - hcc4*(Tto4 -
Tg4);

fcns(32) = et/2*(qp5 + qn5 - 2*sig*Tto5^4) - hcc5*(Tto5 -
Tg5);

fcns(33) = et/2*(qp6 + qn6 - 2*sig*Tto6^4) - hcc6*(Tto6 -
Tg6);

fcns(34) =  A*exp(-Ea/(R*Tg1)) - k1;

fcns(35) =  A*exp(-Ea/(R*Tg2)) - k2;

fcns(36) =  A*exp(-Ea/(R*Tg3)) - k3;
```

```
fcns(37) =  A*exp(-Ea/(R*Tg4)) - k4;
fcns(38) =  A*exp(-Ea/(R*Tg5)) - k5;
fcns(39) =  A*exp(-Ea/(R*Tg6)) - k6;
fcns(40) =  -k1*ea1/v1 - (ea1 - ea0)/x;
fcns(41) =  -k2*ea2/v2- (ea2 - ea1)/x;
fcns(42) =  -k3*ea3/v3 - (ea3 - ea2)/x;
fcns(43) =  -k4*ea4/v4 - (ea4 - ea3)/x;
fcns(44) =  -k5*ea5/v5 - (ea5 - ea4)/x;
fcns(45) =  -k6*ea6/v6 - (ea6 - ea5)/x;
fcns(46) =  k1*ea1/v1 - (ee1 - ee0)/x;
fcns(47) =  k2*ea2/v2 - (ee2 - ee1)/x;
fcns(48) =  k3*ea3/v3 - (ee3 - ee2)/x;
fcns(49) =  k4*ea4/v4 - (ee4 - ee3)/x;
fcns(50) =  k5*ea5/v5 - (ee5 - ee4)/x;
fcns(51) =  k6*ea6/v6 - (ee6 - ee5)/x;
fcns(52) =  k1*ea1/v1 - (hy1 - hy0)/x;
fcns(53) =  k2*ea2/v2 - (hy2 - hy1)/x;
fcns(54) =  k3*ea3/v3 - (hy3 - hy2)/x;
fcns(55) =  k4*ea4/v4 - (hy4 - hy3)/x;
fcns(56) =  k5*ea5/v5 - (hy5 - hy4)/x;
fcns(57) =  k6*ea6/v6 - (hy6 - hy5)/x;
fcns(58) =  V1*4/(pi*Dic1^2) - v1;
fcns(59) =  V2*4/(pi*Dic2^2) - v2;
fcns(60) =  V3*4/(pi*Dic3^2) - v3;
fcns(61) =  V4*4/(pi*Dic4^2) - v4;
fcns(62) =  V5*4/(pi*Dic5^2) - v5;
fcns(63) =  V6*4/(pi*Dic6^2) - v6;
fcns(64) = (Do*(1/(hconv0*Dic0) + (kcoke*log(Do/Di) +
ktube*log(Di/Dic0))/(2*kcoke*ktube)))^(-1) - hcc0;
fcns(65) = (Do*(1/(hconv1*Dic1) + (kcoke*log(Do/Di) +
ktube*log(Di/Dic1))/(2*kcoke*ktube)))^(-1) - hcc1;
fcns(66) = (Do*(1/(hconv2*Dic2) + (kcoke*log(Do/Di) +
ktube*log(Di/Dic2))/(2*kcoke*ktube)))^(-1) - hcc2;
```

```
fcns(67) = (Do*(1/(hconv3*Dic3) + (kcoke*log(Do/Di) +
ktube*log(Di/Dic3))/(2*kcoke*ktube)))^(-1) - hcc3;

fcns(68) = (Do*(1/(hconv4*Dic4) + (kcoke*log(Do/Di) +
ktube*log(Di/Dic4))/(2*kcoke*ktube)))^(-1) - hcc4;

fcns(69) = (Do*(1/(hconv5*Dic5) + (kcoke*log(Do/Di) +
ktube*log(Di/Dic5))/(2*kcoke*ktube)))^(-1) - hcc5;

fcns(70) = (Do*(1/(hconv6*Dic6) + (kcoke*log(Do/Di) +
ktube*log(Di/Dic6))/(2*kcoke*ktube)))^(-1) - hcc6;

fcns(71) = 0*pos0 - hcoke0;

fcns(72) = 0*pos1 - hcoke1;

fcns(73) = 0*pos2 - hcoke2;

fcns(74) = 0*pos3 - hcoke3;

fcns(75) = 0*pos4 - hcoke4;

fcns(76) = 0*pos5 - hcoke5;

fcns(77) = 0*pos6 - hcoke6;

fcns(78) = Di - 2*hcoke0 - Dic0;

fcns(79) = Di - 2*hcoke1 - Dic1;

fcns(80) = Di - 2*hcoke2 - Dic2;

fcns(81) = Di - 2*hcoke3 - Dic3;

fcns(82) = Di - 2*hcoke4 - Dic4;

fcns(83) = Di - 2*hcoke5 - Dic5;

fcns(84) = Di - 2*hcoke6 - Dic6;

fcns(85) = pos0 + x - pos1;

fcns(86) = pos1 + x - pos2;

fcns(87) = pos2 + x - pos3;

fcns(88) = pos3 + x - pos4;

fcns(89) = pos4 + x - pos5;

fcns(90) = pos5 + x - pos6;

fcns(91) = 3.001e-12*Tg0^2 + 3.5967e-8*Tg0 + 12.7423e-7 -
vH2O0;

fcns(92) = 3.001e-12*Tg1^2 + 3.5967e-8*Tg1 + 12.742e-7 -
vH2O1;

fcns(93) = 3.001e-12*Tg2^2 + 3.5967e-8*Tg2 + 12.742e-7 -
vH2O2;
```

```
fcns(94) = 3.001e-12*Tg3^2 + 3.5967e-8*Tg3 + 12.742e-7 -
vH2O3;

fcns(95) = 3.001e-12*Tg4^2 + 3.5967e-8*Tg4 + 12.742e-7 -
vH2O4;

fcns(96) = 3.001e-12*Tg5^2 + 3.5967e-8*Tg5 + 12.742e-7 -
vH2O5;

fcns(97) = 3.001e-12*Tg6^2 + 3.5967e-8*Tg6 + 12.742e-7 -
vH2O6;

fcns(98) = -4.546e-12*Tg0^2 + 2.9244e-8*Tg0 + 12.231e-7 -
vC2H60;

fcns(99) = -4.546e-12*Tg1^2 + 2.9244e-8*Tg1 + 12.231e-7 -
vC2H61;

fcns(100) = -4.546e-12*Tg2^2 + 2.9244e-8*Tg2 + 12.231e-7 -
vC2H62;

fcns(101) = -4.546e-12*Tg3^2 + 2.9244e-8*Tg3 + 12.231e-7 -
vC2H63;

fcns(102) = -4.546e-12*Tg4^2 + 2.9244e-8*Tg4 + 12.231e-7 -
vC2H64;

fcns(103) = -4.546e-12*Tg5^2 + 2.9244e-8*Tg5 + 12.231e-7 -
vC2H65;

fcns(104) = -4.546e-12*Tg6^2 + 2.9244e-8*Tg6 + 12.231e-7 -
vC2H66;

fcns(105) = (3.0933e-8*Tg0^2 + 7.1725e-5*Tg0 - 0.6255e-
2)/1000 - kH2O0;

fcns(106) = (3.0933e-8*Tg1^2 + 7.1725e-5*Tg1 - 0.6255e-
2)/1000 - kH2O1;

fcns(107) = (3.0933e-8*Tg2^2 + 7.1725e-5*Tg2 - 0.6255e-
2)/1000 - kH2O2;

fcns(108) = (3.0933e-8*Tg3^2 + 7.1725e-5*Tg3 - 0.6255e-
2)/1000 - kH2O3;

fcns(109) = (3.0933e-8*Tg4^2 + 7.1725e-5*Tg4 - 0.6255e-
2)/1000 - kH2O4;

fcns(110) = (3.0933e-8*Tg5^2 + 7.1725e-5*Tg5 - 0.6255e-
2)/1000 - kH2O5;

fcns(111) = (3.0933e-8*Tg6^2 + 7.1725e-5*Tg6 - 0.6255e-
2)/1000 - kH2O6;

fcns(112) = (5.4595e-8*Tg0^2 + 12.471e-5*Tg0 - 2.226e-
2)/1000 - kC2H60;
```

```
fcns(113) = (5.4595e-8*Tg1^2 + 12.471e-5*Tg1 - 2.226e-
2)/1000 - kC2H61;

fcns(114) = (5.4595e-8*Tg2^2 + 12.471e-5*Tg2 - 2.226e-
2)/1000 - kC2H62;

fcns(115) = (5.4595e-8*Tg3^2 + 12.471e-5*Tg3 - 2.226e-
2)/1000 - kC2H63;

fcns(116) = (5.4595e-8*Tg4^2 + 12.471e-5*Tg4 - 2.226e-
2)/1000 - kC2H64;

fcns(117) = (5.4595e-8*Tg5^2 + 12.471e-5*Tg5 - 2.226e-
2)/1000 - kC2H65;

fcns(118) = (5.4595e-8*Tg6^2 + 12.471e-5*Tg6 - 2.226e-
2)/1000 - kC2H66;

fcns(119) = nH2O/(nH2O + nHC0) - xH2O0;

fcns(120) = nH2O/(nH2O + nHC1) - xH2O1;

fcns(121) = nH2O/(nH2O + nHC2) - xH2O2;

fcns(122) = nH2O/(nH2O + nHC3) - xH2O3;

fcns(123) = nH2O/(nH2O + nHC4) - xH2O4;

fcns(124) = nH2O/(nH2O + nHC5) - xH2O5;

fcns(125) = nH2O/(nH2O + nHC6) - xH2O6;

fcns(126) = 1 - xH2O0 - xHC0;

fcns(127) = 1 - xH2O1 - xHC1;

fcns(128) = 1 - xH2O2 - xHC2;

fcns(129) = 1 - xH2O3 - xHC3;

fcns(130) = 1 - xH2O4 - xHC4;

fcns(131) = 1 - xH2O5 - xHC5;

fcns(132) = 1 - xH2O6 - xHC6;

fcns(133) = (xH2O0*vH2O0*MW_H2O^0.5 +
xHC0*vC2H60*MW_C2H6^0.5)/(xH2O0*MW_H2O^0.5 +
xHC0*MW_C2H6^0.5) - visc0;

fcns(134) = (xH2O1*vH2O1*MW_H2O^0.5 +
xHC1*vC2H61*MW_C2H6^0.5)/(xH2O1*MW_H2O^0.5 +
xHC1*MW_C2H6^0.5) - visc1;

fcns(135) = (xH2O2*vH2O2*MW_H2O^0.5 +
xHC2*vC2H62*MW_C2H6^0.5)/(xH2O2*MW_H2O^0.5 +
xHC2*MW_C2H6^0.5) - visc2;
```

```
fcns(136) = (xH2O3*vH2O3*MW_H2O^0.5 +
xHC3*vC2H63*MW_C2H6^0.5)/(xH2O3*MW_H2O^0.5 +
xHC3*MW_C2H6^0.5) - visc3;

fcns(137) = (xH2O4*vH2O4*MW_H2O^0.5 +
xHC4*vC2H64*MW_C2H6^0.5)/(xH2O4*MW_H2O^0.5 +
xHC4*MW_C2H6^0.5) - visc4;

fcns(138) = (xH2O5*vH2O5*MW_H2O^0.5 +
xHC5*vC2H65*MW_C2H6^0.5)/(xH2O5*MW_H2O^0.5 +
xHC5*MW_C2H6^0.5) - visc5;

fcns(139) = (xH2O6*vH2O6*MW_H2O^0.5 +
xHC6*vC2H66*MW_C2H6^0.5)/(xH2O6*MW_H2O^0.5 +
xHC6*MW_C2H6^0.5) - visc6;

fcns(140) = (1+
(vC2H60/vH2O0)^0.5*(MW_H2O/MW_C2H6)^0.25)^2/(sqrt(8)*(1 +
(MW_C2H6/MW_H2O))^0.5) - phiHC_H2O0;

fcns(141) = (1+
(vC2H61/vH2O1)^0.5*(MW_H2O/MW_C2H6)^0.25)^2/(sqrt(8)*(1 +
(MW_C2H6/MW_H2O))^0.5) - phiHC_H2O1;

fcns(142) = (1+
(vC2H62/vH2O2)^0.5*(MW_H2O/MW_C2H6)^0.25)^2/(sqrt(8)*(1 +
(MW_C2H6/MW_H2O))^0.5) - phiHC_H2O2;

fcns(143) = (1+
(vC2H63/vH2O3)^0.5*(MW_H2O/MW_C2H6)^0.25)^2/(sqrt(8)*(1 +
(MW_C2H6/MW_H2O))^0.5) - phiHC_H2O3;

fcns(144) = (1+
(vC2H64/vH2O4)^0.5*(MW_H2O/MW_C2H6)^0.25)^2/(sqrt(8)*(1 +
(MW_C2H6/MW_H2O))^0.5) - phiHC_H2O4;

fcns(145) = (1+
(vC2H65/vH2O5)^0.5*(MW_H2O/MW_C2H6)^0.25)^2/(sqrt(8)*(1 +
(MW_C2H6/MW_H2O))^0.5) - phiHC_H2O5;

fcns(146) = (1+
(vC2H66/vH2O6)^0.5*(MW_H2O/MW_C2H6)^0.25)^2/(sqrt(8)*(1 +
(MW_C2H6/MW_H2O))^0.5) - phiHC_H2O6;

fcns(147) = (1+
(vH2O0/vC2H60)^0.5*(MW_C2H6/MW_H2O)^0.25)^2/(sqrt(8)*(1 +
(MW_H2O/MW_C2H6))^0.5) - phiH2O_HC0;

fcns(148) = (1+
(vH2O1/vC2H61)^0.5*(MW_C2H6/MW_H2O)^0.25)^2/(sqrt(8)*(1 +
(MW_H2O/MW_C2H6))^0.5) - phiH2O_HC1;
```

```
fcns(149) = (1+
(vH2O2/vC2H62)^0.5*(MW_C2H6/MW_H2O)^0.25)^2/(sqrt(8)*(1 +
(MW_H2O/MW_C2H6))^0.5) - phiH2O_HC2;

fcns(150) = (1+
(vH2O3/vC2H63)^0.5*(MW_C2H6/MW_H2O)^0.25)^2/(sqrt(8)*(1 +
(MW_H2O/MW_C2H6))^0.5) - phiH2O_HC3;

fcns(151) = (1+
(vH2O4/vC2H64)^0.5*(MW_C2H6/MW_H2O)^0.25)^2/(sqrt(8)*(1 +
(MW_H2O/MW_C2H6))^0.5) - phiH2O_HC4;

fcns(152) = (1+
(vH2O5/vC2H65)^0.5*(MW_C2H6/MW_H2O)^0.25)^2/(sqrt(8)*(1 +
(MW_H2O/MW_C2H6))^0.5) - phiH2O_HC5;

fcns(153) = (1+
(vH2O6/vC2H66)^0.5*(MW_C2H6/MW_H2O)^0.25)^2/(sqrt(8)*(1 +
(MW_H2O/MW_C2H6))^0.5) - phiH2O_HC6;

fcns(154) = xHC0*kC2H60/(xH2O0*phiHC_H2O0 + xHC0) +
xH2O0*kH2O0/(xHC0*phiH2O_HC0 + xH2O0) - cond0;

fcns(155) = xHC1*kC2H61/(xH2O1*phiHC_H2O1 + xHC1) +
xH2O1*kH2O1/(xHC1*phiH2O_HC1 + xH2O1) - cond1;

fcns(156) = xHC2*kC2H62/(xH2O2*phiHC_H2O2 + xHC2) +
xH2O2*kH2O2/(xHC2*phiH2O_HC2 + xH2O2) - cond2;

fcns(157) = xHC3*kC2H63/(xH2O3*phiHC_H2O3 + xHC3) +
xH2O3*kH2O3/(xHC3*phiH2O_HC3 + xH2O3) - cond3;

fcns(158) = xHC4*kC2H64/(xH2O4*phiHC_H2O4 + xHC4) +
xH2O4*kH2O4/(xHC4*phiH2O_HC4 + xH2O4) - cond4;

fcns(159) = xHC5*kC2H65/(xH2O5*phiHC_H2O5 + xHC5) +
xH2O5*kH2O5/(xHC5*phiH2O_HC5 + xH2O5) - cond5;

fcns(160) = xHC6*kC2H66/(xH2O6*phiHC_H2O6 + xHC6) +
xH2O6*kH2O6/(xHC6*phiH2O_HC6 + xH2O6) - cond6;

fcns(161) = 1.4537e-11*Tg0^3 - 1.8726e-7*Tg0^2 + 9.6453e-
4*Tg0 + 1.5267 - CpH2O0;

fcns(162) = 1.4537e-11*Tg1^3 - 1.8726e-7*Tg1^2 + 9.6453e-
4*Tg1 + 1.5267 - CpH2O1;

fcns(163) = 1.4537e-11*Tg2^3 - 1.8726e-7*Tg2^2 + 9.6453e-
4*Tg2 + 1.5267 - CpH2O2;

fcns(164) = 1.4537e-11*Tg3^3 - 1.8726e-7*Tg3^2 + 9.6453e-
4*Tg3 + 1.5267 - CpH2O3;

fcns(165) = 1.4537e-11*Tg4^3 - 1.8726e-7*Tg4^2 + 9.6453e-
4*Tg4 + 1.5267 - CpH2O4;
```

```
fcns(166) = 1.4537e-11*Tg5^3 - 1.8726e-7*Tg5^2 + 9.6453e-
4*Tg5 + 1.5267 - CpH2O5;

fcns(167) = 1.4537e-11*Tg6^3 - 1.8726e-7*Tg6^2 + 9.6453e-
4*Tg6 + 1.5267 - CpH2O6;

fcns(168) = 1.42e-10*Tg0^3 - 1.926e-6*Tg0^2 + 5.63e-3*Tg0 +
2.384e-1 - CpC2H60;

fcns(169) = 1.42e-10*Tg1^3 - 1.926e-6*Tg1^2 + 5.63e-3*Tg1 +
2.384e-1 - CpC2H61;

fcns(170) = 1.42e-10*Tg2^3 - 1.926e-6*Tg2^2 + 5.63e-3*Tg2 +
2.384e-1 - CpC2H62;

fcns(171) = 1.42e-10*Tg3^3 - 1.926e-6*Tg3^2 + 5.63e-3*Tg3 +
2.384e-1 - CpC2H63;

fcns(172) = 1.42e-10*Tg4^3 - 1.926e-6*Tg4^2 + 5.63e-3*Tg4 +
2.384e-1 - CpC2H64;

fcns(173) = 1.42e-10*Tg5^3 - 1.926e-6*Tg5^2 + 5.63e-3*Tg5 +
2.384e-1 - CpC2H65;

fcns(174) = 1.42e-10*Tg6^3 - 1.926e-6*Tg6^2 + 5.63e-3*Tg6 +
2.384e-1 - CpC2H66;

fcns(175) = (xH2O0*CpH2O0*MW_H2O +
xHC0*CpC2H60*MW_C2H6)/(xH2O0*MW_H2O + xHC0*MW_C2H6) - Cp0;

fcns(176) = (xH2O1*CpH2O1*MW_H2O +
xHC1*CpC2H61*MW_C2H6)/(xH2O1*MW_H2O + xHC1*MW_C2H6) - Cp1;

fcns(177) = (xH2O2*CpH2O2*MW_H2O +
xHC2*CpC2H62*MW_C2H6)/(xH2O2*MW_H2O + xHC2*MW_C2H6) - Cp2;

fcns(178) = (xH2O3*CpH2O3*MW_H2O +
xHC3*CpC2H63*MW_C2H6)/(xH2O3*MW_H2O + xHC3*MW_C2H6) - Cp3;

fcns(179) = (xH2O4*CpH2O4*MW_H2O +
xHC4*CpC2H64*MW_C2H6)/(xH2O4*MW_H2O + xHC4*MW_C2H6) - Cp4;

fcns(180) = (xH2O5*CpH2O5*MW_H2O +
xHC5*CpC2H65*MW_C2H6)/(xH2O5*MW_H2O + xHC5*MW_C2H6) - Cp5;

fcns(181) = (xH2O6*CpH2O6*MW_H2O +
xHC6*CpC2H66*MW_C2H6)/(xH2O6*MW_H2O + xHC6*MW_C2H6) - Cp6;

fcns(182) =
0.0279*mg^0.8*cond0^0.6*Cp0^0.4/(Dic0^1.8*visc0^0.4) -
hconv0;

fcns(183) =
0.0279*mg^0.8*cond1^0.6*Cp1^0.4/(Dic1^1.8*visc1^0.4) -
hconv1;
```

```
fcns(184) =
0.0279*mg^0.8*cond2^0.6*Cp2^0.4/(Dic2^1.8*visc2^0.4) -
hconv2;

fcns(185) =
0.0279*mg^0.8*cond3^0.6*Cp3^0.4/(Dic3^1.8*visc3^0.4) -
hconv3;

fcns(186) =
0.0279*mg^0.8*cond4^0.6*Cp4^0.4/(Dic4^1.8*visc4^0.4) -
hconv4;

fcns(187) =
0.0279*mg^0.8*cond5^0.6*Cp5^0.4/(Dic5^1.8*visc5^0.4) -
hconv5;

fcns(188) =
0.0279*mg^0.8*cond6^0.6*Cp6^0.4/(Dic6^1.8*visc6^0.4) -
hconv6;

fcns(189) = (4*mg)/(pi*Dic0*visc0) - Re0;

fcns(190) = (4*mg)/(pi*Dic1*visc1) - Re1;

fcns(191) = (4*mg)/(pi*Dic2*visc2) - Re2;

fcns(192) = (4*mg)/(pi*Dic3*visc3) - Re3;

fcns(193) = (4*mg)/(pi*Dic4*visc4) - Re4;

fcns(194) = (4*mg)/(pi*Dic5*visc5) - Re5;

fcns(195) = (4*mg)/(pi*Dic6*visc6) - Re6;

fcns(196) = 0.092*Re0^(-0.2)/Dic0 - Fr0;

fcns(197) = 0.092*Re1^(-0.2)/Dic1 - Fr1;

fcns(198) = 0.092*Re2^(-0.2)/Dic2 - Fr2;

fcns(199) = 0.092*Re3^(-0.2)/Dic3 - Fr3;

fcns(200) = 0.092*Re4^(-0.2)/Dic4 - Fr4;

fcns(201) = 0.092*Re5^(-0.2)/Dic5 - Fr5;

fcns(202) = 0.092*Re6^(-0.2)/Dic6 - Fr6;

fcns(203) = V0/(nH2O + nHC0)*(ea0*MW_C2H6 + ee0*MW_C2H4 +
hy0*MW_H2) + xH2O0*MW_H2O - MW0;

fcns(204) = V1/(nH2O + nHC1)*(ea1*MW_C2H6 + ee1*MW_C2H4 +
hy1*MW_H2) + xH2O1*MW_H2O - MW1;

fcns(205) = V2/(nH2O + nHC2)*(ea2*MW_C2H6 + ee2*MW_C2H4 +
hy2*MW_H2) + xH2O2*MW_H2O - MW2;

fcns(206) = V3/(nH2O + nHC3)*(ea3*MW_C2H6 + ee3*MW_C2H4 +
hy3*MW_H2) + xH2O3*MW_H2O - MW3;
```

```
fcns(207) = V4/(nH2O + nHC4)*(ea4*MW_C2H6 + ee4*MW_C2H4 +
hy4*MW_H2) + xH2O4*MW_H2O - MW4;

fcns(208) = V5/(nH2O + nHC5)*(ea5*MW_C2H6 + ee5*MW_C2H4 +
hy5*MW_H2) + xH2O5*MW_H2O - MW5;

fcns(209) = V6/(nH2O + nHC6)*(ea6*MW_C2H6 + ee6*MW_C2H4 +
hy6*MW_H2) + xH2O6*MW_H2O - MW6;

fcns(210) = (1/x*(1/MW1 - 1/MW0) + 1/MW1*(1/Tg1*((Tg1 -
Tg0)/x) + Fr1))/(1/(MW1*P1) -
P1/(alpha*R*Tg1)*(pi*Dic1/(4*mg))^2) - (P1 - P0)/x;

fcns(211) = (1/x*(1/MW2 - 1/MW1) + 1/MW2*(1/Tg2*((Tg2 -
Tg1)/x) + Fr2))/(1/(MW2*P2) -
P2/(alpha*R*Tg2)*(pi*Dic2/(4*mg))^2) - (P2 - P1)/x;

fcns(212) = (1/x*(1/MW3 - 1/MW2) + 1/MW3*(1/Tg3*((Tg3 -
Tg2)/x) + Fr3))/(1/(MW3*P3) -
P3/(alpha*R*Tg3)*(pi*Dic3/(4*mg))^2) - (P3 - P2)/x;

fcns(213) = (1/x*(1/MW4 - 1/MW3) + 1/MW4*(1/Tg4*((Tg4 -
Tg3)/x) + Fr4))/(1/(MW4*P4) -
P4/(alpha*R*Tg4)*(pi*Dic4/(4*mg))^2) - (P4 - P3)/x;

fcns(214) = (1/x*(1/MW5 - 1/MW4) + 1/MW5*(1/Tg5*((Tg5 -
Tg4)/x) + Fr5))/(1/(MW5*P5) -
P5/(alpha*R*Tg5)*(pi*Dic5/(4*mg))^2) - (P5 - P4)/x;

fcns(215) = (1/x*(1/MW6 - 1/MW5) + 1/MW6*(1/Tg6*((Tg6 -
Tg5)/x) + Fr6))/(1/(MW6*P6) -
P6/(alpha*R*Tg6)*(pi*Dic6/(4*mg))^2) - (P6 - P5)/x;

fcns(216) = (2*ea0 - ea0)*V0 - nHC0;

fcns(217) = (2*ea0 - ea1)*V1 - nHC1;

fcns(218) = (2*ea0 - ea2)*V2 - nHC2;

fcns(219) = (2*ea0 - ea3)*V3 - nHC3;

fcns(220) = (2*ea0 - ea4)*V4 - nHC4;

fcns(221) = (2*ea0 - ea5)*V5 - nHC5;

fcns(222) = (2*ea0 - ea6)*V6 - nHC6;

fcns(223) = (nH2O + nHC0)*R*Tg0/P0 - V0;

fcns(224) = (nH2O + nHC1)*R*Tg1/P1 - V1;

fcns(225) = (nH2O + nHC2)*R*Tg2/P2 - V2;

fcns(226) = (nH2O + nHC3)*R*Tg3/P3 - V3;

fcns(227) = (nH2O + nHC4)*R*Tg4/P4 - V4;

fcns(228) = (nH2O + nHC5)*R*Tg5/P5 - V5;
```

```
fcns(229) = (nH2O + nHC6)*R*Tg6/P6 - V6;

end
```

Appendix D Solving a system of algebraic equations in PREDICI®

As discussed in 4.6, the approach used to solve the system of algebraic equations to determine the radiant flux and furnace-gas temperature profiles is to use a second "imaginary" batch reactor in PREDICI® and then use the resulting solutions to solve the model for the primary "real" reactor. To use this approach, it is important for both reactors to be batch reactors because of the complex way that PREDICI® handles tubular reactors.

PREDICI® solves ODEs with respect to time and handles tubular reactors by exploiting the analogy between time in a batch reactor and position in a tubular reactor. Essentially, when tubular reactor mode is used in PREDICI®, any user-input value in the "tubular reactor" mode is converted automatically by PREDICI® into its batch analog. Therefore, when the length of the reactor is input by the user, PREDICI® converts this to a residence time by multiplying by the inverse of velocity in the tubular reactor

$$\frac{1}{v_g} = \frac{\rho_g \frac{\pi}{4} {D_i}^2}{\dot{m}_g} \qquad 77$$

PREDICI® is then set up to perform the internal calculation with respect to time, as it would for a normal batch reactor. If a second tubular reactor were used as the "imaginary" reactor to solve the system of algebraic equations, PREDICI® would also scale the length of this imaginary reactor by the inverse of velocity, altering the form of the system of equations being solved. To avoid any confusion associated with this approach, I have used batch reactor mode to model both the imaginary reactor and the real tubular reactor.

For the primary "real" reactor, I have applied the same scaling that PREDICI® does implicitly when it uses tubular reactor mode, but I have done so explicitly using the "rel. velocity" feature. By inserting the factor of $1/v_g$ in a function file in the "rel. velocity" field (shown in Figure 36), the PREDICI®-generated ODEs are scaled by this factor, so that they end up being solved with respect to position rather than time.

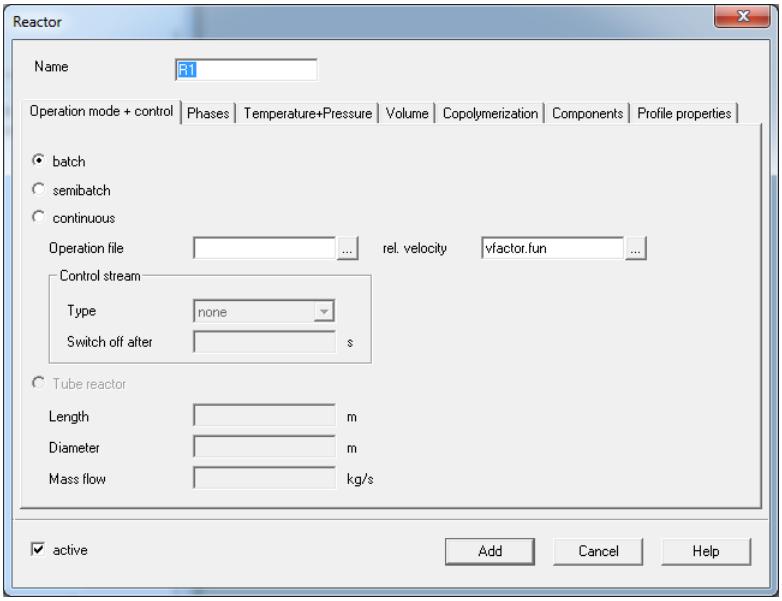

Figure 36 – Reactor settings dialog box in PREDICI®

The rate of change in methane concentration, discussed in 4.5, can once again be used as an example of what happens to PREDICI®-generated ODEs when the "rel. velocity" feature is used in a batch reactor. As presented in equation 46, PREDICI® generates the ODE:

$$\frac{d[CH_4]}{dt} = k_7[C_2H_4][CH_3] + k_8[C_2H_6][CH_3] \qquad \textbf{46}$$

when the kinetic module is used to input reaction kinetics involving methane. Using the "rel. velocity" feature, equation 46 (generated automatically by PREDICI®) is multiplied on both sides by $1/v_g = dt/dx$ to give

$$\frac{d[CH_4]}{dx} = \frac{1}{v_g}(k_7[C_2H_4][CH_3] + k_8[C_2H_6][CH_3]) \quad \textbf{78}$$

The result is the calculation of the rate of change in methane concentration as the process gas flows along the tube (in $mol \cdot m^{-3}m^{-1}$). Using this approach, all of the user-input ODEs must be input with respect to changes in position (as were they originally derived in Chapter 3). The scaling presented in Table 10 in section 4.5 is not used. Note that PREDICI® outputs show concentrations and temperatures plotted with respect to "time" but because of the rel. velocity scaling, these "times" are actually positions. All of the automatically generated plots from PREDICI® need to be replotted so that users of the model will not be confused.

To solve the system of algebraic equations, all of the unknowns in the system must be entered as "elemental species" in the imaginary second reactor in PREDICI®. The reactor in which each "elemental species" resides is specified in the elemental-species dialog box shown in Figure 37.

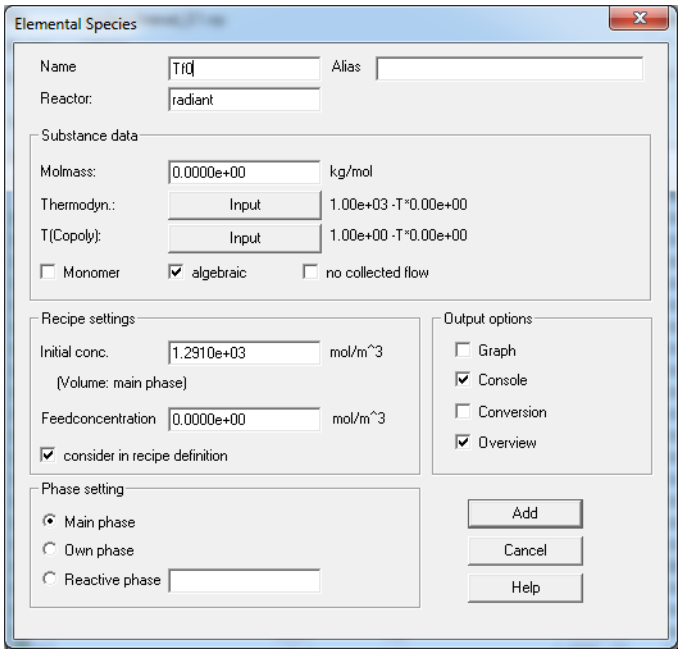

Figure 37 – Elemental Species dialog box in PREDICI®

It is important that all unknowns associated with the set of algebraic equations are input into the second reactor, which I have named *radiant*. These fake species have a molecular weight of zero. It is also required that the "algebraic" option in the elemental species dialog box shown in Figure 37 is checked.

By choosing the "algebraic" option, these "elemental species" are handled differently when they are called into a user-generated ODE module. Instead of the right-hand side of the equation expressing a rate of change, as in an ODE, the right-hand side of the equation provides a function, which will equal zero after the equations are solved. As an example, when the "algebraic" option is selected for the variable $q^+{}_0$, PREDICI® no longer solves:

$$\frac{dq^+{}_0}{dx} = f(q^+{}_0) \qquad \textbf{79}$$

in the user-input ODE module, but instead it solves

$$0 = f(q^+{}_0) \qquad \textbf{80}$$

All of the unknowns (e.g., 2745 of them) associated with the set of algebraic equations to be solved are set as "algebraic elemental species". Then the user-input "ODE module" is used to solve this system of algebraic equations. This can be accomplished in a single function file which includes all 2745 equations and 2745 unknowns (for the 80-section discretization). The unknowns are called arg1 through arg2745. An illustration of the function file format is shown in Figure 38, where qp0, qp1 and qp2 are the names that I gave to the first three elemental species (corresponding to fluxes in the upward direction at discrete positions 0, 1 and 2 and V80 is the name that I gave to the final elemental species corresponding to the process gas volume at the discrete position 80).

```
Arguments 2745

qp0     value
qp1     value
qp2     value
 .        .
 .        .
 .        .
V80     value

qp0 = arg1
qp1 = arg2
qp2 = arg3
    .
    .
    .
V80 = arg2745

result1 = f1(qp0, qp1, qp2, ..., V80)
result2 = f2(qp0, qp1, qp2, ..., V80)
result3 = f3(qp0, qp1, qp2, ..., V80)
                  .
                  .
                  .
result2745 = f2745(qp0, qp1, qp2, ..., V80)
```

Figure 38 – Illustration of PREDICI® code format to solve system of 2745 algebraic functions f1, f2, f3 …f2745 with 2745 unknowns

As with most numerical solvers for nonlinear systems of algebraic equations, PREDICI® requires an initial guess for the value of each variable. The initial guess is input in the elemental species dialog box in the "initial conc." field shown in Figure 37. The better the initial guess, the fewer the iterations that are required to solve the system of equations. For poor initial guesses, the solution may not converge.

Each iteration used to solve the system of equations is equivalent to a "time" step for solving ODEs in PREDICI®. While these "time" steps are taken to solve the system of algebraic equations in the imaginary reactor, the same time steps are taken in the real reactor. Unfortunately, the "real" reactor requires the solutions from the system of algebraic equations to account for the heat transferred to the reactor contents. These values are unknown until the system of algebraic equations has been solved after a few time steps. Therefore, the size of the "time" step must be short so that the amount of "time" (really distance) required to solve the system of equations in the imaginary reactor is small relative to the total length of the real reactor.

For example, if 10 iterations are required to solve the system of algebraic equations and the maximum step size (used for both the imaginary and the real reactor) is set at 0.01 m, the maximum tube length used to solve the system of equations is 0.1 m, which is small relative to the total tube length of 25.2 m (in the cold box). The step-size limit can be set in the Numerical Options dialog box in the "Max. Stepsize" field, as shown in Figure 39.

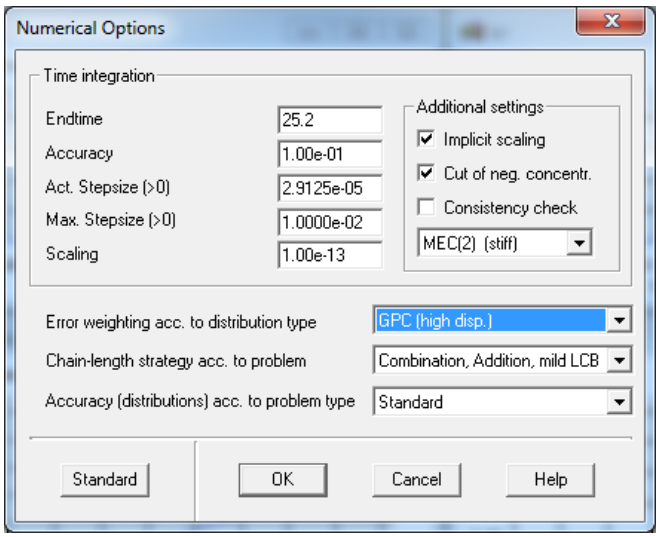

Figure 39 – Numerical Options dialog box in PREDICI®

Note that the automatic step size chosen by PREDICI® may be smaller than the maximum step-size. For example, Figure 40a) shows a case where five steps are taken in the first 0.00007 m in PREDICI®. Figure 40b) shows that the variable, qp0 has reached a nearly constant value by a position of 0.005 m.

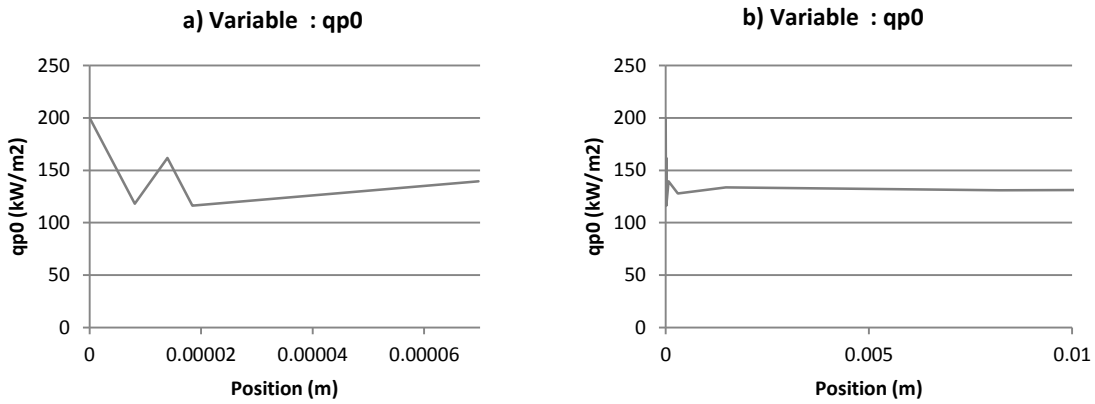

Figure 40 – a) the first 5 steps taken to solve for variable qp0 in the imaginary reactor in PREDICI® b) the solution for the variable qp0 reached by 0.005 m in PREDICI®

The qp0 profile shown in Figure 40b) indicates that PREDICI® solved the system of algebraic equations by a position ~of 0.005 m, which means that these results are now available to be called into the real reactor to provide the radiant flux profiles in the cold box.

Limiting the step size and adding a large number of equations and "elemental species" slows down simulation time significantly (from ~30 s when flux profiles were calculated in MATLAB® to >1 hour when flux profiles were calculated in PREDICI®). Therefore, steps were taken to reduce simulation times.

Since the system of equations residing in the imaginary reactor is solved in the first <0.1 m of the tube, and thereafter the results are stored in PREDICI®, it is not necessary to continue to solve these equations along the remaining length of the reactor. The imaginary reactor can be turned off so that PREDICI® no longer solves any equations associated with that reactor using the *setreactorstate* function in the *schedule* in PREDICI®. The *schedule* field is located under the Settings tab in the PREDICI® workshop, and the code used to set turn off the *radiant* reactor at a position of 0.1 m is

shown in Figure 41. I appreciate all of the help from Dr. Michael Wulkow who showed me how to use this function in PREDICI®, which is not described in the manual.

```
x = acttime()

if (x < 0.1)
{dummy = setreactorstate("radiant",1)
result1 = 0.1
}
        else if ((x >= 0.1) && (x < 25.2))
        {dummy = setreactorstate("radiant", 0)
        result1 = 25.2
        }
```

Figure 41 – PREDICI® code used in a schedule function file to turn off reactor *radiant* after 0.1 m

Note that "result1" indicated in a schedule function file creates a "stoptime" in PREDICI®.

Once the system of equations in the imaginary reactor has been solved, it becomes unnecessary to limit the step size to 0.01 m. The schedule can also be used to control the maximum step size using the *setmaxtimestep* function as shown in Figure 42.

```
x = acttime()

if (x < 0.1)
{dummy = setreactorstate("radiant", 1)
dummy1 = setmaxtimestep(0.01)
result1 = 0.1
}
        else if ((x >= 0.1) && (x < 25.2))
        {dummy = setreactorstate("radiant", 0)
        dummy1 = setmaxtimestep(0.5)
        result1 = 25.2
        }
```

Figure 42 – PREDICI® code used in a schedule function file to adjust the maximum step size

The accuracy of the simulation can also be adjusted to reduce simulation times, with a *higher* value of "accuracy" setting decreasing the simulation time. The accuracy field is located under the Settings tab in the PREDICI® workshop and takes a numerical value as an input. Figure 43 shows the result of changing the accuracy setting on the process gas temperature profile.

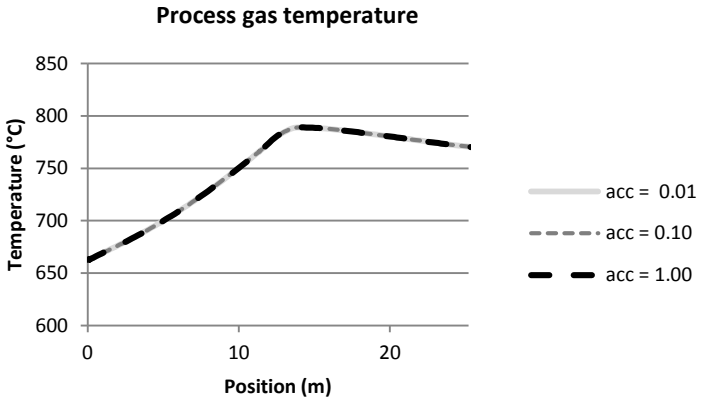

Figure 43 – Effect of changing accuracy on process gas temperature predictions in PREDICI®

As can be seen in Figure 43, there is no significant effect on the process gas temperature profile of increasing the accuracy setting (and therefore making the solution faster and less accurate) from 0.01 to 1 and therefore a value of 1 was chosen for future simulations. Changing the accuracy to 1 in conjunction with increasing the maximum step size to 0.5 m and turning off the imaginary reactor after the first 0.1 m decreased the simulation times from >1 hour to ~6 minutes. Further adjustments to reduce the simulation time should be investigated because they may be important when parameters are estimated in future stages of model development.

When the model was extended to include the cross-over tube and the hot box, the imaginary reactor was turned back on using the schedule file just before the inlet of the hot box. Attempts were made to solve the system of algebraic equations again, using updated initial values calculated from the integration of the model equations in the cold box and cross-over tube. Unfortunately, this attempt failed due to a "divide by zero" error on line 4475 which is depicted in Figure 44.

```
4473 result269 =     -k26*ea26/v26 - (ea26 - ea25)/x
4474 result270 =     -k27*ea27/v27 - (ea27 - ea26)/x
4475 result271 =     -k28*ea28/v28 - (ea28 - ea27)/x
4476 result272 =     -k29*ea29/v29 - (ea29 - ea28)/x
4477 result273 =     -k30*ea30/v30 - (ea30 - ea29)/x
```

Figure 44 – Line of code from PREDICI® that resulted in a "divide by zero" error

Examining the plot of the variable v28 (the process gas velocity at discrete position 28) in Figure 45 shows that once the imaginary reactor is turned back on at a position of 31.3 m (0.1 m before the inlet of the hot box), the simulation takes two steps and the second step brings v28 to a value of zero.

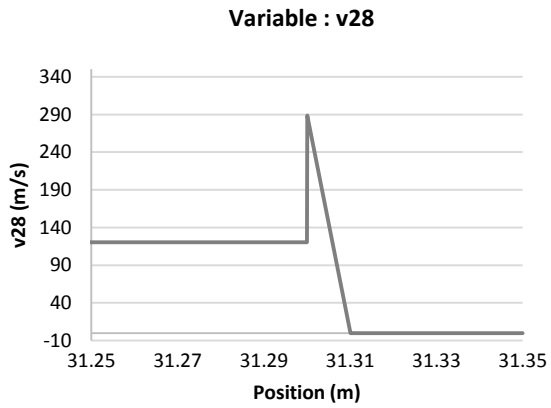

Figure 45 – Attempted solution for the process gas velocity at discrete position 28 in the hot box resulting in divide by zero error in PREDICI®

Since the unknown variables are implemented as "elemental species", PREDICI® sets a lower limit of zero. When the searching for the solution of v28 this limit of zero is hit, which leads to v28 = 0 m/s. If a better initial guess were used for v28, then it is possible that while searching for a solution, the oscillation in values between each iteration would be smaller and the lower limit would not be hit.

The model user is unable to specify better initial guesses for the values of the unknowns in the hot box. PREDICI® stores the cold-box solution of the system of algebraic equations, and these values automatically become the initial guesses for future solutions of the same system of algebraic equations. There is too large of a change between operating conditions for the cold box and operating conditions for the hot box for the cold-box solutions to provide good enough initial guesses for the hot-box solution. As a

result, I decided to change the inputs to the set of algebraic equations in a gradual ramp. The input variables that were updated between solving the system of equations in the hot box and the cold box are:

- internal tube diameter
- inlet concentration of ethane
- inlet concentration of ethylene
- inlet concentration of hydrogen
- inlet process gas temperature
- inlet process gas pressure

This ramping and iterative solution process to obtain good initial guesses could be performed by turning the imaginary reactor on in either the cold box or at the start of the hot box. I decided to do the ramping and iterations within the cold box so that any numerical problems associated with the ramping would be encountered before having to integrate the real PREDICI® model to the end of the cross-over tube.

Unfortunately, using this approach, the value of these inputs (except the internal tube diameter) are not known exactly, because they are determined from the integration of the model equations through the cold box and cross-over tube. However, reasonable guesses for these input values can be made (based on prior simulations) so that algebraic equations can be solved within the cold box to obtain good initial values for solving the algebraic equations at the hot box inlet. Once the cold-box and cross-over tube model equations have been integrated and the actual values of these model inputs are known, the model only has to move from the guessed model inputs to the actual model inputs (a

much smaller change than from the cold-box conditions to the hot-box conditions, assuming that the algebraic-model input guesses were reasonable). If the model-input guesses are not accurate enough, and a divide by zero error still arises at the inlet of the hot box, the simulation can be restarted with updated values of model-input guesses (which are now known from the solution of the cold box).

Appendix E Additional simulation study results

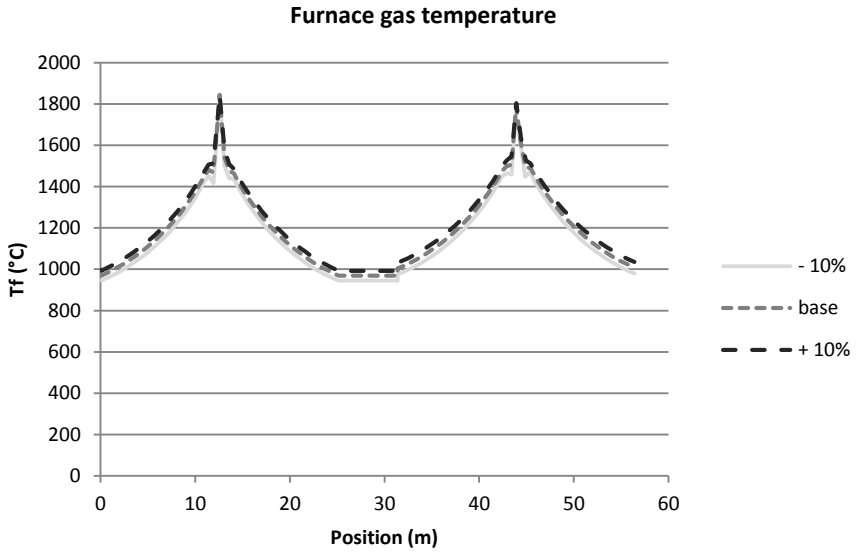

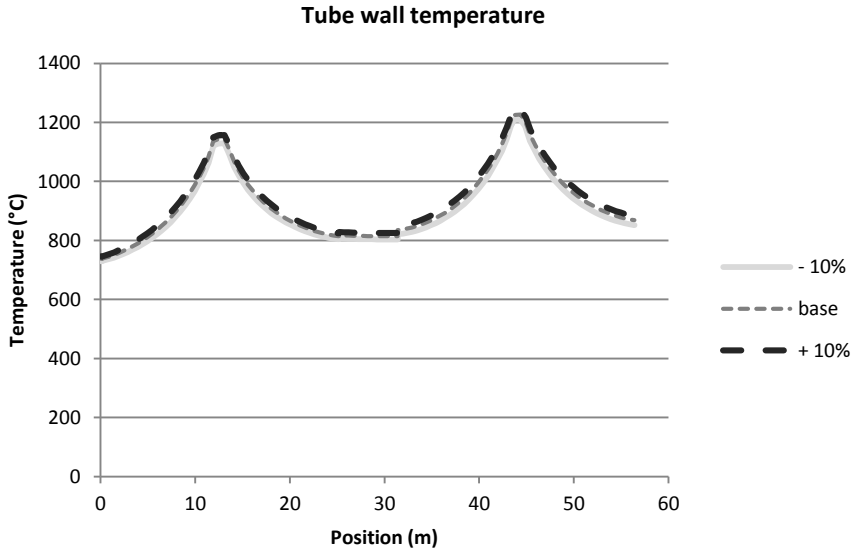

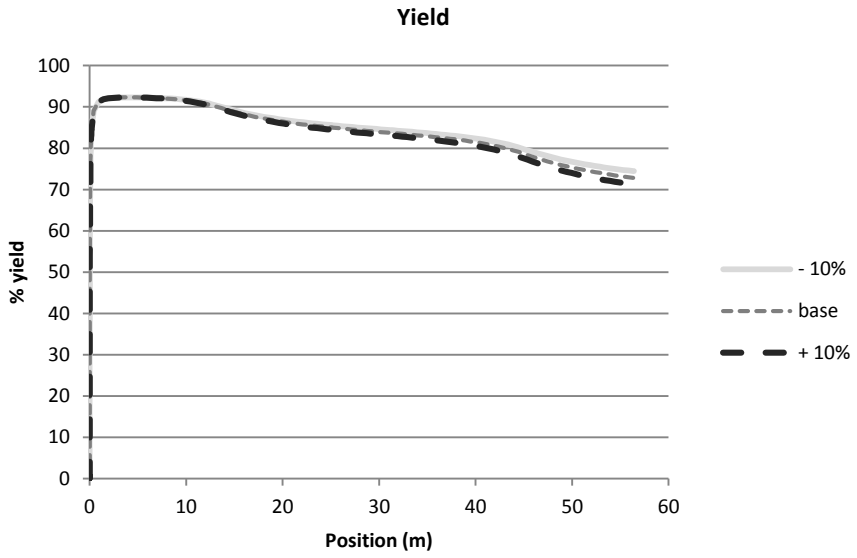

Figure 46 – Model predictions of furnace gas temperature, tube wall temperature and ethylene yield in response to changes in mass flow rate of fuel

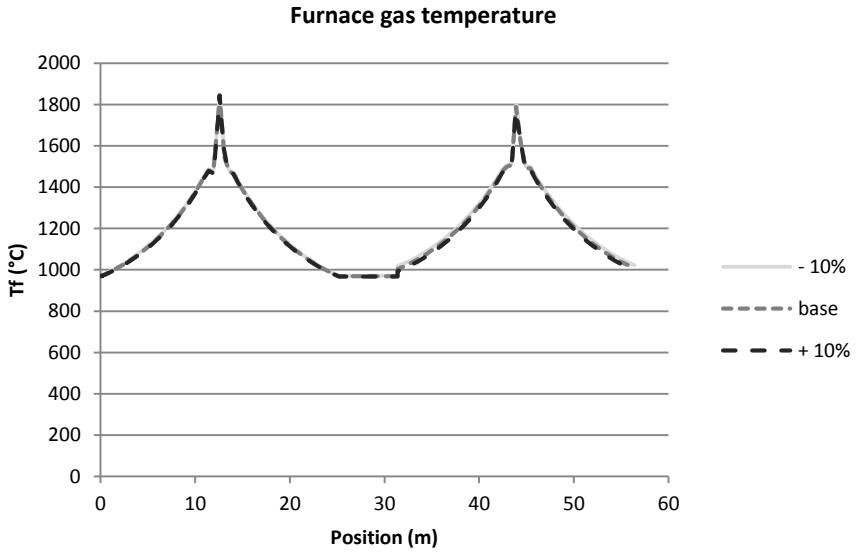

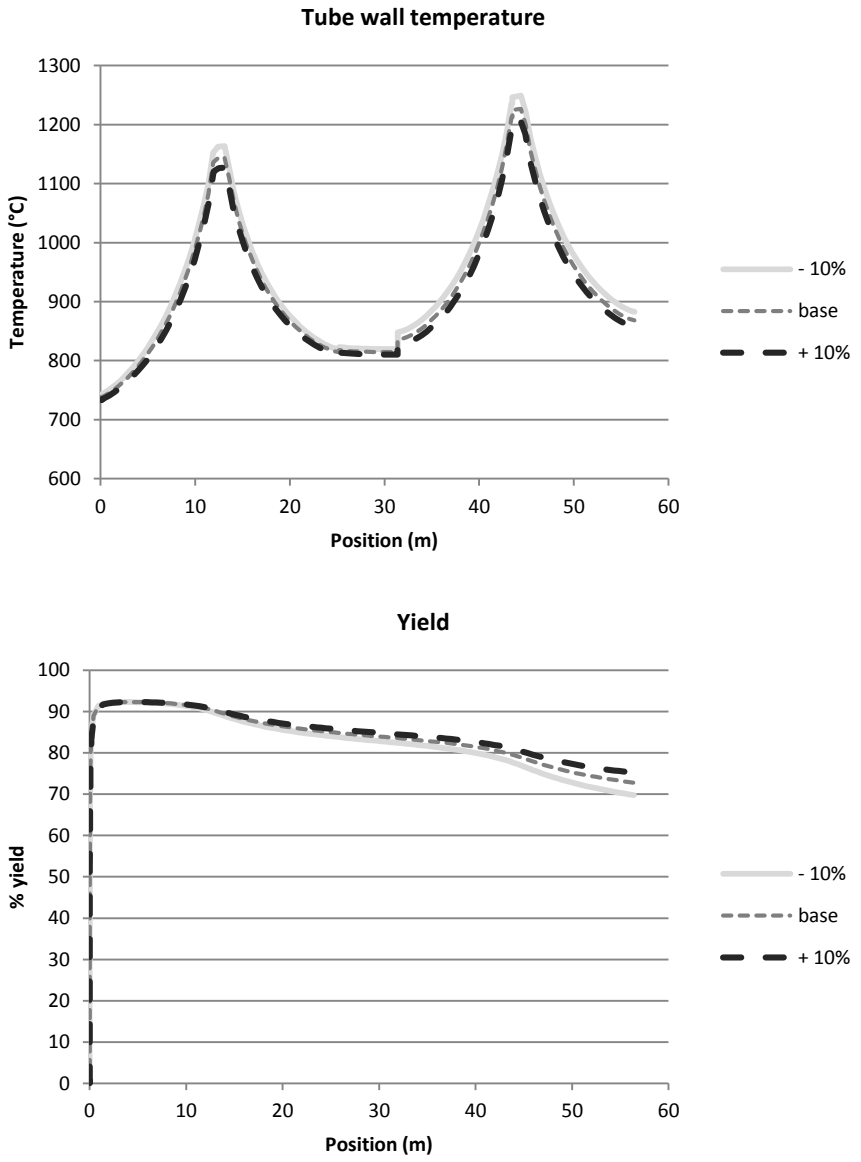

Figure 47 – Model predictions of furnace gas temperature, tube wall temperature and ethylene yield in response to changes in mass flow rate of process gas

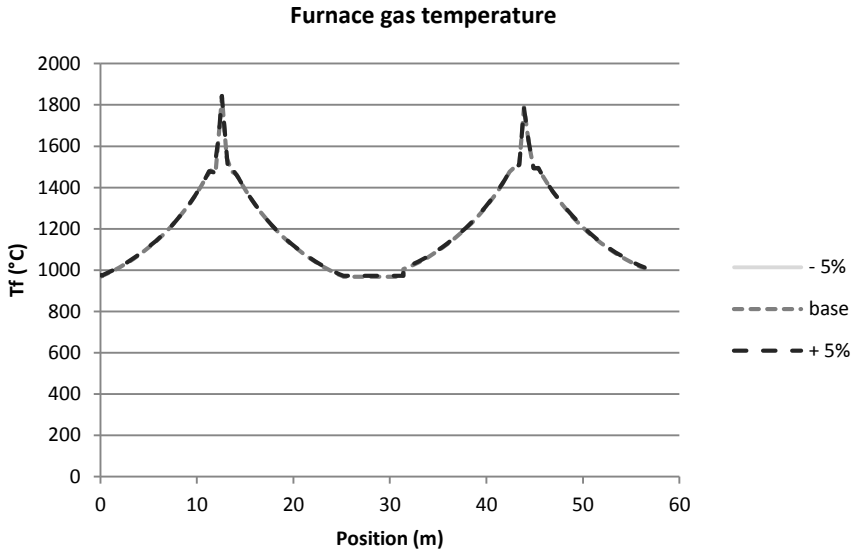
Furnace gas temperature
Tf (°C)
2000
1800
1600
1400
1200
1000
800
600
400
200
0
0
10
20
30
40
50
60
Position (m)
- 5%
base
+ 5%

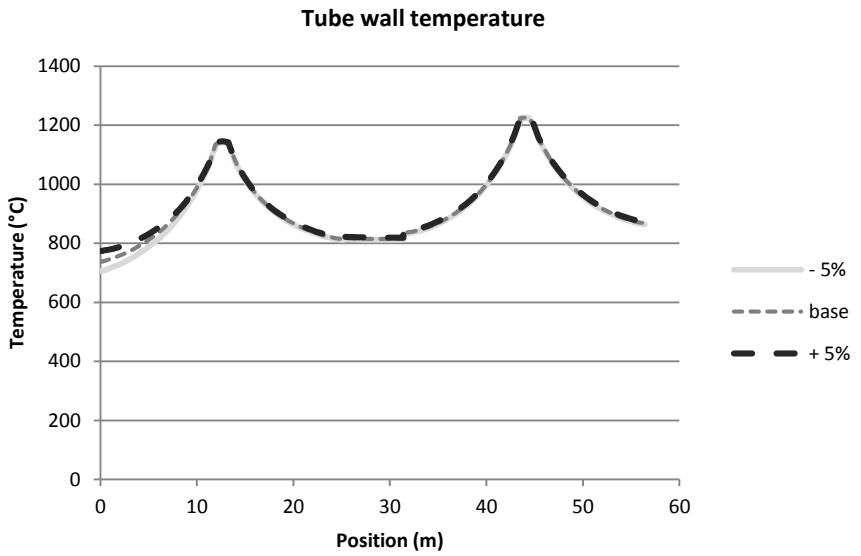
Tube wall temperature
Temperature (°C)
1400
1200
1000
800
600
400
200
0
0
10
20
30
40
50
60
Position (m)
- 5%
base
+ 5%

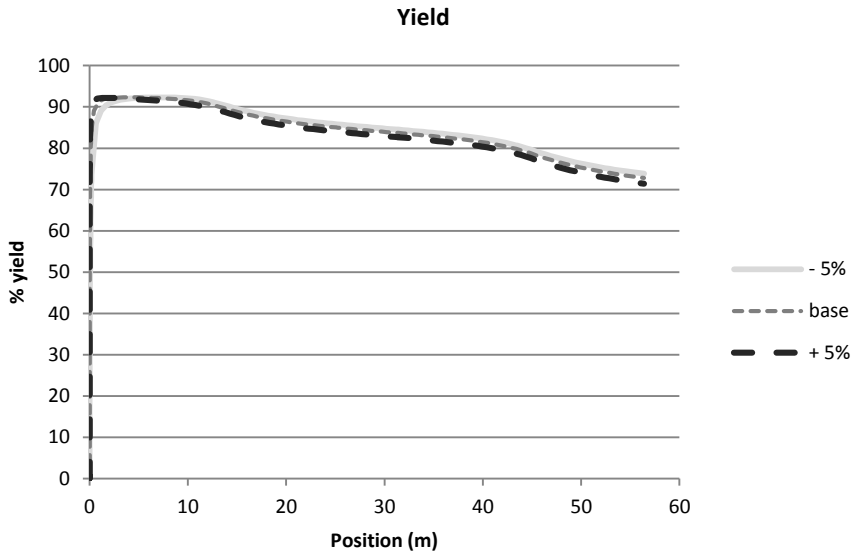

Figure 48 – Model predictions of furnace gas temperature, tube wall temperature and ethylene yield in response to changes in inlet temperature of process gas

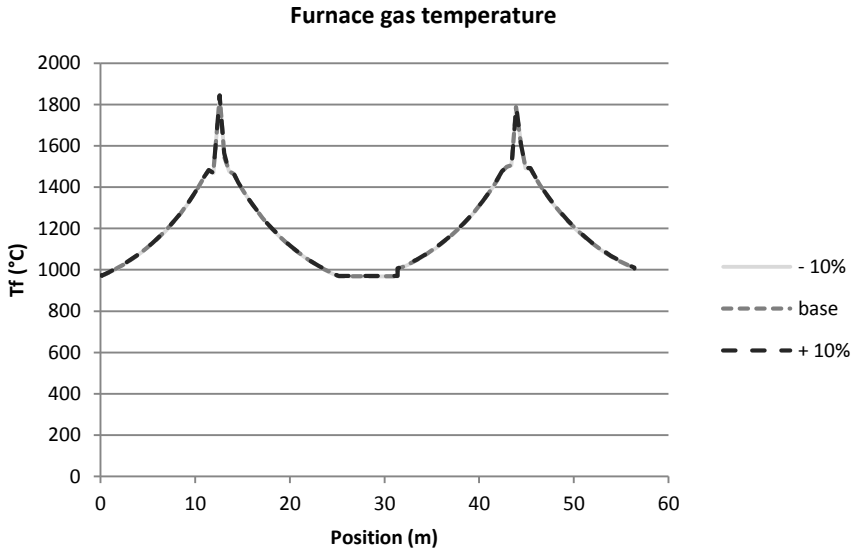

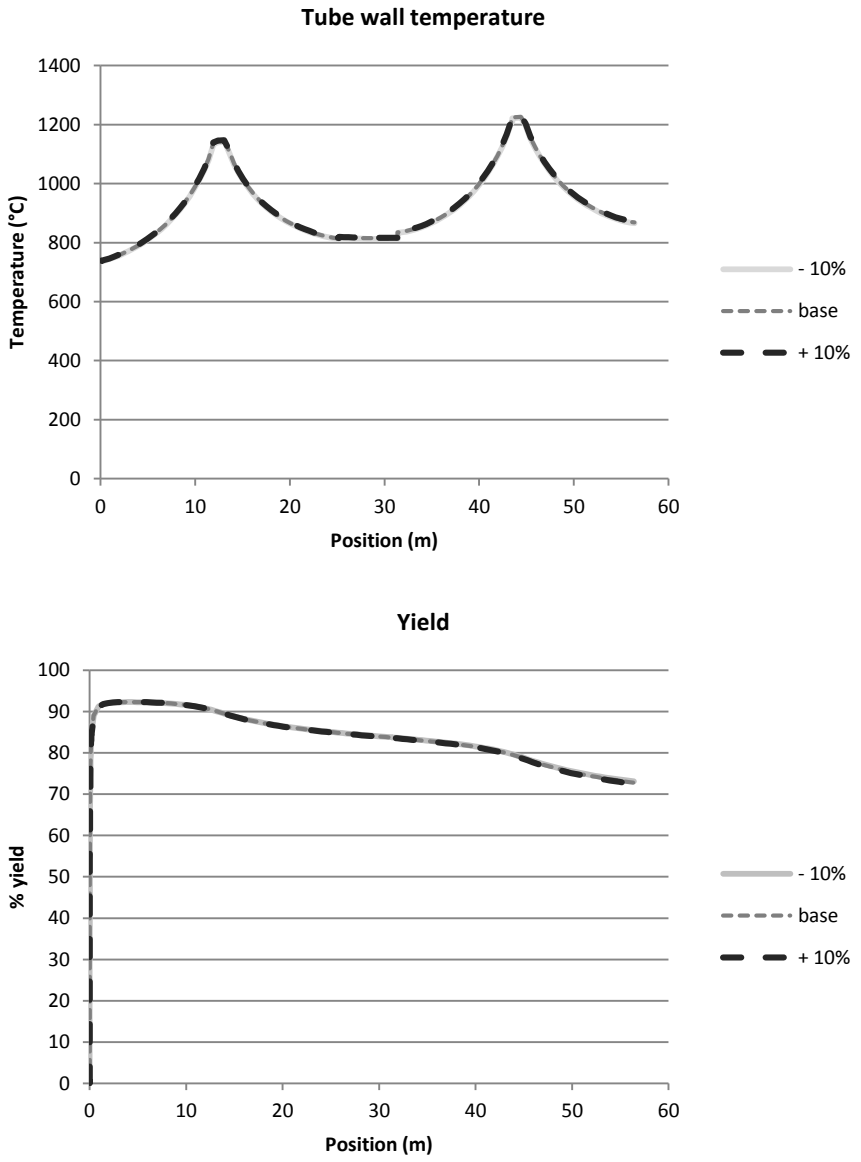

Figure 49 – Model predictions of furnace gas temperature, tube wall temperature and ethylene yield in response to changes in steam to ethane mass flow rate ratio

Appendix F Side-fired furnace implementation

The side-fired furnace (as depicted in Figure 3b) has terraces on the side walls of both the hot box and the cold box to provide heat more uniformly to reactor contents. Initial modeling attempts assumed that there was a terrace at every vertical position *z* and as a result, the combustion gas entered the radiant section at a constant rate over the height of the furnace. Only a cold-box model was attempted, and it was assumed that half of the total mass flow rate of furnace gas enters in the cold box and the other half enters in the hot box. Therefore, the rate of addition of combustion gas can be calculated as:

$$r_{cg} = \frac{\dot{m}_{f,tot}}{2H_{furnace}} \quad \textbf{81}$$

where $\dot{m}_{f,tot}$ is the total mass flow of furnace gas to the radiant section, the factor of two accounts for half of the total mass going to the cold box, and $H_{furnace}$ is the height of the furnace.

A total energy balance was performed on the furnace gas over a small section of height Δz:

$$\begin{aligned} \text{Accumulation} = {} & \text{enthalpy in with furnace gas flow at bottom} - \text{enthalpy out with furnace gas flow at top} + \text{enthalpy in with combustion gas flow} \\ & + \text{upward radiation absorbed by furnace gas} + \text{downward radiation absorbed by furnace gas} - \text{radiation emitted by furnace gas} \end{aligned} \quad \textbf{82}$$

The flux terms were converted to energy flows by multiplying by the cross sectional area, A_c so that equation 82 is:

$$0 = \dot{m}_{f,z}C_{p,f}(T_{f,z} - T_{ref}) - \dot{m}_{f,z+\Delta z}C_{p,f}(T_{f,z+\Delta z} - T_{ref}) + \dot{m}_{cg}C_{p,cg}(T_{comb} - T_{ref}) \quad \textbf{83}$$

$$+ \quad \beta A_{c,rad} q^{+} \Delta z \quad + \quad \beta A_{c,rad} q^{-} \Delta z \quad - \quad 2\beta A_{c,rad} \sigma T_f{}^4 \Delta z$$

where $\dot{m}_{cg}$ is the local mass flow rate of combustion gas (fuel plus associated air), and T_{comb} is the temperature of combustion gas entering the volume. If it is assumed that the combustion gas enters uniformly along the height of the radiant section then mass flow rate of combustion gas $\dot{m}_{cg}$ can be replaced by $r_{cg}\Delta z$ (the rate of mass flow of combustion gas per unit height multiplied by the height section). The steady-state mass balance on the volume element is then:

0	=	furnace gas in at bottom	+	furnace gas added from combustion	-	Furnace gas out at top	**84**
0	=	$\dot{m}_{f,z}$	+	$r_{cg}\Delta z$	-	$\dot{m}_{f,z+\Delta z}$	

which becomes the ODE:

$$\frac{d\dot{m}_f}{dz} = r_{cg} \qquad \textbf{85}$$

when Δz approaches zero.

The composition of the furnace gas entering at the bottom of the volume element will have the same composition as the combustion gas which means that the heat capacities can all be expressed by the same average heat capacity calculation and will only vary as a function of temperature. With this consideration equation 36 becomes the ODE:

$$\frac{dT_f}{dz} = \frac{1}{\dot{m}_f C_{p,f}} \left(r_{cg} C_{p,f} \left(T_{comb} - T_f \right) + \beta A_{c,rad} \left(q^{+} + q^{-} - 2\sigma T_f{}^4 \right) \right) \qquad \textbf{86}$$

when Δz approaches zero.

Unfortunately, when equation 86 was implemented in PREDICI® and shooting was used to solve the boundary value problem (see section 4.6.1), appropriate initial conditions could not be found to fulfil the boundary conditions. Attempts were also made to solve the side-fired model equations using the discretization of a simplified model in MATLAB® (see section 4.6.2). However, this approach was also unsuccessful with either no solution found, or a physically unrealistic solution such as the furnace gas temperature profile shown in Figure 50 which resulted from a discretization with $\Delta x = 0.63$ m.

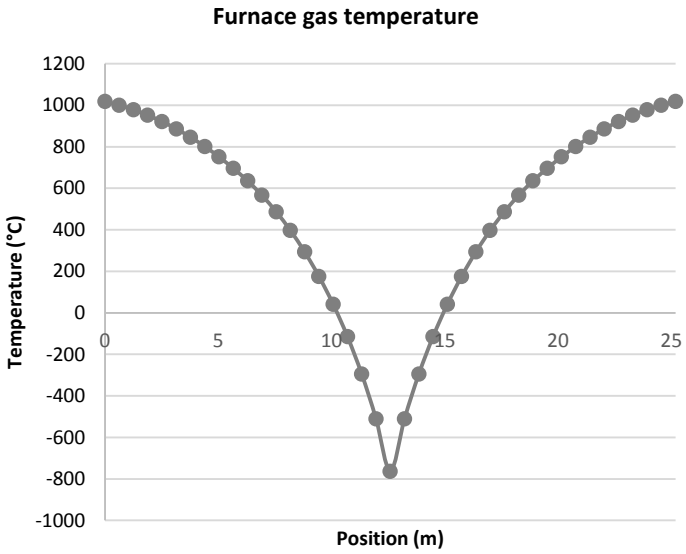

Figure 50 – Furnace gas temperature profile resulting from side-fired modeling attempts using a simplified discretized model in MATLAB® ($\Delta x = 0.63$ m)

Based on these unsuccessful attempts to model side-fired operation, recommendations for future work would be to modify the assumption that furnace gas is added continuously over the entire height of the furnace. Instead, discrete additions of furnace gas at different heights along the furnace should be investigated.